Fracture of porous ceramics : application to the mechanical degradation of solid oxide cells during redox cycling

Amira Abaza

THÈSE

Pour obtenir le grade de

DOCTEUR DE L'UNIVERSITE GRENOBLE ALPES

Spécialité : **Matériaux, Mécanique, Génie civil, Electrochimie**

Arrêté ministériel : 25 mai 2016

Présentée par

Amira ABAZA

Thèse dirigée par **Jérôme LAURENCIN,** Ingénieur de recherche, Univ. Grenoble Alpes – CEA/LITEN,
codirigée par **Sylvain MEILLE,** Professeur, MATEIS
et co-encadrée par **Arata NAKAJO**, Ingénieur de recherche, EPFL

préparée au sein du **CEA-LITEN** dans **l'École Doctorale I-MEP2**

Fracture of porous ceramics: application to the mechanical degradation of solid oxide cells during redox cycling

Thèse soutenue le **« 30 mars 2022 »**,
devant le jury composé de :

M. Rafael ESTEVEZ
Professeur, Laboratoire de Science et Ingénierie des Matériaux et Procédés (SIMaP), Université Grenoble-Alpes (Président de jury)
M. Henrik Lund FRANDSEN
Directeur de recherche, Department of Energy Conversion and Storage, Technical University of Denmark (DTU) (Rapporteur)
M. Guilhem DEZANNEAU
Directeur de recherche, Laboratoire de Structures, Properties and Modeling of Solids (SPMS), CentraleSupélec (Rapporteur)
M. Dominique LEGUILLON
Directeur de recherche émérite, Institut Jean le Rond d'Alembert, Université Pierre et Marie Curie (UPMC), (Examinateur)
M. Jérôme LAURENCIN
Ingénieur de recherche, CEA-LITEN (Membre, directeur de thèse)
M. Sylvain MEILLE
Professeur, MATEIS (Membre, co-directeur de thèse)
M. Arata NAKAJO
Ingénieur de recherche, EPFL (Invité, co-encadrant)
M. Aurélien DOITRAND
Maitre de conférence, MATEIS (Invité)

“ Live as if you were to die tomorrow.
Learn as if you were to live forever. ”

“ The difference between
the impossible and the possible
lies in a person’s determination. ”

Mahatma Gandhi.

Acknowledgments

I would like to dedicate this page as a sign of my gratitude to all those who supported me during my PhD.

Firstly, special thanks go to my supervisor at CEA Jérôme Laurencin for his continuous encouragement and insightful advice. I would also like to express my thanks to my advisors Sylvain Meille and Arata Nakajo for their help and involvement, especially in the experimental work. Their different backgrounds make working with them very interesting and enriching. I am very grateful for giving me the chance to work on this project, which motivated me a lot from the beginning.

Moreover, I would like to thank all the members of the jury for accepting to evaluate my work. I would like to thank Rafael Estevez for being the president of the jury and for creating a good atmosphere during the question session. I am also grateful to Henrik Lund Frandsen and Guilhem Dezanneau for the effort and the time that they dedicated to reviewing this dissertation. A special thanks go to Dominique Leguillon for his participation in the jury. I would like also to thank him for his contribution to my PhD work. It was a pleasure to have the opportunity to collaborate and discuss with him about fracture mechanics.

Besides, the present work was carried out mostly in the LES laboratory, which is part of the STH2 service at CEA Grenoble. For this reason, I would like to thank Julie Mougin and Cyril Bourasseau, heads of the service and the laboratory, respectively, for allowing me to be part of their team. I would also like to thank all the STH2 colleagues: Marie, Géraldine, Karine, Géraud, Jérôme, Bertrand, Lionel, Denis, Rémi, Amir, Simon, Bastien, Bruno, Philippe…

I also owe my gratitude to all the people with whom I worked at CEA. I thank Pascal for preparing the samples holder for me very quickly, Maxime for his help and precious comments, Nathalie for the polishing and SEM samples preparation, Guillaume for his help in preparing the micro-pillars, Renaud for his help with Unix to launch simulations on the servers, especially during the lockdown…

In addition, I am very grateful to have the chance to have shared the office with very kind people who have brought fun to this experience. They have become more than colleagues but real friends: Elisa, Lydia, Eduardo, Giuseppe, Federico. I am also very glad to have met all the other PhD students and Post-docs during these years: Léa, Manon, Giuseppe, Hamza, Veronica, Paul, Delphine, Yusef, Oumaima, Tika, Ridha, Amandine…

I would like to express my immense gratitude to all my friends in Grenoble for their support and motivation throughout my PhD and more particularly during the last year.

My warmest thanks go to the most precious people in my life: my family, my parents, my brother and my sister-in-law for their love and encouragement.

Finally, I would like to thank my motherland Tunisia for the quality of its education system, which allowed me to succeed in my academic experience in France.

Abstract English

This thesis was dedicated to the development of a relevant numerical tool to predict the fracture in 3D porous ceramics such as the electrodes of Solid Oxide cells (SOCs). For this purpose, the so-called phase-field method (PFM) was adopted. Indeed, this model offers many advantages to take into account the characteristics of real complex electrode microstructures. Because of the lack of fracture properties data on porous Yttria-Stabilized Zirconia (YSZ), micro-mechanical characterizations were carried out to provide experimental results for the model validation. A dedicated protocol from the specimen fabrication and compression up to post-mortem characterization was developed. The compressive fracture strength was measured as a function of porosity and a transition in the fracture mode from a brittle behavior to diffuse damage was detected when increasing the porosity. Moreover, the capacity of the PFM model to accurately predict the crack initiation when the fracture is controlled by a mixed stress-energy criterion was validated. For this purpose, the PFM simulations were compared to the well-established predictions given by the coupled criterion on ideal geometries. Besides, the regularization length scale parameter in the PFM model formulation was found to contain information on the material fracture properties and to depend on the type of the local geometry from which the crack initiates. The relevance of the PFM model to predict the fracture in real porous ceramic microstructures was then assessed by simulating the apparent fracture toughness and the compressive fracture strength as a function of porosity. A good agreement with experimental data was obtained, thus validating the PFM model. Finally, as an illustration of the PFM capability to study the mechanical damage of porous SOCs electrodes, the YSZ skeleton micro-cracking induced by the Ni re-oxidation was simulated. The critical degree of oxidation was calculated considering two typical cermets (Ni-3YSZ and Ni-8YSZ). From this study, the PFM model appears as an efficient tool to analyze the effect of material and microstructural properties on the cermet redox tolerance and, more generally, on the mechanical robustness of porous ceramic-based electrodes.

Résumé Français

Cette thèse a été dédiée au développement d'un outil numérique pertinent pour prévoir la rupture des céramiques poreuses telles que les électrodes des cellules à oxyde solide. Pour ce faire, la méthode dite par champ de phase (PFM) a été adoptée. Cette méthode permet de tenir compte des caractéristiques des microstructures complexes des électrodes. En raison du manque de données des propriétés à rupture de la zircone poreuse stabilisée à l'yttrium (YSZ), des caractérisations micromécaniques ont été réalisées afin de fournir des résultats expérimentaux pour la validation du modèle. Un protocole dédié depuis la fabrication et la compression de l'échantillon jusqu'à la caractérisation post-mortem a été développé. La contrainte à rupture en compression a été mesurée en fonction de la porosité. Une transition dans le mode de rupture d'un comportement fragile à un endommagement diffus a été détecté avec l'augmentation de la porosité. En outre, la capacité du modèle PFM à prévoir précisément l'amorçage d'une fissure, notamment quand la rupture est contrôlée par un critère mixte en énergie et contrainte a été validée. Pour ce faire, les simulations par la méthode par champ de phase ont été comparées aux prédictions obtenues par le critère couplé sur des géométries idéales. De plus, il s'est avéré que le paramètre de régularisation introduit dans le modèle PFM contient les informations sur les propriétés à rupture du matériau et dépend du type de la géométrie locale à partir de laquelle la fissure s'amorce. La pertinence du modèle PFM à prévoir la rupture dans des microstructures réelles de céramiques poreuses a été ensuite évaluée en simulant la ténacité apparente et la contrainte à rupture en compression en fonction de la porosité. Un bon accord avec les résultats expérimentaux a été obtenu validant ainsi le modèle PFM. Finalement, pour illustrer la capacité du modèle PFM à étudier l'endommagement mécanique des électrodes poreuses des cellules à oxyde solide, la microfissuration du squelette zircone induite par la réoxydation du Ni a été simulée. Le degré de réoxydation critique a été calculé sur deux cermets typiques en Ni-3YSZ et Ni-8YSZ. Cette étude a montré que le modèle PFM est un outil efficace pour analyser l'effet des caractéristiques des matériaux et de leurs microstructures sur la tolérance du cermet à la réoxydation, et plus généralement, sur la robustesse mécanique des électrodes à base de céramiques poreuses.

Table of Contents

Résumé étendu en français 7
List of symbols 13
List of Figures 15
List of Tables 19
General Introduction 21
I. Literature Review on Solid Oxide Cell (SOC): mechanical damage in porous ceramic electrodes 27
I.1. SOC principle and reaction mechanisms for the two electrodes 27
I.2. SOC design 29
I.3. SOC materials 30
I.3.1. Electrolyte 31
I.3.2. Oxygen electrode 32
I.3.3. Hydrogen electrode 32
I.4. SOC advantages 33
I.5. SOC degradation mechanisms 33
I.5.1. Physicochemical destabilization of materials 33
I.5.2. Microstructural evolution 34
I.5.3. Mechanical damage 35
I.6. Literature review on Ni re-oxidation 40
I.6.1. Ni re-oxidation of the Ni-YSZ substrate 40
I.6.2. Impact of Ni-reoxidation on the cell mechanical and electrochemical response 44
I.6.3. Numerical works on the mechanical damage of the cell upon redox cycling 48
I.7. Fracture in porous ceramics 50
I.7.1. Apparent fracture toughness and strength 50
I.7.2. Models for porous ceramics 52
I.7.3. Concluding remarks 54
I.8. Conclusions 55
I.9. Objective and methodology of the thesis 56
II. Fracture properties of porous yttria-stabilized zirconia under micro-compression testing 59
II.1. Experiments and methodology 61
II.1.1. Sample preparation 61
II.1.2. Micro-compression testing 63

II.1.3. Microstructural characterizations 64
II.2. Results and discussions 67
II.2.1. Sample preparation 67
II.2.2. Microstructural properties: pore volume fraction and phase size distribution 72
II.2.3. Micro-compression testing results 76
II.2.4. Post-mortem characterizations 81
II.2.5. Sample size effect 84
II.3. Conclusion 85
III. Numerical approach to simulate the fracture in porous ceramic microstructures: the Phase-Field method 87
III.1. State of the art 88
III.1.1. Brief review on numerical approaches for fracture 88
III.1.2. Controversy on the capacity of the Phase-Field method to accurately predict the crack initiation 90
III.2. PFM model description 91
III.3. PFM implementation 95
III.4. Numerical validation of the PFM implementation 96
III.4.1. Single edge notched sample under tensile loading 97
III.4.2. Single edge notched sample under shear loading 98
III.5. Evaluation of the PFM capacity to accurately predict the crack nucleation 99
III.5.1. Methodology 99
III.5.2. Results and discussions 104
III.6. Conclusion 112
IV. Prediction of the crack initiation and propagation in porous ceramic microstructures: experimental validation 115
IV.1. Methodology 116
IV.1.1. Propagation of a preexisting macro-crack in 2D porous ceramic microstructures 117
IV.1.2. Crack nucleation in 3D 118
IV.2. Results and discussions 122
IV.2.1. Apparent fracture toughness of porous ceramics 122
IV.2.2. Fracture of porous ceramic microstructures under compression 127
IV.3. Conclusion 131
V. Simulation of the mechanical damage in the hydrogen electrode induced by Ni re-oxidation 134
V.1. PFM-based model to simulate the fracture induced by Ni re-oxidation 135

V.1.1. Ni re-oxidation modeling 135
V.1.2. Implementation description 136
V.1.3. Methodology 136
V.2. Results and discussion 138
V.2.1. Microstructural properties 138
V.2.2. Results of the PFM simulations 140
V.3. Conclusion 144
VI. Conclusions and perspectives 146
References 152

Résumé étendu en français

Devant la situation alarmante du réchauffement climatique, la transition vers un système énergétique écologique et durable est désormais une préoccupation mondiale actée, d'ores et déjà, par des décisions politiques en faveur des énergies vertes. Les infrastructures mettant en œuvre les énergies renouvelables ont beaucoup évolué. Néanmoins, la nature intermittente de ces énergies, liée aux conditions climatiques, demeure un inconvénient majeur pour la gestion globale du réseau électrique. Dans ce contexte, les convertisseurs électrochimiques associés à l'hydrogène comme vecteur énergétique constituent une technologie très prometteuse pour absorber les pics de production électrique inhérents aux énergies renouvelables afin de réinjecter l'électricité dans le réseau en cas de besoin. L'hydrogène se présente en effet comme un vecteur énergétique avec de grandes perspectives et des potentiels d'applications multisectorielles. Il est l'élément le plus abondant dans l'univers et se distingue par sa densité énergétique massique la plus élevée (120 $MJ.kg^{-1}$). Selon le matériau utilisé pour l'électrolyte et la température de fonctionnement, les systèmes à base de convertisseur électrochimique à hydrogène se classifient en trois grandes familles à savoir les cellules alcalines (40-90 °C), à électrolyte polymère (20-100 °C) et à oxyde solide (600-900 °C).

Les cellules à oxyde solide (SOCs) fonctionnant à hautes températures sont constituées d'un électrolyte dense en zircone stabilisée à l'yttrium (YSZ) séparant une électrode poreuse à hydrogène, formée d'un cermet de nickel et YSZ (Ni-YSZ), et une électrode poreuse à oxygène, habituellement fabriquée à partir d'une pérovskite à conduction mixte. Les SOCs se distinguent par des rendements importants sans l'utilisation de catalyseurs onéreux. De plus, grâce à leur caractère réversible, elles peuvent fonctionner aussi bien en mode pile à combustible qu'en mode électrolyse ce qui les rend parfaitement adaptées pour participer à la gestion des énergies renouvelables. Cependant, leur durée de vie reste à ce jour limitée et doit encore être améliorée avant d'envisager leur déploiement industriel à grande échelle.

Au cours de leur fonctionnent ou des cycles de marche/arrêt, différentes formes de dégradation apparaissent dans les SOCs, à savoir l'évolution microstructurale, la déstabilisation physicochimique des matériaux et l'endommagement mécanique. La formation de fissures est parmi les phénomènes les plus critiques pour la cellule provoquant des pertes significatives de ses performances globales, et impactant par conséquent, sa durée de vie. De ce fait, la robustesse

mécanique des électrodes poreuses, siège des réactions électrochimiques, doit être en particulier améliorée pour augmenter la durée de vie des cellules.

A titre d'exemple, il a été observé que l'électrode à hydrogène est sensible aux cycles d'oxydoréduction du Ni. En effet, au cours de sa réoxydation, le Ni augmente de volume induisant des contraintes en traction élevées dans la microstructure qui génèrent la fissuration locale du squelette YSZ. Les mécanismes d'endommagement associés sont cependant très complexes à analyser car fortement dépendants des caractéristiques microstructurales locales des électrodes poreuses. Par conséquent, la simulation numérique doit constituer une approche pertinente pour mieux appréhender les mécanismes de fissuration des électrodes à base de céramiques poreuses et pouvoir par la suite analyser l'impact des propriétés matérielles et microstructurales sur leur robustesse mécanique. A notre connaissance, jusqu'à ce jour, aucun modèle de simulation 3D de la rupture de céramiques poreuses n'a été expérimentalement validé.

Dans cette optique, cette thèse vise à développer un outil numérique capable de prévoir l'amorçage et la propagation de fissures dans la microstructure complexe et tridimensionnelle d'une céramique poreuse. Le modèle sera *in fine* appliqué pour simuler la fissuration du squelette zircone induite par la réoxydation du Ni dans l'électrode à hydrogène.

Pour ce faire, une méthode dite par champ de phase appliquée à la mécanique de la rupture a été adoptée. Une validation de la capacité du modèle à prévoir précisément l'amorçage d'une fissure a été d'abord menée sur la base des prédictions données par le critère couplé sur des géométries idéales. Après ces vérifications théoriques préalables, le modèle PFM a été appliqué sur des microstructures céramiques poreuses pour reproduire les données expérimentales. Le modèle PFM a été capable de retrouver la décroissance de la ténacité apparente avec la porosité issue de la littérature. Ne disposant pas dans la bibliographie de données expérimentales sur la contrainte à rupture en fonction de la porosité de la zircone yttriée, une étude micromécanique spécifique a été menée à une échelle représentative des électrodes de cellules à oxydes solides. Les résultats expérimentaux de cette étude ont été utilisés pour valider davantage le modèle PFM qui s'est montré capable de reproduire la décroissance de la contrainte à rupture en fonction de la porosité. Il a été ainsi déduit que le modèle PFM dispose des atouts nécessaires pour prévoir la rupture des électrodes poreuses des cellules à oxyde solide.

Les différentes études menées dans le cadre de cette thèse sont exposées dans le présent manuscrit, rédigé sous forme de six chapitres.

Le premier chapitre est dédié à la présentation de la technologie de la cellule à oxyde solide. Le principe général de fonctionnement, les mécanismes de réaction, les différentes architectures et les matériaux classiquement employés dans ce dispositif sont détaillés. De plus, les principaux mécanismes de dégradation de la cellule sont décrits avec une attention particulière portée à la dégradation mécanique de l'électrode à hydrogène. Etant un phénomène complexe et critique pour la cellule, une section entière est consacrée au problème de réoxydation du Ni dans l'électrode à hydrogène, avec une présentation des principaux travaux existants dans la littérature. Cette revue de la bibliographie met en exergue les limitations des approches numériques proposées pour étudier la rupture des électrodes poreuses et plus généralement des céramiques poreuses.

Le deuxième chapitre présente l'étude expérimentale menée à l'échelle de la micromécanique. Le protocole développé allant de la fabrication de micro-échantillons avec une variation contrôlée de la porosité, du test de compression jusqu'à la caractérisation post-mortem est détaillé. Dans cette étude, les échantillons ont été préparés sous la forme de micro-piliers en utilisant un « plasma focused ion beam (PFIB) ». Les spécimens ont été ensuite testés avec un poinçon circulaire à tête plate et la contrainte à rupture a été mesurée sur une large gamme de porosité représentative des électrodes. Il a été constaté que la décroissance de la contrainte critique en compression avec la porosité est décrite par une loi en puissance. D'autres tests ont été menés à des charges légèrement inférieures à la contrainte à rupture pour créer des fissures sans entrainer la rupture complète des piliers. Il a été alors possible d'observer les fissures créées et d'identifier un changement de mécanisme de rupture d'un comportement fragile vers un endommagement diffus à forte porosité. Tous ces résultats expérimentaux ont été utilisés par la suite dans la validation du modèle, qui est l'objet du quatrième chapitre.

Le troisième chapitre décrit et justifie le choix de la méthode dite par champ de phase adopté dans cette thèse pour simuler la rupture des céramiques poreuses. En se basant sur les résultats rapportés dans la littérature, la validation numérique est présentée. La capacité du modèle à prédire avec précision l'amorçage d'une fissure est ensuite évaluée en utilisant comme référence le critère couplé d'énergie et de contrainte sur des géométries idéales (entaille en V et fissure émoussée par un pore). Dans les deux cas d'étude, le modèle PFM se montre capable de reproduire les résultats du critère couplé et de capter le changement du critère à rupture. Une discussion sur la nature du paramètre de régularisation introduit dans l'approche champ de phase a été également menée. Il s'avère que ce paramètre contient les informations sur les propriétés à rupture des matériaux, mais dépend aussi du type de la géométrie locale à partir de

laquelle la fissure s'amorce. Avec ces résultats, le modèle par champ de phase peut être considéré, malgré sa formulation initiale purement énergétique, comme une méthode basée sur un critère à rupture en énergie-contrainte par le biais du paramètre de régularisation.

Le quatrième chapitre répond à l'objectif principal de ces travaux de thèse: développer un modèle pertinent pour étudier la rupture des céramiques poreuses. Ce chapitre présente l'étude qui a permis la validation du modèle PFM sur la base des résultats expérimentaux. Dans cette étude, des microstructures céramiques poreuses 2D avec une fissure existante ont été d'abord simulées et la ténacité apparente en fonction de la porosité a été calculée. Un bon accord avec les données expérimentales rapportées dans la littérature a été obtenu et les mécanismes de propagation d'une fissure existante dans une céramique poreuse ont été analysés. Ensuite, une approche multi-échelle a été mise en place pour simuler les tests de compression sur les micro-piliers. Par ailleurs, le modèle par champ de phase a été appliqué en 3D pour simuler la rupture en compression des microstructures non-endommagées de céramique poreuse. L'évolution de la contrainte critique à rupture en fonction de la porosité a été comparée aux valeurs mesurées expérimentalement et présentées dans le deuxième chapitre. Encore une fois, une bonne adéquation entre les résultats simulés et mesurés a été obtenue. De plus, comme observé dans les expériences, le modèle PFM est capable de détecter le changement du mode de rupture d'un comportement fragile à un endommagement diffus en augmentant la porosité. Ce chapitre permet de conclure alors sur la pertinence et l'efficacité du modèle PFM à simuler l'amorçage et la propagation dans les céramiques poreuses à microstructures complexes.

Le cinquième chapitre est une illustration de la pertinence pratique du modèle par champ de phase à prévoir la rupture dans les électrodes poreuses des cellules à oxyde solide à base de céramique. Pour ce faire, la microfissuration du squelette zircone induite par la réoxydation du Ni a été simulée. Une analogie basée sur la dilatation thermique a été adoptée pour modéliser l'expansion de volume du Ni au cours de sa réoxydation. Il est à noter que cette simplification est valide uniquement pour simuler les premiers degrés de réoxydation. Cette étude a montré que la fissuration de la zircone yttriée apparait pour des taux de réoxydation faibles, en accord avec les pertes de performances électrochimiques souvent observées dès les premiers degrés de réoxydation. Deux microstructures typiques du cermet ont été simulées (Ni-3YSZ et Ni-8YSZ) permettant de confirmer davantage l'efficacité du modèle PFM à analyser l'effet des propriétés matérielles et microstructurales sur la tolérance du cermet à la réoxydation, et plus généralement, sur la robustesse mécanique des électrodes à base de céramiques poreuses.

Le dernier chapitre synthétise les résultats obtenus dans le cadre des travaux de cette thèse et ouvre les perspectives pour des études futures. A titre d'exemple, il a été proposé en perspective d'étudier des géométries synthétiques 3D idéales présentant des caractéristiques microstructurales bien définies et contrôlées (réseau de sphères par exemple). Le modèle PFM devrait être alors en mesure d'établir des relations pertinentes entre le paramètre de régularisation et les propriétés morphologiques. De plus, il serait possible de mieux comprendre et analyser les mécanismes de rupture dans les céramiques poreuses si des données expérimentales sont fournies sur des microstructures idéales similaires pour la validation. Concernant la fissuration de l'électrode à hydrogène induite par la réoxydation du Ni, une approche plus rigoureuse qui prend en compte la transformation Ni/NiO est requise pour pouvoir simuler des degrés de réoxydation élevés, ce que ne permet pas l'hypothèse de l'analogie de dilatation thermique. De plus, des expériences dédiées sont nécessaires pour pouvoir valider le degré de réoxydation critique calculé par le modèle. Disposant d'un modèle valide pour décrire convenablement la réoxydation du Ni, l'impact des propriétés matérielles et microstructurales sur la tolérance du cermet à la réoxydation pourrait être par conséquent évalué et une recommandation de microstructure optimale pour une électrode ayant de meilleures propriétés à rupture pourrait être proposée. Finalement, en vue de quantifier la perte des performances globales de la cellule provoquée par la formation des microfissures, une approche multiphysique, consistant à coupler le modèle par champ de phase avec un modèle électrochimique, doit être mise en place. En guise de conclusion, un modèle qui repose sur une bonne compréhension et maîtrise des mécanismes de fonctionnement et de dégradation de la technologie des cellules à oxyde solide est indispensable pour pouvoir identifier des solutions pertinentes conduisant à l'amélioration de sa durée de vie.

List of symbols

a_c	crack length	(mm or µm)
a_n	notch depth	(mm)
L	beam length	(mm or µm)
h	beam height	(mm or µm)
b	beam thickness	(mm or µm)
r	cavity radius	(mm)
δ_c	crack width	(µm)
λ	singularity order	(-)
β	notch angle	(degrees)
ε	porosity	(%)
K_{Ic}^{notch}	apparent fracture toughness for the notch	(MPa $m^{1-\lambda}$)
K_{Ic}^{app}	apparent fracture toughness for the crack blunted by a cavity	(MPa.√m)
K_{I}	generalized stress intensity factor	(MPa $m^{1-\lambda}$)
K_{Ic}	material fracture toughness	(MPa.√m)
R	relative toughness	(-)
F_{c}	applied critical loading	(N)
G_{c}	critical energy release rate	(J m^{-2})
G_{inc}	incremental energy release rate	(J m^{-2})
W_p	potential energy	(J)
σ_c	material strength	(MPa)
σ_0	applied stress	(MPa)
σ_0^c	critical applied stress	(MPa)
k, A	dimensionless coefficients	(-)
Λ	scaling coefficient	(MPa^{-1})
D	scaling coefficient	($MPa^{-0.5}$)
E	Young modulus	(MPa)
$\hat{E}$	Young modulus for the plane strain condition	(MPa)
ν	Poisson coefficient	(-)
d	phase-field variable	(-)
g	degradation function	(-)
t	time	(s)
E_s	stored energy	(J)
W_c	energy dissipation	(J)
P_c	work of external forces	(J)
π	potential energy	(J)
Ψ	elastic strain energy	(J m^{-3})
Ψ^+	strain energy related to tension contribution	(J m^{-3})
$\mathcal{H}$	'history' loading field	(J m^{-3})
f	thermodynamic driving force	(J m^{-3})
ℓ	regularization length scale parameter for the phase-field approach	(mm or µm)
ℓ_{8YSZ}	length scale parameter for the 8YSZ material	(mm or µm)
ℓ_{3YSZ}	length scale parameter for the 3YSZ material	(mm or µm)
l_{Irwin}	Irwin length	(µm)

l_{Irwin}^{8YSZ}	Irwin length for the 8YSZ material	(mm or µm)
l_{Irwin}^{3YSZ}	Irwin length for the 3YSZ material	(mm or µm)
l_0	initial crack length for the coupled criterion	(mm or µm)
l_0^c	critical initial crack length	(mm or µm)
$l_0^{c,8YSZ}$	critical crack length for the 8YSZ material	(mm or µm)
$l_0^{c,3YSZ}$	critical crack length for the 3YSZ material	(mm or µm)

List of Figures

Fig I- 1. Operating principle in (a) electrolyzer and (b) fuel cell modes. 29
Fig I- 2. Solid Oxide Cell designs: (a) planar and, (b) tubular [11] (illustrated here in SOFC mode with air and fuel supplied to the cell. In this case, the anode and cathode are the H_2 and O_2 electrodes, respectively). 30
Fig I- 3. Ionic conductivity of 3YSZ and 8YSZ as a function of temperature in air [15]..... 31
Fig I- 4. Oxygen electrode delamination in: a) electrolyte-supported cell [35], b) hydrogen electrode-supported cell [39]. 36
Fig I- 5. (a) LSCF-based O_2 electrode imaged by FIB-SEM serial sectioning after segmentation. (b) Close-up view in the EsB grayscal data showing cracks. (c) 3-D view of the cracks detected in the imaged sample volume [49]. 37
Fig I- 6. Different forms of mechanical degradation induced by Ni re-oxidation: a) electrolyte fracture observed on a scanning-electron microscopy (SEM) cross-section [52], b) cracks observed at the surface of the electrolyte [52], c) micro-cracks within the YSZ skeleton observed on a focused ion beam-scanning electron microscopy (FIB-SEM) cross section [53], d) microstructure before and after re-oxidation observed by X-ray nanotomography, showing the formation of micro-cracks within the YSZ skeleton after re-oxidation [54], e) cracks observed at the interface electrolyte-anode functional layer and anode functional layer-current collector layer [48]. For a), b), c) and d), the re-oxidation was conducted in air and by an ionic current for e). 39
Fig I- 7. Cermet redox strain measured by: a) dilatometry as a function of degree of oxidation [56], b) image analysis as a function of number of redox cycles [53]. 42
Fig I- 8. Degree of oxidation as a function of air flow rate for two operating temperatures (600°C and 800°C) [40]. 43
Fig I- 9. Degree of oxidation as a function of air flow rate for two different microstructures with porosities of 48% and 33% at operating temperatures of 800°C for 15 min [40]. 43
Fig I- 10. Oxidation gradient observed at a DoO of 41.7% in a cermet support oxidized in air at 800°C. The NiO/Ni ratio of the intensity peaks of X-ray diffraction is plotted on the left as a function of the axial location in the cermet. On the right, the SEM micrograph is depicted showing a difference of microstructure including porosity between the oxidized and the reduced states [60]. 44
Fig I- 11. Evolution of the residual stress in the electrolyte as a function of degree of oxidation (DoO) for oxidation temperature of 800°C. X-Ray Diffraction measurements were performed at room temperature [40]. 45
Fig I- 12. Evolution of electrochemical performances of anode-supported cell upon redox cycling for three temperatures (800°C, 700°C and 600°C): a) normalized power density, b) open current voltage [40]. 47
Fig I- 13. Decrease of the measured a) bending strength of porous alumina [69], b) fracture toughness of the yttria stabilized zirconia with the porosity [75]. 51
Fig I- 14. Comparison of the computed a) tensile strength, b) normalized flexural strength with the experimental data. Simulations using a fracture stress criterion on microstructures generated by a) discrete element method (DEM) [97], b) lattice element model [87]. 54
Fig I- 15. Overview of the methodology of the thesis: multi-scale approach coupling modeling and micro-scale experiments. 57

Fig II- 1. Procedure for micro-pillar preparation: a) schematic representation of the Xe^+ pFIB, b) example of a typical specimen obtained after the milling. 63
Fig II- 2. Specimen preparation procedure for X-ray tomography: a) fixation of the micromanipulator on the pillar, b) extraction of the pillar from the pellet, c) pillar moved by the micromanipulator to the invar pin, d) pillar mounted on the invar pin. 67
Fig II- 3. Secondary electrons SEM micrographs of 8YSZ samples prepared by partially sintering under air at: a) 1270°C, b) 1230°C, c) 1200°C, d) 1150°C. e) and f) SEM observations of the 8YSZ sample obtained by dissolving the Ni present in a cermet substrate for two magnifications. The insert in Fig. 3a shows the pellet after sintering. 68
Fig II- 4. Porosity gradient in the sample sintered at 1270 °C. 69
Fig II- 5. Comparison between two FIB-SEM secondary electron cross-sections of microstructures obtained after dissolution of the Ni: a) with defects (highlighted by red and yellow rectangles), b) without defects (i.e. obtained by the validated protocol). 70
Fig II- 6. 3D rendering segmented volumes of FIB-SEM reconstructions of porous 8YSZ samples sintered at: a) 1270°C, b) 1150°C and of the whole X-ray holotomography reconstructions for c) highly porous 3YSZ, d) highly porous 8YSZ samples. 71
Fig II- 7. FIB-SEM segmented reconstructions of the sample sintered at 1270°C: a) illustration of the two regions of interest, 3D rendering volumes extracted from the whole FIB-SEM reconstructions b) Reconstruction 2: nearby the well in which the pillar is centered, c) Reconstruction 1: in the pillar. 72
Fig II- 8. Particle size distributions of the solid and porous phases of: a) 8YSZ samples sintered at 1270°C (porosity: 33%) and 1150°C (49%), b) highly porous 8YSZ sample (63%), c) highly porous 3YSZ sample (63%). 75
Fig II- 9. Load-displacement curves recorded for samples sintered at: a) 1270°C (porosity: 33%), b) 1230 (36%), c) 1200°C (40%), d) 1150°C (49%) and highly porous specimens (63%) made of: e) 3YSZ, f) 8YSZ. 77
Fig II- 10. Young's modulus as a function of porosity for 8YSZ porous ceramics. Comparison with the modified exponential model proposed in [132] considering a Young's modulus of E_0 = 216 GPa for dense 8YSZ [103] and an intrinsic elastic modulus E = 2.2 [132]..... 78
Fig II- 11. Stress-strain response for the 8YSZ micro-pillars sintered at: a) 1270°C (porosity: 33%), b) 1230 (36%), c) 1200°C (40%), d) 1150°C (49%) and for the highly porous specimens (63%) made of: e) 3YSZ, f) 8YSZ. Fracture stress is marked with a star. The zone surrounded by the dashed line in e) and f) shows non-linearity in the stress strain curve before fracture. 79
Fig II- 12. Compressive fracture strength as a function of porosity in 8YSZ ceramics, fitted by a power law model. 80
Fig II- 13. Ex-situ characterization after mechanical loading of the 8YSZ pillar sintered at 1270°C (porosity: 33%): a) SEM image of a longitudinal crack on the edge of the pillar, b) SEM image of the tested pillar, c) FIB-SEM cross section showing the large crack in the bulk of the pillar. 82
Fig II- 14. Ex-situ characterization of the highly porous (porosity: 63%) pillars after the mechanical loading with a zoom showing micro-cracks in the bulk of the pillar (highlighted by red rectangles): a) 8YSZ, b) 3YSZ. The tests were stopped before the fracture..... 83

Fig III- 1. Sharp and diffuse crack description..... 92

Fig III- 2. Geometry of the single edge notched sample as reported in the work of Miehe et al. [136] subjected to: a) tension and b) shear loadings. 97
Fig III- 3. Phase field reasults for a single edge notched sample under tensile loading: pattern crack with a) ℓ_1= 0.015 mm, c) ℓ_2= 0.0075 mm and load-displacement response with b) ℓ_1= 0.015 mm, d) ℓ_2= 0.0075 mm. The insert in (b) and (d) corresponds to the results reported in Miehe et al. [13]. 98
Fig III- 4. Phase field reasults for a single edge notched sample under shear loading: pattern crack with a) ℓ_1= 0.015 mm, c) ℓ_2= 0.0075 mm and load-displacement response with b) ℓ_1= 0.015 mm, d) ℓ_2= 0.0075 mm. The insert in (b) and (d) corresponds to the results reported in Miehe et al. [13]. 99
Fig III- 5. Three-point-bending test on a V-notched sample. 101
Fig III- 6. Three-point-bending test on a sample with a crack blunted by a cavity. 102
Fig III- 7. Applied loading as a function of crack length obtained using the stress (in blue) and the energy (in purple) criteria. The coupled criterion is chosen among the admissible solutions such that l_0^c minimizes the applied loading σ_0^c (in red). 103
Fig III- 8. Visualization of the crack pattern initiated from a notch at an opening angle 2β of 90° for: a) ℓ_1 = 0.01 mm, b) ℓ_2 = 0.04 mm. c) Force-Displacement curves considering the 8YSZ material at a V-notch angle 2β of 90° for ℓ_1 = 0.01 mm and ℓ_2 = 0.04 mm. 105
Fig III- 9. Dependence of the mechanical response of the V-notched 8YSZ sample on the opening angle considering different values of the length scale parameter ℓ: a) apparent fracture toughness, b) critical force triggering crack initiation. ℓ_{8YSZ} refers to the length scale parameter that provides close agreement between the coupled criterion and the PFM results over the whole considered range of notch angles, c) force-displacement curves at a V-notch angle 2β of 120°. 108
Fig III- 10. Dependence of the apparent fracture toughness on the opening angle for the 3YSZ material considering different values of the length scale parameter ℓ. ℓ_{3YSZ} refers to the length scale parameter that provides close agreement between the coupled criterion and the PFM results over the whole considered range of notch angles. 109
Fig III- 11. The dependence of the relative toughness on the cavity radius considering different values of the length scale parameter ℓ for: a) 8YSZ material, b) 3YSZ material. ℓ_{8YSZ} and ℓ_{3YSZ} refer to the length scale parameters that provide close agreement between the coupled criterion and the PFM results over the whole considered range of cavity radii. 111

Fig IV- 1. Synthetic porous microstructures with different pore volume fractions ε (solid phase in grey): a) 10%, b) 20%, c) 30%. 118
Fig IV- 2. Meshed 8YSZ microstructures at a porosity of: a) 33 %, b) 36 %, c) 40 %, d) 49 % and e) 63 %. 120
Fig IV- 3. Mesh of the tapered pillar attached to the pellet with axisymmetric conditions. A zoom on the pillar is shown together with the location of the Volume Of Interest (VOI) for the simulation at the microstructure scale using the meshes shown in Fig. IV-2. 121
Fig IV- 4. Cartographies displaying crack paths within the porous microstructures: a) first realization at ε (porosity) = 20%, b) second realization at ε = 20%, c) first realization at ε = 10%. (ℓ_{3YSZ}= 0.1 µm). 123
Fig IV- 5. Comparison between two generated synthetic microstructures with ε = 20%: a) visualization of the two realizations of the microstructure, b) Solid phase size distributions (2D) computed on the two realizations. 124

Fig IV- 6. Experimental and simulated dependences of the apparent fracture toughness on porosity using a) the two computation methods for realization 1, b) “method 1” for the two realizations. 126
Fig IV- 7. Comparison between the calculated compressive fracture strength and the experimental data [161] as a function of porosity. 128
Fig IV- 8. Visualization of the cracks created in porous microstructures submitted to compression: First micro-cracks created in the microstructure with a porosity of a) 33 % and b) 63 %. Evolution of the damage variable after a small increment of charge at c) 33 % and d) 63 % (ℓ = 0.4 µm). 129
Fig IV- 9. Evolution of the density of elastic strain energy as a function of porosity (ℓ = 0.8 µm). 130

Fig V- 1. Meshes of the computation domain illustrated for the total volume and for each phase separately: a) Ni-8YSZ, b) Ni-3YSZ. 137
Fig V- 2. Particle size distribution (PSD) of: a) Ni-8YSZ and b) Ni-3YSZ microstructures. 139
Fig V- 3. Meshes of the simulated Ni-YSZ volumes of 2^3 µm^3: a) Ni-8YSZ, c) Ni-3YSZ. Micro-cracks simulated by PFM in b) Ni-8YSZ, d) Ni-3YSZ at a critical degree of oxidation of 3% and 11%, respectively. 141
Fig V- 4. Meshes of the simulated solid phases in the Ni-YSZ volumes of 5^3 µm^3: a) Ni-8YSZ, c) Ni-3YSZ. Micro-cracks simulated by PFM in b) Ni-8YSZ, d) Ni-3YSZ. 143

List of Tables

Table II- 1. Microstructural properties of the investigated samples computed on 3D reconstructions. 73
Table II- 2. Mechanical properties of the investigated samples under micro-compression testing. 81

Table III- 1. Mechanical properties of 3YSZ and 8YSZ. 100

Table V- 1. material properties used for the simulations. 136
Table V- 2. Microstructural properties of the Ni-8YSZ and Ni-3YSZ cermet supports computed on 3D reconstructions. 138

General Introduction

1. Motivation

In the last decade, natural calamities have become more frequent and destructive (hurricanes, wildfires, floods, etc.). Researchers explain these events by the climate change and global warming effects, thus pointing out the urgent necessity to reduce greenhouse gas emissions (Fig. 1). The massive utilization of fossil fuels (oil, coal and natural gas) is considered as the main source of the CO_2 release in the atmosphere. Indeed, the CO_2 emissions from the global energy sector were estimated to 32 Gt with a significant part coming from power generation (42%) [1].

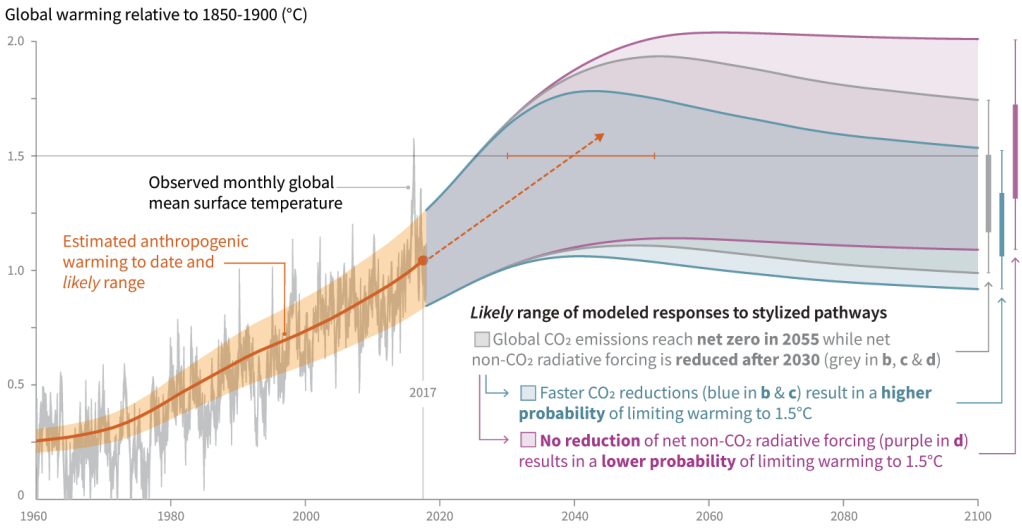

Fig 1. Evolution of the global temperature with two CO_2 emissions scenarios: faster CO_2 reduction and no CO_2 reduction [2].

Accordingly, political awareness for this environmental problem and more specifically for the development of an eco-friendly and sustainable energy system is raising. In 2015, the Paris agreement on the climate change fixed a target to maintain the increase in global average temperature below 2°C above pre-industrial levels [1]. To reach this objective, serious measures must be taken worldwide for an efficient energy transition process.

Electricity is identified as the key for the energy system transition by decarbonizing power generation and by electrifying different sectors such as those related to transport [3].

Renewable energies are therefore presented as the guarantee for the decarbonisation of the electricity production. However, because of their intermittent nature related to weather conditions (except for biomass), they cannot provide a stable energy system. For example, solar energy is stopped once the sun disappears meaning that an overproduction is expected during the day while a deficit occurs during the night. On the other hand, wind turbines are highly dependent on a suitable wind speed to generate electricity. For instance, a lack of wind over the summer of 2021 has forced UK to rely more on fossil fuel aggravating the crisis due to the oil price surge [4].

The challenge is thus to find technological solutions to compensate the fluctuations in power generation for the efficient integration of renewable energy. Therefore, a main goal is to identify a flexible energy system that would be able to store electricity during peaks of overproduction and reinject electricity in the grid when necessary.

In this perspective, electrochemical conversion technologies associated to hydrogen as an energy vector appears as a promising solution. Firstly, hydrogen is the most abundant element in the universe providing the highest ratio of chemical energy to mass (120 $MJ.kg^{-1}$). Secondly, technological systems based on electrochemical devices can be operated in both electrolysis and fuel modes. Using water electrolysis, they enable converting electricity into hydrogen, which can be then stored in different forms: gas, liquid, or solid. In fuel cell mode, the electrochemical device consumes hydrogen to generate electricity with zero carbon emission. The hydrogen system provides thus a low carbon hydrogen-power production, which fall in line with the decarbonisation objective. Accordingly, in these last years, hydrogen has received an awesome interest. In 2017, a long-term vision for the development of the hydrogen economy was presented in the frame of the international industrial initiative “Hydrogen Council” [5]. This event gathered industrial leaders in the fields of energy and transport. Moreover, several countries such as Japan, China, Korea and France have committed to energy transition advances

through policies that allocate huge budgets, in particular for the integration of hydrogen into the energy system. Finally, research organisms have risen the effort in the hydrogen field, as shown by the increase in the number of publications per year and the enhancement of the hydrogen technologies. The ongoing synchronization between researchers, political decision-makers as well as industrial stakeholders is making the process of developing the hydrogen economy more efficient.

To date, three main types of devices for the electrochemical conversion of hydrogen have been developed. They are commonly classified according to the electrolyte material and the operating temperature. The alkaline and the Proton Exchange Membrane (PEM) technologies work at low temperature, (*i.e.* 20-100 °C and 40-90 °C for PEM and alkaline cell respectively). These two technologies are the most mature and commercialized ones. Solid Oxide Cells (SOC), which are made of ceramic materials, operates at high temperature (*i.e.* 600-900 °C) and are still in research and prototyping phase. Nonetheless, SOC presents many advantages and is considered nowadays as an attractive technology with promising perspectives and multi-sectorial potential. Due to the high operating temperatures, they can reach very high efficiency without using expensive electro-catalysts for the electrochemical reactions. Besides, beyond hydrogen, other gas such as alkanes, alcohols and ammonia can be used as fuels to produce electricity. Finally, SOCs offer very good reversibility in both fuel and electrolysis modes, which makes this technology well adapted for integration in renewable energy systems. Despite these advantages, its industrial deployment is hindered by lifetime limitations. Indeed, different forms of degradation such as microstructural evolution, chemical reactivity and mechanical damage can arise during operation resulting in a decrease of the global cell performances. The formation of cracks within the cell is found to be one of the most detrimental phenomenon, leading to considerable shortening of the cell lifetime. Therefore, a better understanding of the mechanism of fracture along with a deeper knowledge of the mechanical properties of SOC materials are a prerequisite to improve the durability of the device for widespread commercialization.

Among the different mechanical degradations, the damage in the porous electrodes is especially problematic as it affects the efficiency of the electrochemical reactions. However, the damage mechanisms in porous ceramic electrodes is complex and highly dependent on their 3D microstructures. From this point of view, the modeling should constitute a relevant approach to better understand the mechanical degradation phenomena in the porous electrodes. To date,

only few numerical models have been developed to predict the fracture of porous ceramics. None of them has been yet fully validated on real and representative microstructures.

In this context, the objective of the present work is to develop and validate a modeling framework able to predict the crack initiation and propagation in porous ceramics electrodes. The validated model is illustrated by studying the mechanical degradation of the so-called solid oxide cell hydrogen electrode upon redox cycling.

2. Outline of the manuscript

The first chapter is dedicated to the state-of-the-art of the solid oxide cell technology. The general operating principle, reaction mechanisms, different designs and classical materials employed in this device are detailed. In addition, the main mechanisms of degradation of the cell are described in general with a specific attention paid to the so-called hydrogen electrode mechanical degradation. The re-oxidation phenomenon, which severely affects state-of-the-art Ni-based hydrogen electrode, is more specifically detailed. A literature review of the existing studies is presented highlighting the limitation of the proposed numerical approaches to predict the mechanical damage of porous electrodes and, more generally, in porous ceramics. Finally, the objective and the methodology of the thesis are exposed.

The second chapter is devoted to the mechanical characterization of porous YSZ ceramics. The developed experimental methodology, from sample preparation up to microstructural characterization after testing, is detailed. The results are discussed and presented with an emphasis on the data required for the validation of the modeling approach.

The third chapter describes and justifies the selection of the so-called Phase-Field method to simulate the fracture of porous ceramics in this thesis. The numerical validation based on the results reported in the literature is then presented. The capacity of the model to accurately predict the fracture nucleation is evaluated using the established so-called stress and energy coupled criterion as reference.

The fourth chapter reports the comparison between the numerical predictions and the experimental results. Firstly, the model is used to simulate the propagation of an existing crack in 2D porous ceramic microstructures. The computations are confronted to the experimental data available in the literature. Secondly, the simulations of the nucleation and propagation of fracture in pristine 3D porous ceramic microstructures are compared to the results of the second

chapter using a multi-scale approach. Finally, the relevance of the model to simulate the fracture in porous ceramics is assessed.

In the fifth chapter, the simulation of the mechanical damage of the hydrogen electrode upon redox cycling is analyzed and the results are discussed.

The main findings and conclusions of the present thesis along with the perspectives for future studies are synthesized in the last chapter.

I. Literature Review on Solid Oxide Cell (SOC): mechanical damage in porous ceramic electrodes

This chapter provides an overview of the Solid Oxide Cell (SOC) technology. Firstly, the operating principle is presented in both fuel and electrolysis modes. Then, the different architectures existing in market are described and the classical materials used for each component are detailed. Afterwards, the main advantages of this technology are reported. The prominent degradation phenomena limiting the SOC lifetime and consequently its commercialization are described with a focus on the electrode mechanical damage. As an illustration, the H_2 electrode degradation induced by redox cycling is more specifically detailed. The complexity of fracture behavior and modeling of porous ceramics such as the typical SOC electrodes is also addressed in the chapter. Accordingly, the general context of the thesis is exposed. The objective as well as the methodology adopted in the present work are detailed.

I.1. SOC principle and reaction mechanisms for the two electrodes

Associated to hydrogen as an energy vector, the SOC technology offers promising perspectives in the field of energy. It is a high temperature electrochemical energy conversion device able to operate with zero carbon waste under two modes: as a fuel cell (SOFC) to generate electricity

or as an electrolyzer cell (SOEC) to produce hydrogen. Therefore, it appears as key for the efficient integration of intermittent renewable energies (*e.g.* solar or wind). Indeed, the same device can be used to store the surplus electricity production in the form of hydrogen that can be used as fuel when the demand is higher than the production. Moreover, for stationary applications, residential combined heat and power fuel cell-based systems are receiving an awesome interest. For the mobility sector, solid oxide fuel cell is also gaining ever increasing attention with the first prototypes for maritime applications [6]. Accordingly, the SOC technology is presented as eco-friendly with multi-sectorial potential.

SOC is composed of a dense electrolyte sandwiched between two porous electrodes. The SOC operating principle is presented in Fig. I-1. In fuel cell mode (SOFC), the dioxygen is reduced (eq. I-1) at the so-called oxygen electrode resulting in oxygen ions O^{2-} that migrate through the electrolyte towards the so-called hydrogen electrode. The dihydrogen is then oxidized by reacting with the oxygen ions (eq. I-2) producing steam and electrons. As a result, the produced electricity goes through an external circuit connecting the two electrodes. The global reaction in SOFC mode is deduced from the two half reactions, which take place in each electrode (eq. I-3).

In electrolysis mode (SOEC), the reactions are reversed. The system input are in this case current and steam. On the hydrogen electrode side, water molecules are reduced (eq. I-2) forming dihydrogen gas and oxygen ions. The latter are transported by the electrolyte up to the oxygen electrode where they are oxidized giving dioxygen gas (eq. I-1). The global electrochemical reaction, which governs the operating principle of the cell in electrolysis mode, is deduced from the two half reactions occurring in each electrode (eq. I-3).

$$\tfrac{1}{2}\,O_2 + 2\,e^- \underset{SOFC}{\overset{SOEC}{\leftrightarrows}} O^{2-} \qquad \text{(I-1)}$$

$$H_2 + O^{2-} \underset{SOFC}{\overset{SOEC}{\leftrightarrows}} H_2O + 2\,e^- \qquad \text{(I-2)}$$

$$H_2 + \tfrac{1}{2}\,O_2 \underset{SOFC}{\overset{SOEC}{\leftrightarrows}} H_2O \qquad \text{(I-3)}$$

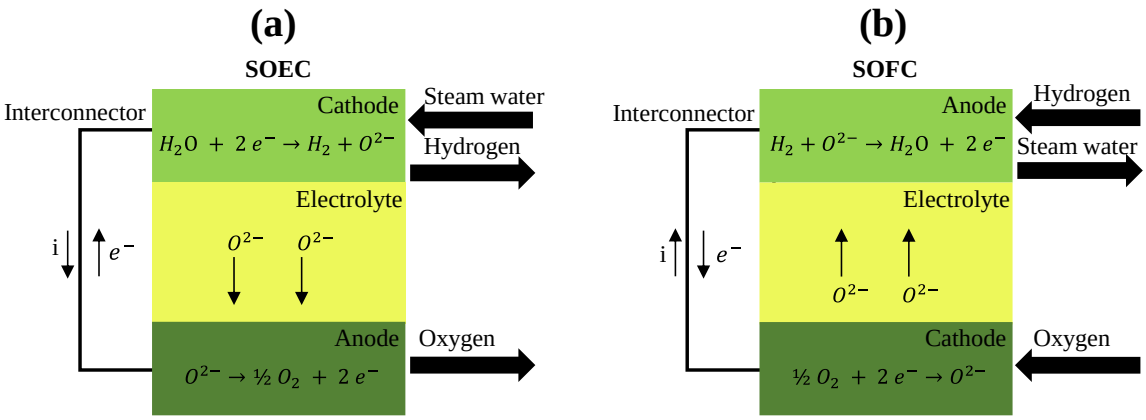

Fig I- 1. Operating principle in (a) electrolyzer and (b) fuel cell modes.

I.2. SOC design

The gas distribution and current collection are dependent on the cell design. Two main SOC architectures exist: planar and tubular (Fig. I-2).

In the tubular architecture, the cell is constituted of concentric tubes associated to the electrolyte and the two electrodes. The hydrogen electrode is in most cases situated in the external part of the cylinder while the oxygen electrode is positioned in the inner part. The current is collected by an interconnect in ceramic material deposited all along the tube as shown in Fig. I-2b. The cells are then assembled in bundles to form high power system. This design offers good mechanical robustness with a simple and efficient solution for the tube sealing. However, significant ohmic losses affecting performance, component production and in-series stacking complications are inherent to this design. Therefore, the tubular cell architecture is often considered economically less attractive comparing to the planar one [7,8].

In the planar architecture, the cell is formed of three layers associated to the electrolyte and the two electrodes. This design stands out by the different possibilities to distribute hydrogen and oxygen gas. Depending on the cell geometry, radial-flow configuration is attributed to circular cell while parallel co-flow or counter-flow or cross-flow configurations are used for parallelepiped cell. Furthermore, three configurations for the planar design are proposed depending on the layer providing the mechanical support of the cell (*i.e.* layer having the highest thickness): hydrogen electrode supported cell, oxygen electrode supported cell, or electrolyte supported cell. To date, the most common configuration is the hydrogen electrode supported cell as it provides the best tradeoff between electrochemical performances, mechanical robustness and manufacturing cost [9]. It is to be noted that, for this cell configuration, the

thickness of the hydrogen electrode, oxygen electrode and electrolyte is classically around 250-400 µm, 30-60 µm and 8-10 µm, respectively [10]. As shown in Fig. 3a, the cells are assembled with metallic interconnects that ensure the current collection and gas distribution in the cells. The cell along with the interconnect plates is called the Single Repeat Unit (SRU) which is assembled in-series to form a stack of desired power.

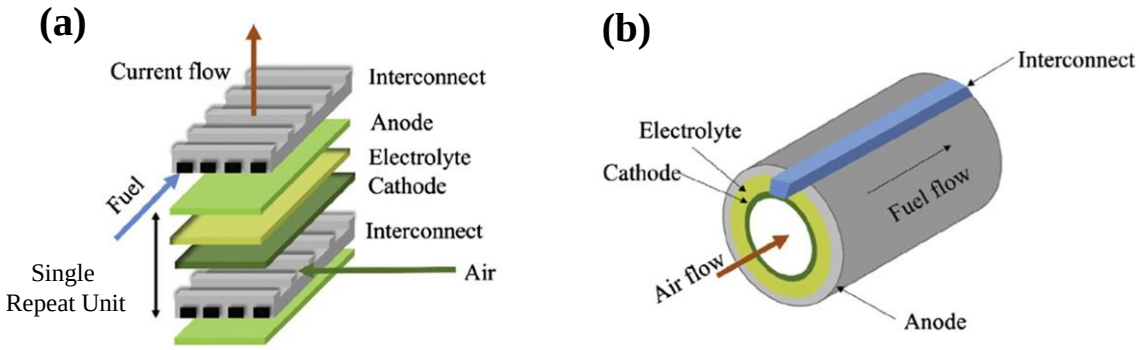

Fig I- 2. Solid Oxide Cell designs: (a) planar and, (b) tubular [11] (illustrated here in SOFC mode with air and fuel supplied to the cell. In this case, the anode and cathode are the H_2 and O_2 electrodes, respectively).

I.3. SOC materials

The selection of materials forming the cell stems from the role of each component (electrolyte, oxygen electrode, hydrogen electrode) as well as from the operating environment conditions. The three components constituting the cell present some common requirements. Firstly, materials should be mechanically and chemically stable under high operating temperature and oxidizing-reducing environments. Secondly, a compatibility in terms of thermal expansion coefficients and absence of chemical reactivity between the materials of the different cell components is required. Finally, materials should be chosen in such a way to guarantee competitive fabrication costs. In addition, each component requires materials with specific properties, essential for its functioning. For the electrolyte, a dense material with high ionic and negligible electronic conductivity is required, providing the gas sealing between the two electrodes, the efficient transport of oxygen ions and the conduction of electrons through the external circuit. For the porous electrodes, both electronic and ionic conductivity are required. Moreover, high electro-catalytic activity is necessary to promote the electrochemical reactions at high temperature. Regarding the pore volume fraction, an adequate balance between effective solid-state and gas-phase transport properties and density of electro-catalytic sites is classically achieved around 30-49 % and 26-33% for the oxygen and hydrogen electrode, respectively [10,12].

I.3.1. Electrolyte

The role of the electrolyte is threefold: firstly, the transport of the oxygen ions controlling the operating principle of the cell; secondly, a perfect gas sealing between the two electrodes; and thirdly, avoiding electronic conductivity between the two electrodes, which are only connected via an external circuit. To fulfill these functions, materials based on fluorite oxides (*e.g.* doped ceria CeO_2 and stabilized zirconia ZrO_2) and on perovskites (*e.g.* doped lanthanum gallate $LaGaO_3$) are considered as candidates [13]. To date, the electrolyte is commonly made of Yttria Stabilized Zirconia (YSZ), distinguished by its low cost and high electrochemical stability over a wide range of oxygen partial pressures compared to other materials. Yttria is used as dopant to stabilize the tetragonal or cubic structure and create vacancies, through which oxygen ions are conducted, thus enhancing the ionic conductivity [14]. This can be, for instance, seen in Fig. I-3 where the comparison of the ionic conductivity between the stabilized zirconia with 3% and 8% molar of yttria (3YSZ and 8YSZ) is depicted [15].

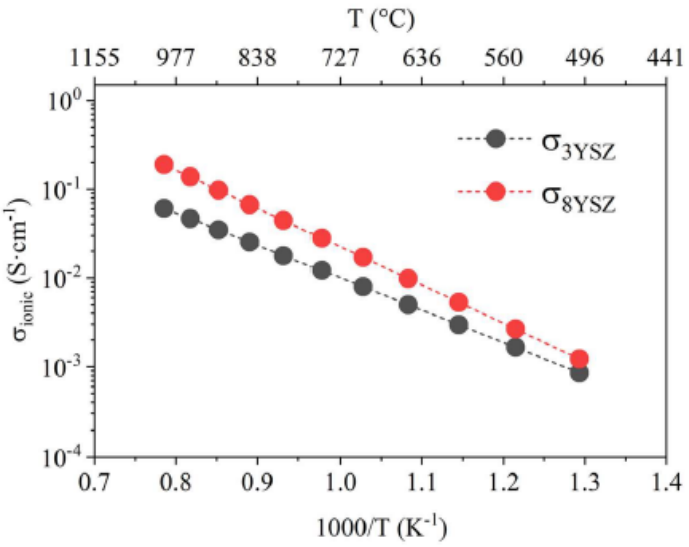

Fig I- 3. Ionic conductivity of 3YSZ and 8YSZ as a function of temperature in air [15]

It has been found that the maximum ionic conductivity is reached for around 8.5-9% molar of yttria. However, a low yttria doping rate provides a better mechanical robustness of the ceramic [16]. Therefore, a compromise between ionic conductivity and mechanical properties should be found based on the targeted properties, which are dependent on the selected SOC design. For example, the material chosen for the electrolyte in the hydrogen electrode supported cell configuration is classically made of stabilized zirconia with 8% molar of yttria (8YSZ) [17]. It exhibits higher ionic conductivity as well as sufficient mechanical robustness for this design,

thus considered to be the most promising tradeoff in terms of electrochemical performance, durability of the cell and costs, from the standpoint of the compatibility with other stack components.

I.3.2.Oxygen electrode

In the electrodes, the electrochemical reactions take place in active sites corresponding to the so-called triple phase boundaries (TPB). The latter correspond to locations where the ionic, electronic and gas conductors are in contact. Therefore, a composite material should be selected to simultaneously provide high electronic and ionic conductivity. Because of the oxidizing atmosphere at the oxygen side, it is not possible to use a metal as electronic conductor. The composite of Lanthanum Strontium Manganite (LSM) and YSZ was traditionally used offering good properties of catalytic activity, ionic and electronic conductivity [18]. Nevertheless, higher electrochemical performance can be achieved by increasing the number of TPB. Therefore, the use of mixed ionic and electronic materials is a solution allowing electrochemical reactions to take place over the whole surface of the porous electrode. Several materials are proposed, among which the Lanthanum Strontium Cobalt Ferrite (LSCF) perovskite is nowadays the most common material for the oxygen electrode [19]. However, it has been observed that, LSCF reacts with YSZ forming to a non-conducting phase between the electrode and the electrolyte [20]. Consequently, a thin layer of Cerium-Gadolinium Oxide (CGO) is generally added as a barrier to limit the formation of this secondary phase [21]. Moreover, the CGO barrier layer alleviates the mismatch in thermal expansion coefficients with YSZ, hence reducing the risk of mechanical damage.

I.3.3. Hydrogen electrode

In the hydrogen electrode, the electrochemical reactions take place at TPBs supplied by hydrogen gas, oxygen ions and electrons. The electrode material is thus chosen to be an ionic and electronic conductor, along with high catalytic activity. The most common composite used for the hydrogen electrode is the cermet of nickel and YSZ [19]. The YSZ is chosen to ensure a good compatibility with the electrolyte usually made of 8YSZ. The two types of zirconia stabilized with 8% and 3% molar of yttria can be used depending on the targeted properties of the hydrogen electrode. The nickel is used as the electronic conductor for its attractive properties and low cost. Indeed, it exhibits very high electronic conductivity and electro-catalytic activity for hydrogen oxidation/reduction. As the hydrogen electrode is usually used

as the cell mechanical support, 3YSZ is preferred, in certain cases, for its better robustness [16]. However, 3YSZ presents lower ionic conductivity than 8YSZ. In this case, a particular attention is paid for the hydrogen electrode microstructure to fulfill both high electrochemical performance and good mechanical properties. Accordingly, the hydrogen electrode is often formed of two layers. A thin functional layer (FL), in contact with the electrolyte, usually made of 8YSZ, to enhance the ionic conductivity and a thicker current collection and gas diffusion layer (CC) in 3YSZ, which corresponds to the mechanical support of the cell.

I.4. SOC advantages

The SOC is an electrochemical device operating at high temperature (600°C-900°C). It offers many advantages. Since the electrochemical reactions, which take place in the two electrodes, are thermally activated, it can reach very high efficiency without the use of expensive electro-catalyst. It presents a good reversibility and a same device can be used in fuel cell and electrolysis mode [22]. In addition, the SOC technology offers fuel/feed flexibility (*i.e.* hydrogen, alkanes, alcohols and ammonia). In particular, it can be employed as a co-electrolyser of a mixture of water steam and carbon dioxide gas producing hydrogen and carbon monoxide.

I.5. SOC degradation mechanisms

During operation in both fuel cell and electrolysis modes, several degradation phenomena can arise leading to the deterioration of the overall cell performances [23,24]. The dominant mechanisms of degradation are found to be dependent on the operating conditions, the cell materials and architecture. They mainly refer to microstructural evolutions in the electrodes, physicochemical destabilization of materials associated with reactivity between the cell components and mechanical damage. In addition, contamination by impurities may occur resulting in the degradation of the global cell performances. Finally, it has been shown that the degradation of the cell performances is in general more accelerated in electrolysis mode, especially during polarization at high current density [25].

I.5.1. Physicochemical destabilization of materials

Electrolyte: Nano-porosities formation and interdiffusion.

The formation of nano-porosities in the YSZ electrolyte close to the interface between the oxygen electrode has been observed in electrolysis mode [26,27]. This results in a decrease in

the ionic conductivity due to the increase in the series resistance [28]. However, the mechanism of the formation of these nano-porosities is not yet fully understood. Furthermore, it is to be noted that the diffusion of element such as the Gadolinium into the electrolyte can also affect its ionic conductivity [29].

Oxygen electrode: LSCF demixing and reactivity at the electrode/electrolyte interface.

For LSCF based electrode, a physicochemical destabilization of the material has been observed referring to the release and migration of strontium as well as a reactivity with the electrolyte material [30]. These phenomena induce the creation of non-ionic conducting phases such as strontium zirconates at the electrode-electrolyte interface and strontium oxide film at the LSCF surface, thus partly explaining the cell performance degradation. It has been shown that a barrier layer between the electrode and the electrolyte cannot completely prevent the formation of the strontium zirconates in all cases [27]. It is to be noted that the electrolysis mode aggravates the degradation due to these phenomena [27,31].

I.5.2. Microstructural evolution

Hydrogen electrode: Ni *agglomeration and migration.*

During operation, a morphological evolution of the microstructure can arise in the hydrogen electrode. Indeed, Ni migration towards the interface between the hydrogen electrode and the electrolyte can occur in SOFC mode while the reverse process can appear in SOEC mode. Therefore, the Ni migration results in a change of the distribution of the Ni phase within the hydrogen electrode. It has been shown that this phenomenon is mainly activated in electrolysis mode [32,33]. In this case, when Ni particles migrate away from the hydrogen electrode-electrolyte interface, the TPB density of the functional layer decreases in the long term, thus lowering the global cell performances.

Another phenomenon associated to the microstructural evolution is the Ni phase agglomeration [33,34]. It is described by coarsening of the Ni phase driven by internal energy minimization, leading in particular to the sintering of small Ni particles at the high operating temperature. This results in a decrease of the density of the active TPBs available for electrochemical reactions, leading to the deterioration of the overall cell performances. For instance, Hubert et al. [34] have found that performance losses of 30% and 25% after the first 2000 h of a cell operated at 850°C in SOFC and SOEC modes, respectively could be ascribed to the Ni agglomeration phenomenon. According to the different works reported in literature, this phenomenon appears to be independent of the cell operating mode [31]. Furthermore, it has been shown that this

phenomenon occurs mainly during the early stage of the cell operation before stabilizing for long operating time. In the Ni-YSZ cermet, the presence of the YSZ skeleton enables mitigating further the Ni coarsening and hindering the massive Ni agglomeration [34].

Finally, the Ni agglomeration and migration phenomena are found to be the cause of a significant part of the degradation of the global performance of the cell.

I.5.3. Mechanical damage

Different forms of mechanical damage can occur in the cell: (i) delamination at the interface with the electrolyte and/or micro-cracking of the oxygen electrode, (ii) fracture of the electrolyte, (iii) delamination at the interface between the functional layer and the current collector layer, (iv) micro-cracking of the YSZ skeleton of the hydrogen electrode. All these mechanical degradations of the cell may have various and often combined origins: external mechanical loading, internal stresses induced by the thermal expansion coefficient mismatch between the cell components, Ni re-oxidation, formation of secondary phase and nano-porosities, etc.

I.5.3.1. Oxygen electrode delamination

The delamination of the oxygen electrode is a typical problem strongly dependent on the electrode material, the cell design and the operating conditions. The delamination has been observed for instance in the experiments by Mawdseley et al. [35] for an electrolyte supported cell operated for 2000h at 800°C in electrolysis mode (Fig. I-4a). In this particular case, the delamination was probably due to the use of a composite electrode made of a mixture of zirconia and perovskite material [31]. With the classical LSCF material and associated barrier layer, this type of degradation is less often observed. Nevertheless, the delamination can still arise in some specific cases. As an illustration, for the hydrogen electrode supported cell, the TEC mismatch between the cell components leads to substantial internal stresses at room temperature. Therefore, during the cooling down, the significant elastic energy stored in the electrolyte can constitute the driving force for the delamination of the oxygen electrode [36]. For example, for this cell configuration, the increase in polarization resistances after operation was mainly attributed to the oxygen electrode delamination. It has been shown also that the formation of a secondary phase at the interface between the electrolyte and the oxygen electrode is liable to create micro-cracks leading to the delamination of the oxygen electrode [37]. It is to be noted that this phenomenon was found to be aggravated in electrolysis mode. This can be explained

by the production of oxygen at the electrolyte-electrode interface making this region subjected to high pressures [38,39] . Indeed, Laguna-Bercero et al. [39] have observed that micro-cracks appear from pores or voids created during cell operation, where oxygen tends to accumulate (Fig. I-4b). The detachment of the oxygen electrode is a serious issue even in the case of a partial delamination resulting in localized gaps between the electrode and the electrolyte. By reducing the surface in contact with the electrolyte available for electrochemical reactions, the delamination leads to a significant decrease in the cell performance.

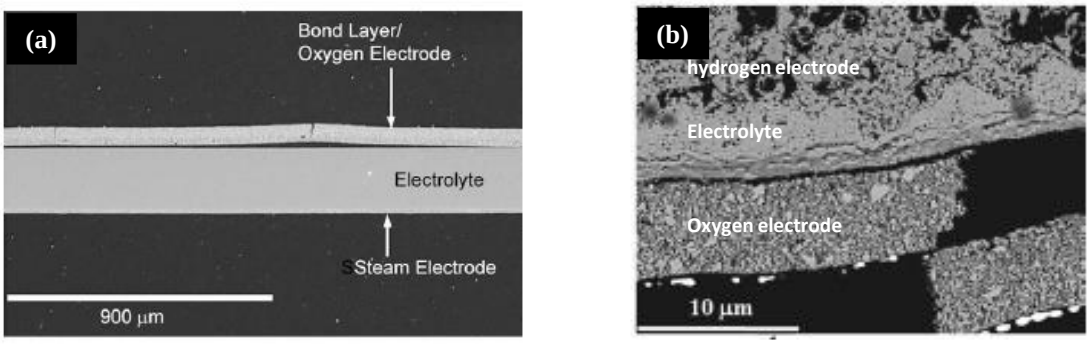

Fig I- 4. Oxygen electrode delamination in an: a) electrolyte-supported cell [35], b) hydrogen electrode-supported cell [39].

I.5.3.2. Cell layers fracture

Mechanical damage due to the TEC mismatch between the SRU components.

As previously mentioned, the TEC mismatch between the different cell layers generates large internal stresses when cooling the cell from the manufacturing temperature [36]. For the hydrogen electrode supported cell configuration, it has been shown that the electrolyte at room temperature is subjected to residual compressive stresses, which are found to increase with thermal cycling [40]. It is difficult to create cracks in a dense electrolyte under compressive stress state since the compressive fracture strength is very high, exceeding 2 GPa [41]. Therefore, as a general matter, these residual compressive stresses have a protective role for the electrolyte against fracture. These protective stresses are reduced when heating the cell at the operating temperature. Nevertheless, even in this case, the electrolyte rupture remains unexpected.

Contrary to the electrolyte, the two porous electrodes can be cracked both in compression and in tension. For example, in the case of the electrolyte-supported cell, the hydrogen electrode is submitted to non-negligible tensile stress at room temperature due to manufacturing that can induce channel cracking of this thin electrode [36,42,43]. Moreover, in both configurations (*i.e.*

hydrogen electrode supported cell or electrolyte supported cell), the thermal gradients arising in operation along with thermal cycling can also trigger the degradation of the electrodes [44–46]. In this case, the stack design including the interconnect plates play a key role on the cell internal stresses as discussed in [7,46,47]. Depending on the SRU geometry and especially on the interconnect thickness, mechanical damage can be induced in the electrodes [46].

It is worth noting that reliable predictions of the electrode total fracture can be obtained by a statistical approach such as the Weibull probability when the layer is submitted to a tensile stress [36]. It has been shown that the deterministic approach also provides for thin layers consistent results with the Weibull theory. For instance, Laurencin et al. [48] have applied an energetic method to predict the total fracture of the thin electrolyte. The comparison with the results given by the Weibull approach has shown a good agreement between the statistical and the deterministic methods. When the layer is subjected to a compressive loading, a stress criterion can be used to estimate the fracture. These predictions are useful to determine the threshold for which the total fracture in the porous electrodes is triggered. However, they cannot inform about the internal damage in the electrodes (Fig. I-5) that affects the cell performances. For this purpose, the crack nucleation and distribution should be estimated in the complex 3D microstructure of the porous electrode. However, as discussed in details later in section I.7, fully validated methods to model such damage in real porous ceramics are not yet available.

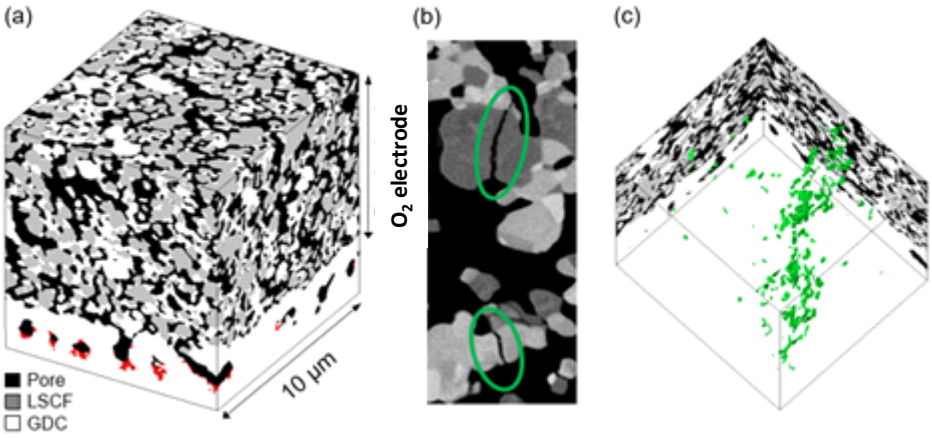

Fig I- 5. (a) LSCF-based O_2 electrode imaged by FIB-SEM serial sectioning after segmentation. (b) Close-up view in the EsB grayscal data showing cracks. (c) 3-D view of the cracks detected in the imaged sample volume [49].

Internal stresses in composite electrodes.

When considering composite electrodes, the difference in the TEC between the two materials can generate local internal stresses (at short distance) in the network of the two solid phases [44,45]. For the porous cermet, in particular, the TEC mismatch between Ni (16.9×10^{-6} K^{-1}

[50]) and YSZ (10.8×10^{-6} K^{-1} [51]) is liable to generate locally high tensile stresses within the YSZ skeleton. The internal stresses within the cermet is also very sensitive to the Ni re-oxidation.

I.5.3.3. Brief overview of the cell mechanical damage during redox cycling

In the case of a fuel shortage or re-introduction of oxygen because of sealing deficiencies during system shutdown or operation, the Ni of the hydrogen electrode is liable to re-oxidize. The swelling of the Ni phase induced by its re-oxidation results in a significant expansion of the cermet volume. Therefore, for the hydrogen electrode-supported cell, high tensile stresses can be generated in the thin electrolyte despite the residual compressive stresses, thus leading to the creation of cracks. For example, in the experiments of Malzbender et al. [52] and Laurencin et al. [48], an array of cracks was observed in the electrolyte after re-oxidation in air meaning that tensile stresses above the fracture strength were reached (Fig. I-6a-b). It is worth noting that the fracture mode of the dense electrolyte is brittle with the creation of large cracks crossing its thickness. The gas leakage through the cracks then accelerates the Ni re-oxidation resulting in a rapid drop of the performance and complete failure of the cell in a very short time. Accordingly, the fracture of the electrolyte is considered as the most detrimental issue for the cell.

Besides, it has been observed during experiments under milder Ni re-oxidations conditions that, the volume expansion of Ni upon redox cycling induces first the micro-cracking of the YSZ skeleton of the hydrogen electrode. For instance, Faes et al. [53] have detected the formation of micro-cracks after one redox cycle conducted in air at a temperature of 1000°C (Fig. I-6c). Using X-ray nanotomography, Nakajo et al. [54] have tracked the microstructure evolution after re-oxidation in air at 800°C of a small volume of cermet and have quantified the density of micro-cracks created in the YSZ skeleton (Fig. I-6d). Furthermore, it has been estimated that YSZ micro-cracking likely results in the degradation of the global performances of the cell due to the damage of the ionic conducting phase. Indeed, the formation of few micro-cracks is found to lead to a significant loss in the cell power density [40].

Finally, in the particular case of fuel shortage (*i.e.* electrochemical re-oxidation by an ionic current), it has been noticed that the thin layer at the interface between the electrolyte and the hydrogen electrode is the most exposed region upon redox cycling. Therefore, a delamination of the functional layer at the interface with the current collector layer as well as at the interface with the electrolyte can arise resulting in the deterioration of the overall cell performances [48].

Indeed, Laurencin et al. [48] have observed this mechanical degradation after nine redox cycles by an ionic current at 800°C (Fig. I-6e).

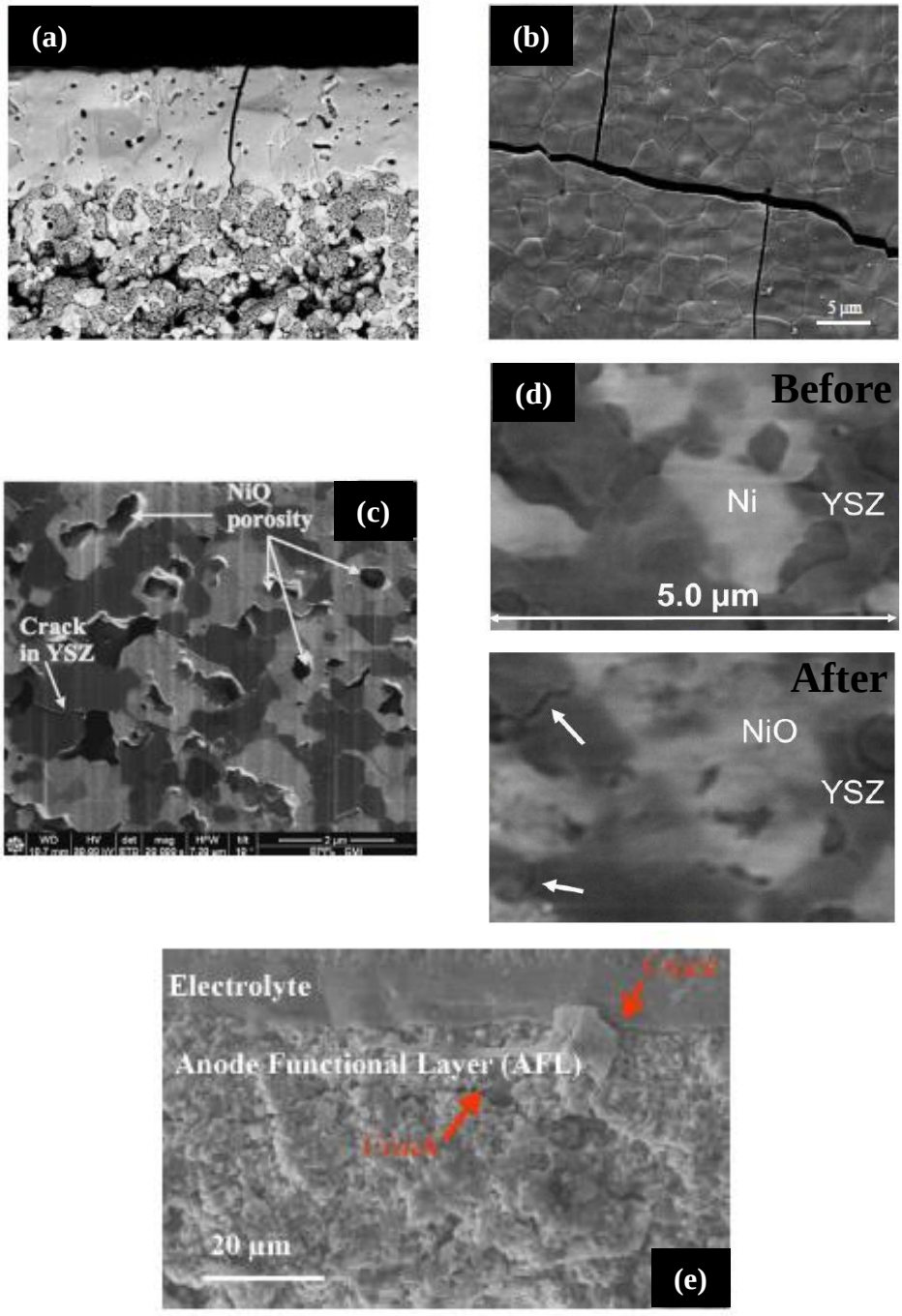

Fig I- 6. Different forms of mechanical degradation induced by Ni re-oxidation: a) electrolyte fracture observed on a scanning-electron microscopy (SEM) cross-section [52], b) cracks observed at the surface of the electrolyte [52], c) micro-cracks within the YSZ skeleton observed on a focused ion beam-scanning electron microscopy (FIB-SEM) cross section [53], d) microstructure before and after re-oxidation observed in-situ by X-ray nanotomography, showing the formation of micro-cracks within the YSZ skeleton after re-oxidation [54], e) cracks observed at the interface electrolyte-anode functional layer and anode functional layer-current collector layer [48]. For a), b), c) and d), the re-oxidation was conducted in air and by an ionic current for e).

To conclude this section, it appears that Ni re-oxidation is one of the most detrimental issue for the cell as it is liable to induce not only the damage of the cermet but also the fracture of the electrolyte resulting in the complete loss of the cell.

For this reason, a deep understanding of this phenomenon along with methods for predicting micro-cracking in the hydrogen electrode YSZ skeleton up to the complete failure of the electrolyte are required. It is worth noting that the degradation in the cell performances, caused in particular by the formation of micro-cracks in the YSZ skeleton upon redox cycling, can be quantified only when the mechanical damage of the cermet is correctly predicted. Accordingly, in this case, it would be possible to identify solutions to improve the redox tolerance of the cell and increase its lifetime.

I.6. Literature review on Ni re-oxidation

Fuel starvation due to accidental interruption in the fuel supply, or oxygen introduction due to sealing failures and/or system shutdown the system shutdown, can lead to the Ni re-oxidation in the hydrogen electrode [40,55]. Depending on the type of system deficiency events or imperfections, the Ni can either oxidize directly in air (*e.g.* oxygen leakage) or electrochemically with the ionic current O^{2-} (*e.g.* fuel shortage or high current demand).

The first line of proposed measures to limit the risk of Ni re-oxidation mainly concerns the fuel supply system ancillaries. For instance, the implementation of an auxiliary system has been suggested to enable a sufficient supply of fuel to maintain reducing conditions in the case of leakage or accidental interruption until falling down below a secure temperature during the system emergency shutdown [40,55]. As a general matter, it is worth noting that these mitigating strategies can prevent the complete stack failure due to the electrolyte fracture but they cannot prevent a partial re-oxidation inducing a decrease in the performances.

In this section, the phenomenon of Ni re-oxidation is described and the main experimental and numerical results reported in the literature are presented.

I.6.1.Ni re-oxidation of the Ni-YSZ substrate

I.6.1.1. Homogeneity of the Ni oxidation in the cermet

At the electrode scale, the Ni oxidation can be treated as either homogeneous or not in the cermet. In the case of fuel starvation, it is always non-uniform and arises first at the interface with the electrolyte because the Ni is electrochemically oxidized. When the re-oxidation occurs because of the presence of O_2 in the electrode gas compartment, the homogeneity of the re-

oxidation rate throughout the thickness of the electrode is dependent on the kinetics, hence the temperature. The oxidation rate can be approximated as homogeneous, at low temperature (700-750°C), providing higher mechanical stability of the cell whereas the oxidation is inhomogeneous at high temperature (>700-750°C). This inhomogeneous oxidation is found to have more detrimental effect on the cell than the homogeneous one [40,48,55].

I.6.1.2. Cermet deformation as a function of the degree of oxidation

As a general matter, the re-oxidation of the Ni phase results in its expansion and is characterized by faster kinetics at high operating temperature [55]. The maximum volume expansion of Ni during oxidation is theoretically estimated to about 71.2% while its contraction is around 41.6% upon reduction [53].

A degree of oxidation (DoO) is attributed to each Ni volume expansion and it reaches 100% when the Ni swelling reaches the maximum (71.2%). It is defined as the ratio between the mass of oxygen absorbed and the maximum mass of oxygen liable to be absorbed when a complete oxidation occurs ($DoO = m_{absorbed\ O_2}/m_{maximum\ O_2}$). The degree of oxidation informs about the effect of external parameters such as temperature, time and oxygen flow and internal parameters such as microstructural properties, cermet composition and dimensions [40].

It has been shown that the Ni swelling induced by its re-oxidation results in a macroscopic deformation of the hydrogen electrode. The cermet redox strain can be measured during redox cycling using different methods. For example, Sarantaridis et al. [56] have measured the redox strain using dilatometry technique as a function of the degree of oxidation (Fig. I-7a). Faes et al. [53] have used scanning electron microscopy (SEM) image analysis based on the measurement of either the electrolyte cracks width or the porosity and found two evolutions describing the increase of the cermet redox strain upon redox cycling (Fig. I-7b).

The cermet redox strain partly remains after reduction and accumulates upon redox cycling [40,55]. For instance, Robert et al. [57] measured a shrinkage of about 0.15% after the initial reduction of the as-sintered cermet. Then, they found that the Ni re-oxidation resulted in a volume expansion of the hydrogen electrode of approximately 0.35%. This cermet swelling was reduced after the subsequent reduction by a contraction of about 0.25%. A permanent strain of around 0.1% was thus left after the first redox cycle. Therefore, the Ni re-oxidation phenomenon is irreversible, resulting in a permanent redox strain of the cermet.

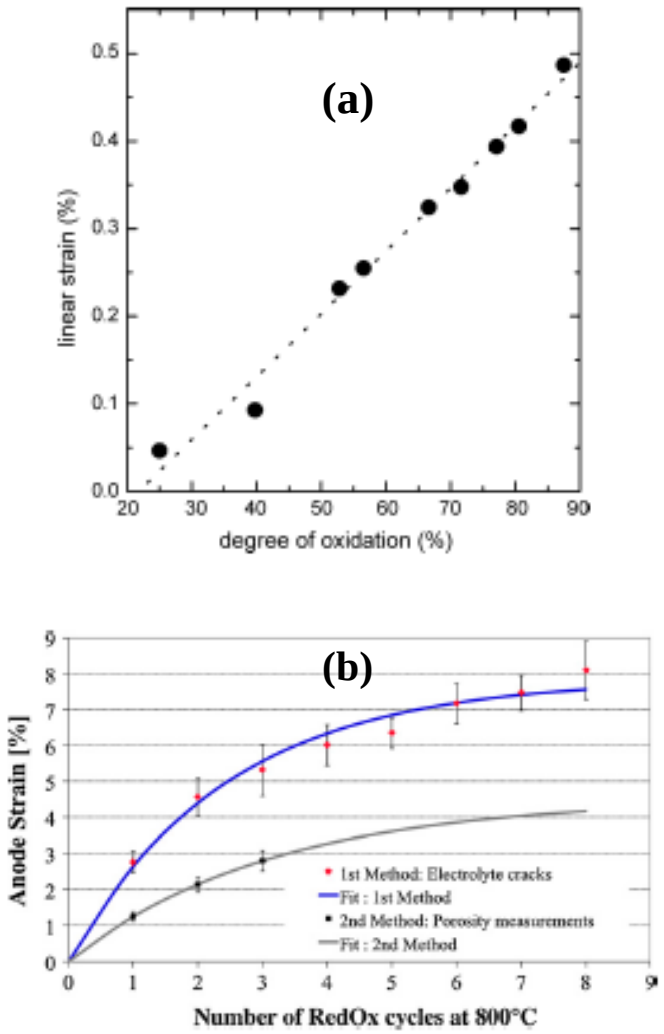

Fig I- 7. Cermet redox strain measured by: a) dilatometry as a function of degree of oxidation [56], b) image analysis as a function of number of redox cycles [53].

I.6.1.3. Parameters influencing the re-oxidation mechanism

The Ni re-oxidation mechanism in the Ni-YSZ cermet is affected by a set of parameters, either external such as temperature and time or internal such as microstructural characteristics. The degree of oxidation is usually used for evaluating the effect of these parameters.

For example, Ettler et al. have found that the kinetics of Ni re-oxidation was faster when increasing the temperature (Fig. I-8). For the same oxidation duration (15 min), the DoO was equal to 74% and 51% at 800°C and 600°C, respectively.

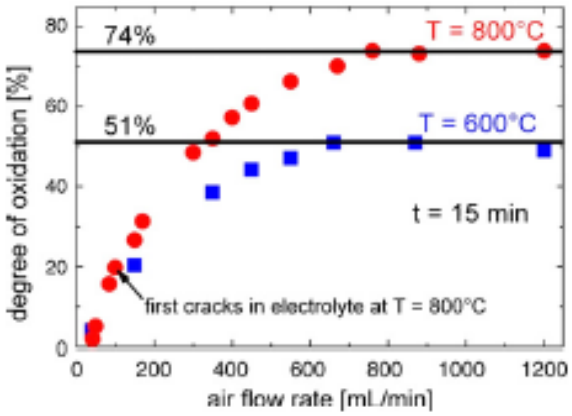

Fig I- 8. Degree of oxidation as a function of air flow rate for two operating temperatures (600°C and 800°C) [40].

The impact of the hydrogen electrode initial microstructure has also been investigated. Malzbender et al. [52] showed that higher porosity is advantageous for redox tolerance even if it enhances the degree of oxidation, as shown in the work of Ettler et al (Fig. I-9) [40]. Moreover, Fouquet et al. [58] have stated that a finer microstructure is beneficial for the redox stability.

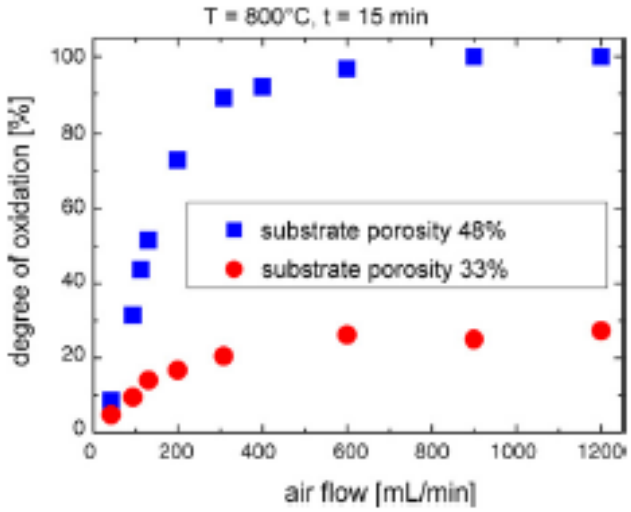

Fig I- 9. Degree of oxidation as a function of air flow rate for two different microstructures with porosities of 48% and 33% at operating temperatures of 800°C for 15 min [40].

Furthermore, Ettler et al. [40] have analyzed the impact of the oxidizing conditions including temperature and duration on the oxidation homogeneity. They have found that below 700°C the oxidation is homogeneous without a gradient of DoO along the cermet. When the temperature exceeds 700°C, they have observed an inhomogeneous oxidation. In this case, the re-oxidation arises first at the outer side. Then, the reduced part of the cermet decreases with the duration to reach a complete oxidized state. According to the work of Laurencin et al. [59], the transition from homogeneous to inhomogeneous oxidation appears in a range of temperature of 700-750°C. In their experiments conducted at 800°C, they have observed the oxidation gradient created at an average DoO of 41.7% and, as expected, they have found that the oxidation was

localized in the outer region of the cermet. They have also measured the NiO/Ni intensity peaks ratio by X-ray diffraction as a function of the location in the hydrogen electrode to further confirm their observations (Fig. I-10).

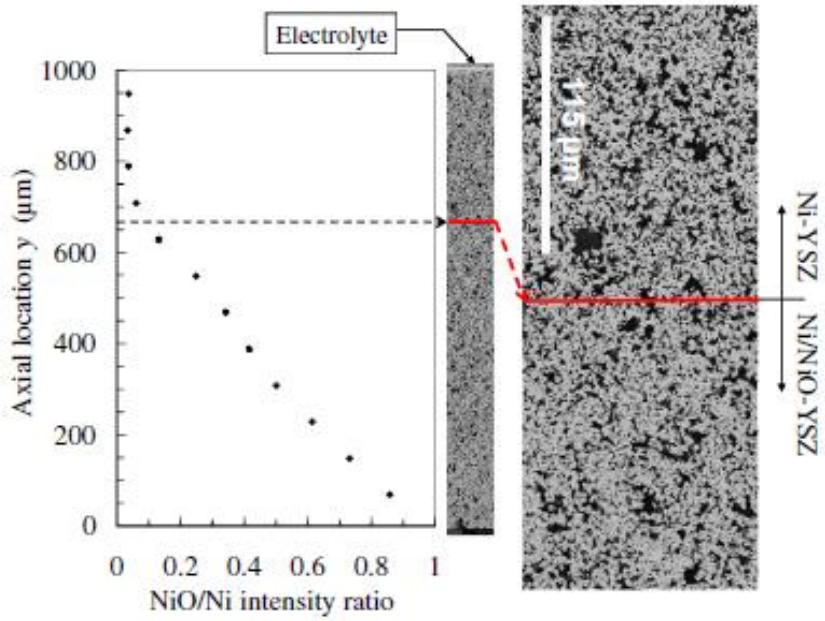

Fig I- 10. Oxidation gradient observed at a DoO of 41.7% in a cermet support oxidized in air at 800°C. The NiO/Ni ratio of the intensity peaks of X-ray diffraction is plotted on the left as a function of the axial location in the cermet. On the right, the SEM micrograph is depicted showing a difference of microstructure including porosity between the oxidized and the reduced states [60].

I.6.2. Impact of Ni-reoxidation on the cell mechanical and electrochemical response

I.6.2.1. Impact on the cell stress state

In order to deeply understand the impact of redox cycling on the mechanical stability of the hydrogen electrode-supported cell, *in situ* measurements of the stress state in the electrolyte have been performed using X-ray powder diffraction. In these experiments, the strain is converted to stress by assuming a plane stress field along with using the X-ray elastic constants of Eigenmann et al. [52,61]. For instance, Faes et al. [55] have measured a compressive residual stress of 400 MPa in the as-sintered electrolyte at room temperature. This is due to the difference in the thermal expansion coefficients (CTE) between the cermet and the electrolyte (*i.e.* the CTE of the NiO-8YSZ and 8YSZ is equal to 12×10^{-6} K^{-1} and 10.5×10^{-6} K^{-1}, respectively [50]). Then, they have found that the compressive residual stress decreases to 250 MPa after the initial reduction of the cermet and subsequently to 170 MPa in the re-oxidized

state. Therefore, they have noticed that the residual stresses decrease with the redox cycles. In the experiments of Ettler et al. [40], the re-oxidation was conducted in air at 800°C and the stresses in the electrolyte were measured at room temperature (Fig. I-11). During redox cycling, the change in the thermal expansion coefficient of the hydrogen electrode results in a decrease of the compressive residual stress in the electrolyte at the reduced state. Indeed, the thermal expansion coefficient of the anode at the reduced state is lower than at the as-sintered state (*i.e.* the CTE of the NiO-8YSZ and Ni-8YSZ is equal to 12×10^{-6} K^{-1} and 11×10^{-6} K^{-1} [50], respectively), thus explaining the loss in the compressive residual stress in the electrolyte measured after the first reduction. Moreover, they have found that the first re-oxidation associated to a low DoO of 5 % leads to an additional compressive residual stress in the electrolyte. This was induced by the non-homogeneity of the oxidation at such high temperature along with the low DoO. Indeed, in this case, the outer side of the cermet oxidizes first resulting in a concave bending strain towards the electrolyte at low DoO. Therefore, compressive stresses are generated in the electrolyte layer. At a DoO of 20%, they have observed a significant decrease of the residual stresses meaning that the electrolyte became subjected to tension.

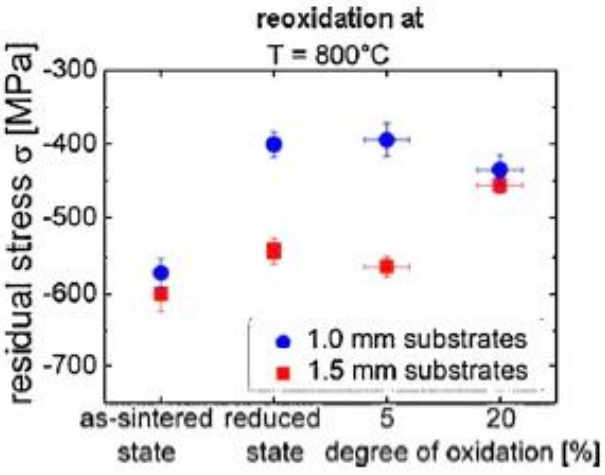

Fig I- 11. Evolution of the residual stress in the electrolyte as a function of degree of oxidation (DoO) for oxidation temperature of 800°C. X-Ray Diffraction measurements were performed at room temperature [40].

Therefore, a change in the residual stress state of the electrolyte occurs at a re-oxidation threshold. In other words, the residual compressive stresses in the electrolyte at the oxidized state decreases when the oxidized region exceeds the neutral axis of the cermet. In this case, the cermet becomes subjected to a convex bending strain. Upon increase of the DoO, the compressive residual stress in the electrolyte is progressively relieved until turning into tensile

stress. The latter is the only cause of the electrolyte fracture in SOC whereas compressive stress always has a protective role.

I.6.2.2. Cell mechanical damage

Electrolyte fracture.

During redox cycling, the cermet redox strain accumulates up to a threshold liable, in the case of the hydrogen electrode-supported cell, to generate high tensile stresses in the thin electrolyte leading to its fracture. In the case of re-oxidation in air at 800°C, Laurencin et al. [55] have found that a redox strain of approximately 0.26-0.34 associated to a critical DoO of about 58-71% leads to the fracture of the electrolyte and the complete failure of the cell. This result was in good agreement with the experiments conducted at the same temperature by Sarantaridis et al. [56] where the critical DoO was found in the range of 49-75%. In the case of electrochemical oxidation by the ionic current O^{2-} at 850 °C, Sarantaridis et al. [56] have found that the critical DoO inducing the fracture of the thin electrolyte is equal to 5%. The value is much lower in this case compared to the one measured during oxidation conducted in air. Indeed, the electrochemical oxidation is non-homogeneous and occurs first at the interface with the electrolyte. They concluded that inhomogeneous oxidation by an ionic current presents the most detrimental effect and leads to the fracture of the electrolyte at low DoO, thus limiting in absolute terms the redox tolerance of the cell.

Micro-cracking in the cermet.

Aside from the electrolyte fracture, it has been found that Ni re-oxidation induces as anticipated the micro-cracking of the YSZ skeleton in the hydrogen electrode during the early stages of oxidation (*cf.* section I.5.3.3). For example, micro-cracks have been observed by Faes et al. [53] after one redox cycle on a Focused Ion Beam - Scanning Electron Microscope (FIB-SEM) cross-section of a cermet support oxidized in air at 1000°C (*cf.* Fig. I-6c). Nakajo et al. [54] have used non-destructive 3D imaging by X-ray nanotomography to image the same sample of cermet substrates before and after re-oxidation in air at 800 °C. The analysis of the 3D reconstructions of the samples oxidized for 45 min informed about the location of cracks and change of the microstructure upon oxidation as well as quantifying the density of the micro-cracks created within the YSZ skeleton (*cf.* Fig. I-6d).

I.6.2.3. Impact on the cell performances

At the early stages of re-oxidation in air, it has been noticed that the Ni volume expansion is liable to create micro-cracks within the YSZ skeleton of the hydrogen electrode before the fracture of the electrolyte and the complete failure of the cell at high DoO (49-75%). This contributes to the degradation of the overall cell performances which could be observed from the first redox cycles [40,53]. Besides, it is worth noting that changes in the cermet microstructure including the creation of closed porosities and the redistribution of the Ni phase also arise upon redox cycling, which can affect in particular the density of connected TPBs in the cermet. Therefore, these microstructural evolutions also participate to the degradation of the cell electrochemical performances [53,55,62]. As an example, Ettler et al. [40] have studied the impact of the oxidizing conditions (temperature and duration) on the response of the cell in terms of the open current voltage (OCV) and the power density (Fig. I-12a-b).

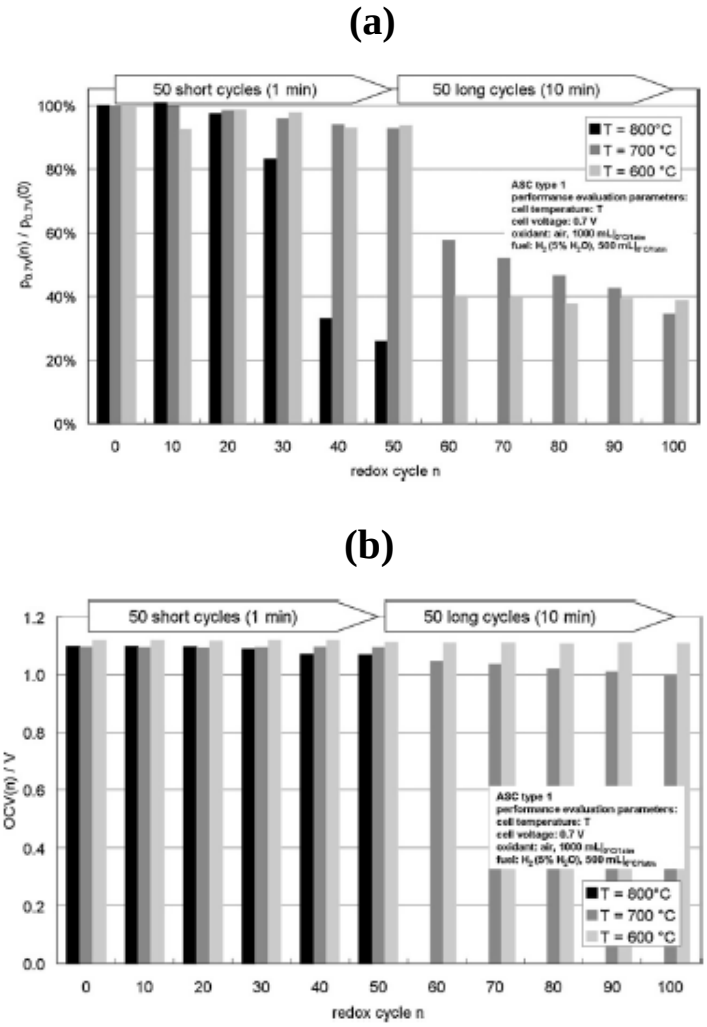

Fig I- 12. Evolution of electrochemical performances of anode-supported cell upon redox cycling for three temperatures (800°C, 700°C and 600°C): a) normalized power density, b) open current voltage [40].

They have found that the degradation of the cell performances decreases when decreasing the operating and oxidation temperature. Besides, they noticed that a small decrease in the OCV results in a significant decrease in power density (at 800°C: cycles 30-50 and at 700°C: cycles 60-100). The loss in power density was explained by the formation of micro-cracks in the cermet support. In addition, they showed that a long re-oxidation duration of 10 min causes a rapid drop in power density at 700°C and 600°C, and a complete loss of the cell at 800°C due to the creation of cracks in the electrolyte.

I.6.3. Numerical works on the mechanical damage of the cell upon redox cycling

I.6.3.1. Electrolyte fracture predictions

The experiments of oxidation in air have shown that cracks can occur in the cermet at an early stage of Ni re-oxidation while the fracture of the electrolyte occurs at a significantly larger DoO. Macro-scale modeling has been adopted to study the fracture of the electrolyte and the Weibull approach has been selected for its capability to predict the failure of dense ceramics under tensile stresses. In this statistical method, the failure probability P_f is by definition expressed as a function of the volume tested V_{test}, the tensile stress σ, and the Weibull parameters (V_0, σ_0 and m):

$$P_f = 1 - e^{\left(-\int_{V_{\text{test}}} \left(\frac{\sigma}{\sigma_0}\right)^m \frac{dV_{\text{test}}}{V_0}\right)} \quad \text{(I-4)}$$

It is to be noted that σ_0 is the Weibull strength associated to the failure probability P_f of 0.632. Faes et al. [53] have applied Weibull approach by considering the parameters (V_0, σ_0 and m) of 8YSZ material and calculated a critical redox strain of 0.18 at 800°C. In the work of Laurencin et al. [48], the fracture of the 8YSZ electrolyte at 800°C was also found to occur at a range of 0.16-0.19% for the cermet expansion associated to a degree of oxidation of 50%. The numerical predictions using the Weibull approach agreed with the experimental estimations of the critical cermet strain which was in the range of 0.26-0.34.

Laurencin et al. [60] have also studied the oxidation kinetics and assessed the impact of the temperature and the homogeneity of oxidation using the Weibull approach. The probability of the electrolyte failure was calculated at three temperatures (600°C, 700°C and 800°C) by considering the creation of a redox gradient in the cermet at high temperature (800°C). The

experimental results were retrieved and the critical degree of oxidation was accurately predicted (*i.e.* DoO = 64-66%).

I.6.3.2. Electrode damage during re-oxidation

The redox tolerance of the hydrogen electrode remains a salient subject of investigation. Few studies have addressed this problem using macro-scale modeling. For example, Pihlatie et al. [63] have considered an homogeneous medium for the cermet and have proposed a model that takes into account different non-elastic strains including the one coming from the YSZ micro-cracking. Their model proved capable to reproduce qualitatively the increase of the cermet permanent strain upon redox cycling.

This limitation of the macro-scale approach has underlined the necessity to model the cermet microstructure in order to accurately describe the impact of the local morphology on the fracture of the YSZ skeleton upon redox cycling. To date, few works at the micro-scale are available in the literature. For instance, Toros et al. [64] have developed a mathematical model to simulate the Ni re-oxidation considering 3D synthetic microstructures representative of the cermet. They have analyzed the impact of the temperature and the duration of oxidation on the distribution of the stresses. As expected, they have found that some regions of the YSZ skeleton were subjected to high tensile stresses liable to create micro-cracks. However, they did not go further in their analysis to predict the fracture of the YSZ skeleton induced by the Ni re-oxidation. Xiang et al. [65] have recently studied the fracture of the YSZ skeleton of the hydrogen electrode considering 3D real microstructures. They have analyzed the stress distribution in the YSZ phase generated under compressive and tensile loading as a function of the microstructural properties. The failure probability of the YSZ backbone was then calculated using the Weibull approach. Abdeljawad et al. [66] have developed a model to simulate the fracture of the YSZ skeleton induced by the Ni re-oxidation. 3D real microstructures obtained by X-ray tomography have been considered and a local fracture criterion has been implemented. This criterion states that cracks initiate when the local tensile stress exceeds the YSZ strength. Thanks to their model, the spatial distribution of the created micro-cracks in the microstructure has been simulated and analyzed, along with calculations of the cermet redox strain. However, the relevance of the local fracture criterion, which was not based on experimental validation or theoretical demonstration, can be questionable for the damage prediction in porous electrodes. Indeed, the energy criterion for the crack nucleation is expected to play a key role on the local fracture for porous ceramics. Accordingly, it appears that the model proposed by Abdeljawad

et al. [66] to simulate the fracture of the YSZ skeleton induced by the Ni re-oxidation need to be improved to advance further the understanding of electrode damage upon re-oxidation.

This bibliography review on the SOC electrode damage shows that the modeling of crack nucleation and propagation is essential and must rely on an accurate description of the fracture mechanisms in porous ceramics, which still needs to be better understood and validated.

I.7. Fracture in porous ceramics

The fracture of porous ceramics is complex and strongly dependent on the microstructure. Indeed, it has been shown that the crack onset and propagation is a function of the local geometry mainly referred to the shape, size and pore distribution in the microstructure [67–69]. Therefore, the apparent toughness and strength of porous ceramics can strongly differ from the properties of the dense material.

I.7.1. Apparent fracture toughness and strength

It has been widely reported that the strength of porous ceramic is strongly decreased with increasing the porosity. For instance, it has been shown that the strength of alumina and zirconia follows an exponential decrease with the pore volume fraction [69–71]. Miyazaki et al. [69] have studied the impact of the pore volume fraction on strength for a porous alumina by three-point bending test. As presented in (Fig. I-13a), the bending strength was found to decrease from 69 MPa to 16.1 MPa when increasing the porosity from 35 % to 58 %. Ryshkewitch et al. [70] have conducted compression tests on porous alumina and zirconia and have also found that the compressive fracture strength decreases with porosity. In the case of uniaxial compression loading, the fracture mode of porous ceramics was found to change from a brittle behavior at low porosity towards a diffuse damage at high porosity [72,73]. This transition observed in experiments is still not well understood and the underlying mechanisms have not been yet precisely explained.

Moreover, it is generally observed that the apparent toughness of porous ceramics also decreases with increasing porosity [71,74,75]. For instance, Samborski et al. [74] have measured the fracture toughness of porous alumina under three-point bending test. For a porosity ranging from 3.5 % to 20.8 %, they have obtained a decrease in the fracture toughness from 3.3 MPa $m^{1/2}$ to 2.6 MPa $m^{1/2}$. Using double torsion testing, Khajavi et al. [75] have measured the fracture toughness for YSZ as a function of porosity. They have found that the

fracture toughness decreases from 4.27 MPa $m^{1/2}$ to 0.71 MPa $m^{1/2}$ when increasing the porosity from 4.5 % to 45.5 % (Fig. I-13b).

However, it is worth noting that opposite trends in the experimental results have been also reported in the literature [76]. Indeed, in specific conditions of well distributed macropores and low porosity, several studies have found that the material resistance can be reinforced by the porosity. In other words, the apparent toughness of the porous material exceeds the one of the dense ceramic. For instance, Deng et al. [76] have tested porous SiC specimens with two types of pore morphologies under three-point bending loading. They have found that the apparent fracture toughness is enhanced when increasing the pore size. This unexpected behavior could be explained by the effect of both a crack tip blunted by macro-pores and a large distance between the pores [67,76]. Therefore, there is a competition between a weakening effect by increasing the pore volume fraction and a strengthening effect associated to the local crack blunting due to the voids.

The dependency of both the apparent fracture toughness and strength of porous ceramic is thus strongly affected by the local morphology within the microstructure.

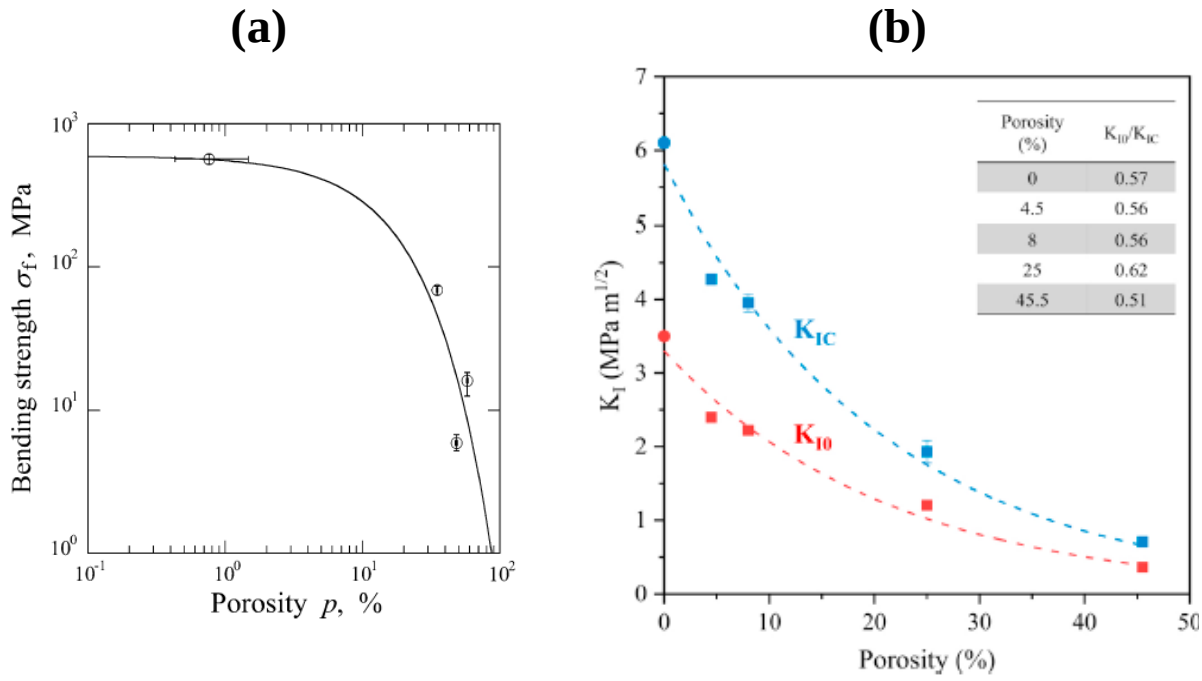

Fig I- 13. Decrease of the measured a) bending strength of porous alumina [69], b) fracture toughness of the yttria stabilized zirconia with the porosity [75].

I.7.2.Models for porous ceramics

Modeling appears as a relevant approach to establish the complex correlations between the fracture properties and the microstructures of porous ceramics. For this purpose, the developed models need to be applied on real or synthetic microstructures in 2D or 3D. To the best of our knowledge, there are still no studies demonstrating together numerical simulations considering 3D reconstructions obtained by tomographic techniques as computational domains and dedicated experimental validation. On the contrary, several models have been developed on ideal 2D geometries [67,69,77–82]. Nevertheless, despite their interest and contribution to the current understanding, their relevance to analyze the full complexity of microstructures remains questionable.

An adequate criterion for local fracture is the first fundamental requirement to simulate fracture is porous ceramics. In this frame, depending on the local configuration where the crack nucleates, the fracture can occur under regimes governed by an energy, a stress or a coupled energy-stress criterion. The formulation of the energy criterion is based on the Griffith theory [83,84] and states that the fracture occurs when the change in the potential energy is equal the energy required to create the crack surface. For the stress criterion, the fracture is triggered when the local tensile stress exceeds the material strength. The coupled criterion stipulates that both stress and energy criteria must be fulfilled to induce the fracture. For example, D. Leguillon [85] has developed a rigorous framework for a coupled stress-energy criterion to predict the crack nucleation.

To address the effects of 3D microstructural characteristics on the fracture properties, some authors have proposed to use 3D synthetic microstructures generated using numerical methods [86–93]. The two main approaches that have been employed are the particle-based models (*e.g.* random sphere packing algorithm, discrete element method, lattice element models etc.) and the geostatistical-based models (*e.g.* truncated Gaussian random filed method, Boolean sets method, etc.) [90,94–96]. Accordingly, the characteristics of the microstructures can be precisely controlled allowing to investigate the effect of each microstructural property (*i.e.* phase distribution nature: random or periodic, size and shape) on the fracture behavior. Nevertheless, the representativeness of the synthetic microstructure with respect to the real ones is essential to obtain accurate prediction of the fracture properties. It has been shown that the adapted methods based on the truncated Gaussian random filed method and the sphere-packing algorithms can provide a very good approximation of the real SOC electrode microstructure [12].

2D models for fracture predictions.

Many models have been already proposed on 2D microstructures, considering the energy or stress criterion. For example, Doltsinis and Dattke [77] have used a numerical model to randomly generate the solid phase enabling to obtain several types of microstructures. In their work, the effect of the microstructural properties on the material strength has been evaluated based on an energy criterion. It has been shown that the material strength is increased with decreasing the particle size and the pore volume fraction. However, the discussion was only based on numerical results without any comparison with experimental data. On the other hand, Lipperman et al. [79] have proposed a model, based on a stress criterion, to predict the fracture mechanism of a porous ceramic weakened by a set of cracks of different orientations. They have studied cellular materials and assessed the impact of the form of the unit cell (triangular, square, etc.) on the fracture toughness. Leguillon at al. [67] have applied a local coupled stress-energy criterion on a 2D simplified system of pores. The authors have formulated from this analysis an expression of the macroscopic apparent toughness able to capture the effect of pore and ligament sizes (leading to an apparent strengthening for large pores and low fractions of voids). Therefore, the fracture seems to be controlled by both strength and energy criteria. Nevertheless, the full validation of this claim still needs to be checked on more representative 2D and 3D microstructures.

3D models for fracture predictions.

Compared to 2D-based approaches, only few studies have been devoted to investigate the fracture behavior on 3D synthetic microstructures. It can be noted that most of the models have been developed on microstructures generated by the Discrete Element Method (DEM) [88,90,91,97]. In the work of Jauffres et al. [88], pre-cracked samples have been simulated and the fracture toughness has been calculated as a function of porosity. Their model was able to retrieve the decrease of the toughness when increasing the porosity. However, a discrepancy between the simulated toughness and the experimental data was obtained. Besides, several numerical works have been devoted to predict the fracture strength of porous ceramics [90,91,97]. Among these studies, some have used the energy criterion to predict the fracture as a function of porosity [90]. In this case, the bonds between two particles is supposed to break if the energy reaches the surface energy required to create the crack. It is generally reported that this approach allows reproducing the global evolution of the strength with the porosity observed in experimental measurements. For instance, Liu et al. [90] have obtained that the simulated tensile and compressive strengths decrease when increasing the porosity. Nevertheless, Smolin

et al. [91], who has also used the DEM method, have assumed that the crack initiation occurs when the local stress reaches the material strength. Despite the change in the choice of the fracture criterion, they were also able to retrieve qualitatively the experimental data. More precisely, the change in fracture strength at the percolation threshold was well captured by their model. Therefore, for all these studies, the models seem to capture the dependency of the fracture strength on the porosity whatever the fracture criterion. Nevertheless, it is worth noting that they fails to predict precisely the measurements. For instance, in the work of Roussel et al. [97], the simulated strength was overestimated compared to the experimental data (Fig. I-14a). Finally, the so-called lattice element models have been also applied to study the fracture in porous ceramics. They have been implemented considering a stress fracture criterion [86,87,98] For example, Šavija et al. [87] have found that their model is able to predict the decrease of the flexural strength with increasing the porosity. However, as presented in Fig. I-14b, the discrepancy between the computed results and the measurements was significant.

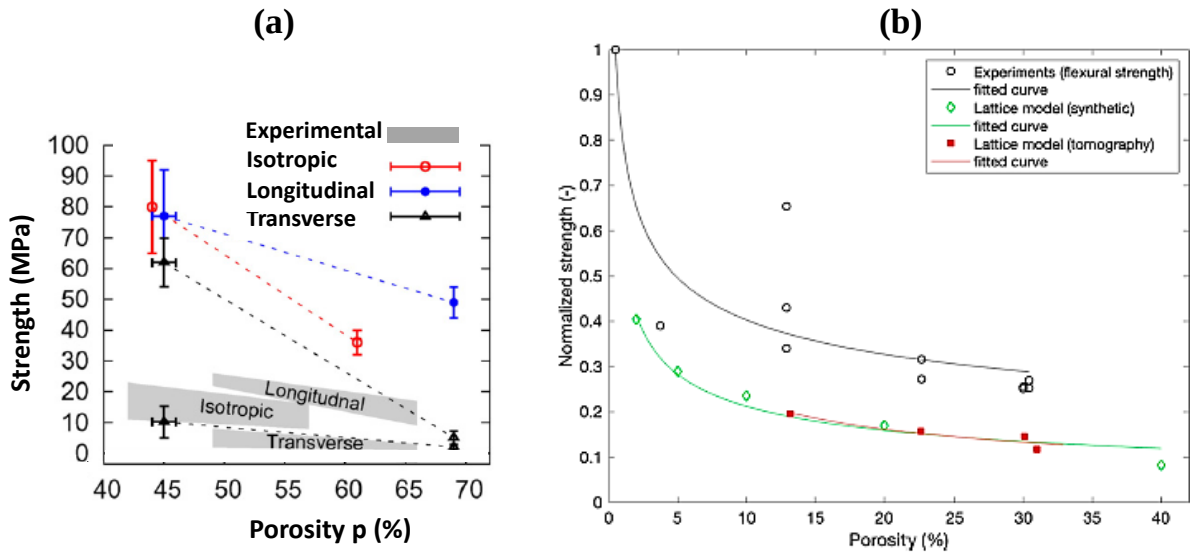

Fig I- 14. Comparison of the computed a) tensile strength, b) normalized flexural strength with the experimental data. Simulations using a fracture stress criterion on microstructures generated by a) discrete element method (DEM) [97], b) lattice element model [87].

I.7.3.Concluding remarks

This short bibliography review shows that key challenges remain for the understanding of the fracture mechanisms of porous ceramics. Indeed, it is still not clearly established under which conditions the local fracture in the porous microstructure may be mainly controlled by an energy

or stress criterion. As discussed in the work of Leguillon et al. [67], it can be suspected that a coupled stress-energy criterion would be required. Moreover, the precise role on the fracture properties of the local morphology in real and complex microstructure is still unclear, but is required for the development of generalized predictive modeling frameworks. Indeed, one of the main difficulty consists in the development of appropriate models for real 3D microstructures that could consider an energy-stress criterion. From a practical point of view, the complexity of real porous ceramic microstructures makes the numerical treatment as well as the introduction of cracks in the 3D meshed volume very challenging. For all these reasons, the simulation of the nucleation and propagation of cracks in porous ceramic microstructure remains a salient subject of investigation.

I.8. Conclusions

The solid oxide cell technology appears promising in the context of transition toward an eco-friendly energy system. However, its durability remains insufficient for industrial deployment. The state-of-the-art of SOC technology has shown that many degradation mechanisms can occur in the cell leading to a deterioration of its performances and reduction of its lifetime. In particular, the mechanical damage in the electrodes is one of the main issues limiting the cell durability. For instance, the Ni re-oxidation is found to be one of the most detrimental phenomena. Indeed, micro-cracks, which arise in the YSZ skeleton of the hydrogen electrode at the early stages of re-oxidation, can significantly affect the overall cell performances. Regarding the fracture of the electrolyte, the studies available in the literature are relevant and provide predictions in good agreement with experiments. However, such situations are extreme from a practical SOC technology standpoint, since they typically correspond to the end of life of the device. In contrast, the current capabilities for the prediction of micro-cracking of the YSZ skeleton during redox cycling remains extremely limited and a deeper understanding is still needed.

Indeed, the facture in porous ceramic is still not fully understood, largely due to the complexity of the microstructure. A reliable modeling of the crack onset, propagation and branching in real porous ceramics still needs to be developed for real microstructure taking into account a relevant mixed energy-stress criterion.

I.9. Objective and methodology of the thesis

Objective of the thesis.

The present work aims to develop a relevant and validated numerical tool able to predict accurately the fracture mechanisms in porous ceramics. The capability to study the electrode damage for SOC applications will be illustrated on the fracture of the YSZ skeleton induced by Ni re-oxidation. For this purpose, a coupled experimental-modeling methodology has been implemented.

Methodology of the thesis.

The methodology adopted in this work is organized into three main steps as shown in Fig. I-15. Firstly, because of the lack of data on porous YSZ in the literature at the micro-scale, dedicated experiments on the mechanical characterization of this material have been carried out and a thorough analysis of the fracture properties and the failure modes has been performed. All the experimental results are presented and analyzed in the second chapter. Secondly, an appropriate numerical tool to study the nucleation and propagation of micro-cracks in real porous ceramic microstructures has been developed. The theoretical description as well as the numerical implementation of the adopted approach are detailed in the third chapter. The capability of the model to accurately predict the crack nucleation and propagation is also discussed. Thirdly, a multi-scale approach has been implemented to evaluate the capacity of the model to retrieve the experimental results and to further understand the underlying mechanism controlling the fracture in porous ceramics. This part of the study is detailed in the fourth chapter, which concludes the validation of the methodology and analysis of the mechanism of fracture in porous ceramics. The model has been then applied to predict the micro-cracking of the YSZ skeleton induced by the Ni re-oxidation. The results of the simulations are reported in the fifth chapter with a discussion on the impact of the microstructural properties on the mechanical redox stability of the hydrogen electrode.

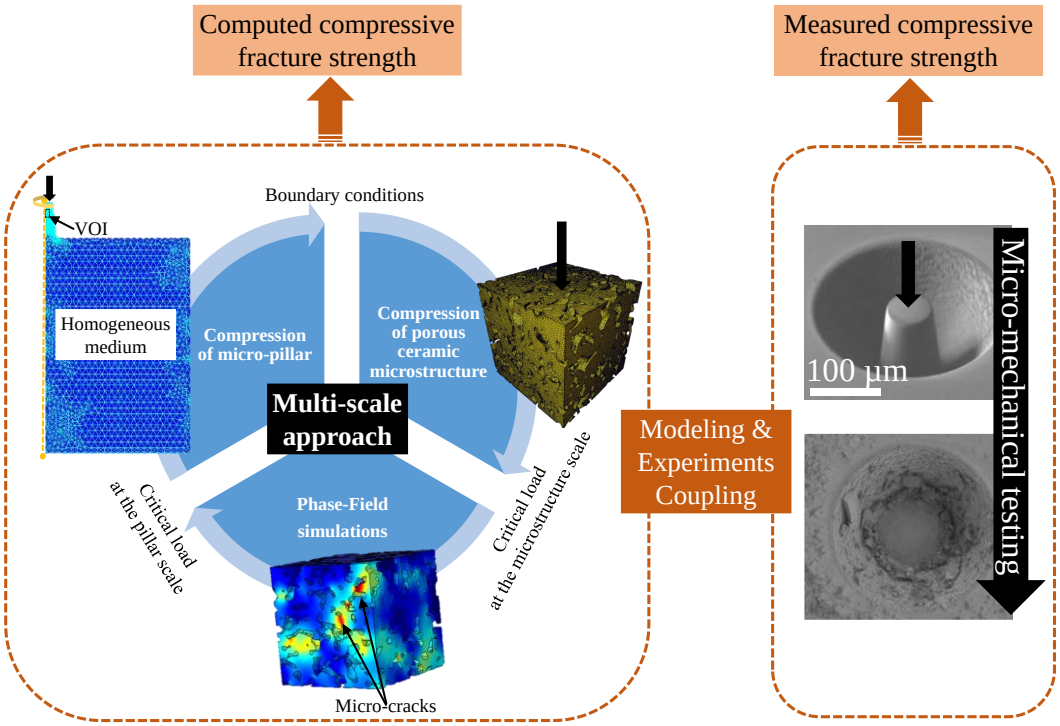

Fig I- 15. Overview of the methodology of the thesis: multi-scale approach coupling modeling and micro-scale experiments.

II. Fracture properties of porous yttria-stabilized zirconia under micro-compression testing[1]

Despite the various advantages of the high-temperature technology, the SOC is still submitted to degradation phenomena that limit its lifetime. As discussed in chapter one, the cell is subjected to significant internal stresses due to the high operating temperature and the mismatch in thermal expansion coefficients between the SOC components. In particular, these thermomechanical loadings can lead to mechanical damage in the hydrogen electrode with the creation of micro-cracks within the YSZ backbone [23,44,45,99]. Moreover, the Ni in the hydrogen electrode is liable to re-oxidize into NiO in case of system failures such as the re-introduction of air during the system shutdown. Because of the Ni volume expansion upon re-oxidation, high tensile stresses are generated in the YSZ skeleton leading to the generation of micro-cracks [53,54,100,101]. It has been shown that the mechanical damage in the hydrogen electrode can affect significantly the overall cell performance [54–56,100].

[1] The results of this chapter have been published in Journal of European Ceramic Society.

Several studies have been dedicated to assess the mechanical degradation of the hydrogen electrode and to quantify its impact on the global cell performances [48,53,60]. In this frame, characterizations campaigns have been carried out on the porous cermet to determine its Weibull properties allowing the calculation of the failure probability [102–104]. However, data on the fracture properties of YSZ ceramic as a function of its porosity is currently incomplete for the prediction of local fracture in the electrode. The toughness of 3YSZ has been measured by double-torsion over a large range of porosity [75]. Nevertheless, the compressive fracture strength for the 8YSZ has been measured only at high porosity (65-77%) on millimetric macroscopic samples [41,105] whereas no data is available for 3YSZ. As the thickness of the cermet substrate does usually not exceed 400 µm [40], special care should be taken when using fracture properties measured at the macroscopic scale. Indeed, a change in the fracture strength and in the mechanism of fracture can occur when reducing the sample size. To date, no data is available on the mechanical properties of porous YSZ at small scale, even if micromechanical testing is becoming more common on other types of materials [106–109].

In the last decades, micro-mechanics has received ever increasing interest thanks to advances in sample manufacturing and preparation techniques such as electrodeposition and Focused Ion Beam (FIB) machining [110–112]. In the literature, sophisticated geometries such as micro-cantilever and micro-tensile specimen have been tested under bending and tensile tests [113–115] whereas micro-pillars have been tested under uniaxial compression [111,116]. To date, micro-compression testing has been conducted on dense materials such as gold, zirconia and metallic alloys, on composite such as wood, and porous metals such as silver [106,110,117–119]. To the best of our knowledge, the mechanical characterization of porous ceramics under micro-compression has never been addressed and thus adequate methods for the preparation of porous ceramic micro-pillars are yet to be developed.

The first objective in this thesis is to characterize the fracture properties of porous YSZ ceramic, as a key material component in SOC, by the micro-compression testing of pillars with microstructures and dimensions representative of the hydrogen electrode. The study has been mainly focused on the characterization of the 8YSZ material as a function of porosity (33-63%) while the behavior of 3YSZ has been complementarily investigated at high porosity (63%). A main rationale behind the measurements presented in this chapter two is the generation of data amenable for model validation, which is the focus of chapter four.

In the first section, the experiments and the methodology are detailed with the preparation of micro-pillars, the micro-compression testing and the different techniques used for

microstructural characterizations. In the second section, the results are presented and discussed. The compressive fracture strength measured as a function of porosity is analyzed and compared to the few data on macroscopic samples available in the literature [41,105]. This comparison allowed addressing sample size effects on the compressive fracture strength. Finally, using FIB - Scanning Electron Microscope (FIB-SEM), the fracture mode of the YSZ ceramic under compression is analyzed as a function of its porosity.

II.1. Experiments and methodology

II.1.1. Sample preparation

Micro-pillars for the compression tests were milled in macroscopic porous YSZ pellets. The protocols of the sample preparation are detailed in the sections hereafter.

II.1.1.1. Pellets at intermediate porosities (<50%)

To obtain samples at intermediate porosities (<50%), 8YSZ powder was partial sintered at different temperatures. A commercial Tosoh TZ-8YSB powder was first compacted under an uniaxial compression load of 156 MPa. The compacted pellets were then heated in air for five hours to reach the sintering temperature, which was maintained for one hour. Afterwards, all pellets were cooled down to room temperature during five hours. In order to change the pore volume fraction, four different sintering temperatures (*i.e.* 1270°C, 1230°C, 1200°C and 1150°C) were selected based on the 8YSZ dilatometry curve, leading to pellets with different porosities. It should be noticed that several pellets were produced at each given sintering temperature. After sintering, the pellet dimensions were around 9 mm in diameter and 3 mm in thickness. To prepare the pellets for the compression test, their upper surfaces were mechanically polished. The protocol consisted in polishing the samples with a series of diamond suspensions down to 1 µm with a last step using a vibratory finishing machine (Struers tetra force 5). As a result, flat surface with limited roughness was obtained.

II.1.1.2. Pellets at high porosities (> 50 %)

To obtain pellets at porosities higher than 50%, a typical Ni-8YSZ cermet support was used to complement the study. The protocol reported in Laurencin et al. [120] was used to remove the Ni from the 8YSZ backbone and is briefly reminded hereafter. Firstly, as the cermet is under

its oxidized state after manufacturing, the NiO particles were reduced into Ni. For this purpose, the NiO-YSZ substrate was heated up to 800°C at a rate of 5°C.min^{-1} under a gas mixture of (2% H_2+Ar). The substrate was then maintained under these reducing conditions for 48 h up to the complete reduction of NiO into Ni before being cooled down to room temperature. The substrate in reduced state was then treated two times in a solution of nitric acid (65% HNO_3) for 4 hours at room temperature. This procedure completely removed the Ni, revealing the zirconia backbone. As a result, a highly porous 8YSZ sample was obtained.

The same protocol was also applied on a Ni-3YSZ cermet support. The highly porous 3YSZ substrate obtained after Ni dissolution was used to compare the fracture properties with 8YSZ at a similar porosity.

II.1.1.3. Porous micro-pillars

The micro-pillars for the mechanical testing were milled in the porous 3YSZ and 8YSZ pellets using a Xe^+ plasma FIB (pFIB). The pFIB technology was chosen as it is able to form a high current beam allowing to etch specimens in a short time [121–124]. The target dimensions for the micro-pillars were chosen to fulfill specific criteria. Firstly, the size of pillar must be sufficiently large in order to be representative of the electrode microstructure and to neglect the influence of ion irradiation [107,121]. Knowing that the microstructural characteristic length is roughly estimated to 1 µm (*cf.* section II-2.2), a diameter of at least 40 µm is required to be representative of the investigated microstructures [125]. Secondly, an aspect ratio, defined as the ratio between the pillar height and its upper diameter, ranging between 2 and 3 is recommended in the literature for micro-compression testing [126,127]. Thirdly, the pillar section was also chosen considering the measurement range of the nano-indenter force sensor to be able to reach the critical loading triggering fracture. Considering all these constrains, the target dimensions of the micro-pillars were set to 60 µm in diameter and 130 µm in height.

Since ceramic zirconia is an electrical insulator, the milling was carried out under charge neutralizer atmosphere to evacuate the charges, and hence, to minimize ion beam shifting. The milling was performed at an accelerating voltage of 30 kV with a beam current of 0.47 µA. This rather low current was chosen as a tradeoff to limit the so-called "curtaining effect" while keeping an acceptable milling time. Indeed, this "curtaining effect" is here promoted by the presence of porosities and absence of electron or ion beam assisted deposition layer when the milling is performed at a too high current, which degrades the external surface of the pillar

[128]. In the present work, milling was conducted using circular pattern for a duration of about 4 hours. It is worth noting that the Xe^+ beam has a Gaussian shape resulting to produce tapered pillars. This geometrical feature can have a significant impact on the compression testing by inducing a significant gradient in the stress field inside the pillar. Therefore, even if the taper angle is unavoidable, the protocol adopted in this work has successfully enabled to obtain micro-pillars with taper angle not exceeding 7° (Fig. II-1). It can be noticed that a milling current higher than 0.47 µA led to higher taper angle.

With the idea of preparing several pillars in the same porous pellet, labelling each pillar was needed for identification before testing. Thus, a silver coating was deposited on a small edge of the upper surface of the sample. To ensure the precise positioning of the indenter on the head of the pillar and to avoid contact with the substrate surface during the compression, a trench of ≈100 µm surrounding the pillar was milled: this procedure results in a well of ≈260 µm with the micro-pillar at the center as shown in Fig. 1. Furthermore, the adjacent wells were milled at a minimal distance of 500 µm to neglect the influence of the surrounding pillars on the tested one as discussed in Camposilvan et al. [106].

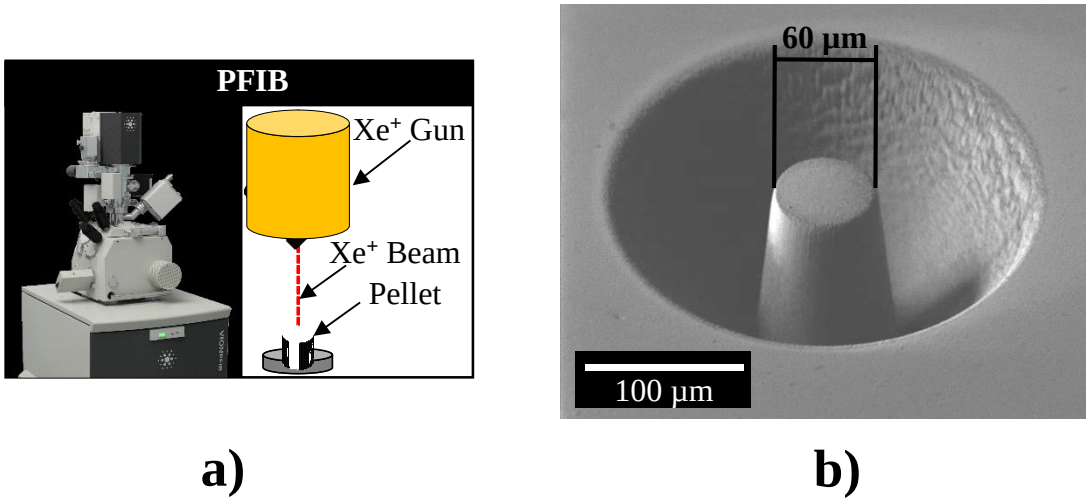

Fig II- 1. Procedure for micro-pillar preparation: a) schematic representation of the Xe^+ pFIB, b) example of a typical specimen obtained after the milling.

II.1.2. Micro-compression testing

The compression test was selected in this study for several reasons. As previously mentioned, the hydrogen electrode is submitted to complex loadings during operation as well as in the case of Ni re-oxidation, leading to its mechanical damage. The fracture of the YSZ skeleton occurs

in the regions subjected to tensile and bending stresses. In this view, the compression testing of porous YSZ specimens is relevant since it allows generating local tensile stresses in the microstructure. Besides, under compression, an approximately quasi-uniform macroscopic stress distribution is created within the micro-pillar facilitating the analysis of the test results. The compression test was performed using a nano-indenter (G200, Keysight technologies, USA) equipped with a diamond circular flat punch tip of 100 µm in diameter associated to an optical microscope. This instrument is controlled by a set of parameters, which can affect the experimental results. Before starting the mechanical testing, calibration of the indentation set up is thus required. First, if the flat punch tip surface is not parallel to the top surface of the pillar, non-homogeneous stress distribution can be generated in the pillar with a flexure moment in addition to the solicitation in compression. Attention was thus paid to correct the misalignment between the flat punch tip and the pillar upper surface. For this purpose, the optical microscope was used to correct the tilt angle of the sample surface with respect to the punch tip. Secondly, attention was paid to calibrate the positioning of the indenter on the tested micro-pillar with the microscope.

The compression testing was conducted under monotonic loading at a constant strain rate of 0.05 s^{-1}. As the diameters slightly increase from the top to the bottom in the tapered pillar, a non-uniform stress field is created under compression, with highest stress in the top surface of the pillar. The engineering stress-strain curve was thus computed from the load-displacement data based on the initial pillar geometry (*i.e.* top surface diameter and total height).

In the present work, for each tested material (either 8YSZ or 3YSZ at a given porosity), at least five pillars were compressed until total failure to measure the compressive fracture strength. Complementary experiments on additional pillars consisted in stopping just before the samples collapse in order to detect the cracks created within the YSZ skeleton and thus to assess the material damage behavior.

II.1.3. Microstructural characterizations

The validation of the protocol applied for the preparation of porous YSZ samples (*cf.* section II-1.1) as well as the detection of the damage after testing were carried out using several microstructural characterization techniques.

II.1.3.1. Scanning Electron Microscopy (SEM) observations

After the sintering step, polished cross-sections of each material were observed by Scanning Electron Microscopy (SEM) to assess the microstructure homogeneity and to estimate the sample porosity. For this purpose, one sample from each batch was impregnated with an epoxy resin to fill the pores, then subsequently cut and polished to prepare the cross-section for SEM imaging. As zirconia is an insulating material, a carbon layer was deposited on the sample surface to avoid charge accumulation during SEM observations. A Field Emission Gun – Scanning Electron Microscope (FEG-SEM Zeiss Merlin, Germany) was used for the imaging. The micrographs were acquired with a pixel size of 10 nm using the Everhart-Thornley Secondary Electron (SE) detector at an accelerating voltage of 3 kV.

Aside from the polished cross-section micrographs, all the pillars were also systematically observed after testing at low magnification by SEM in Secondary Electron (SE) mode (accelerating voltage of 3 kV and working distance of 13 mm). Besides, the internal damage was characterized for the specimen that were unloaded just before the final fracture. In this case, the cracks are expected to nucleate in the upper part of the pillar (i.e. in a zone close to the top of the specimen) where the stresses are the highest. Therefore, 2D cross-sections localized in this zone of the tested pillars were polished using FIB-SEM (Crossbeam 540, Zeiss) at a milling current between 0.7-3 nA for the Ga^+ beam. A conducting Au layer was deposited on the top surface of the pillar to limit charge accumulation and beam shift during sputtering. For practical reasons, it can be noticed that the impregnation of the microstructure by an epoxy resin is not possible in this specific case. The SEM images of the 2D FIB slices were acquired under conditions representative of 3-D imaging, *i.e.,* acceleration voltages between 1.5-1.7 kV and current of 0.5-1.5 nA. Electron images from the secondary electrons Everhart-Thornley and in-lens energy-selective backscatterer were recorded for each region of interest. It can be noticed that the same procedure was applied to confirm that the microstructure of the YSZ skeleton was not affected by the dissolution of Ni in nitric acid, for the samples at high porosities before testing.

II.1.3.2. Reconstructions by FIB-SEM and synchrotron X-ray holotomography

The microstructure of all the types of investigated samples were reconstructed for the accurate measurement of 3-D characteristic properties including the pore volume fraction. The 3D volumes were also used to verify the microstructure homogeneity of the tested materials.

3D reconstructions by FIB-SEM – For the pellets at intermediate porosities, the microstructural reconstructions were obtained by FIB-SEM (FEG-SEM NVISION 40, Carl ZEISS®) slice and view. The porosities were previously filled by an epoxy resin to help the subsequent image segmentation. The energy selective backscatter (ESB) detector with a low acceleration voltage of 1.5 kV was used for the electron images. Volumes of around 17^3 µm^3 were acquired for the samples sintered at 1270°C, 1230°C, 1200°C and 1150°C with a voxel size of 10^3 nm^3.

The same procedure was also used to check that the milling procedure using pFIB for the micro-pillar preparation does not affect its microstructure. For this purpose, two 3D FIB-SEM (Zeiss Crossbeam 540, Atlas Fibics) reconstructions were obtained for the pellet sintered at 1270°C: the first one was acquired directly in one micro-pillar while the second one was taken just aside the well in which the specimen is centered (*cf.* Fig. II-6). Then, a set of microstructural properties was computed and a comparison between the results on the two 3D reconstructions was performed.

3D reconstructions by synchrotron X-ray holotomography – Regarding the highly porous samples, the mean diameter of the pore phase is significantly larger compared to the sintered pellets. Besides, the highly porous 8YSZ sample contains macro-pores (approx. 3 to 4 µm in size). Therefore, to be representative of this type of microstructures, large reconstructed volumes, bigger than the one obtained by the FIB-SEM serial sectioning, are required [125]. For this purpose, the microstructure for the 3YSZ and 8YSZ highly porous samples were reconstructed at the Nano-Imaging Beamline (ID16A) of the European Synchrotron Radiation Facility (ESRF) using X–ray nano-holotomography [129,130]. Before proceeding to X–ray tomography, pillars of around 60 µm in diameter were milled in the highly porous 8YSZ and 3YSZ pellets using pFIB (Fig. II-2). Then, they were extracted using a micro-manipulator and fixed on a tip holder suitable for the X–ray tomography measurements. Afterwards, two reconstructions of $51.2 \times \pi \times 25.6^2$ µm^3 were obtained for 8YSZ and 3YSZ with a voxel size of 25^3 nm^3.

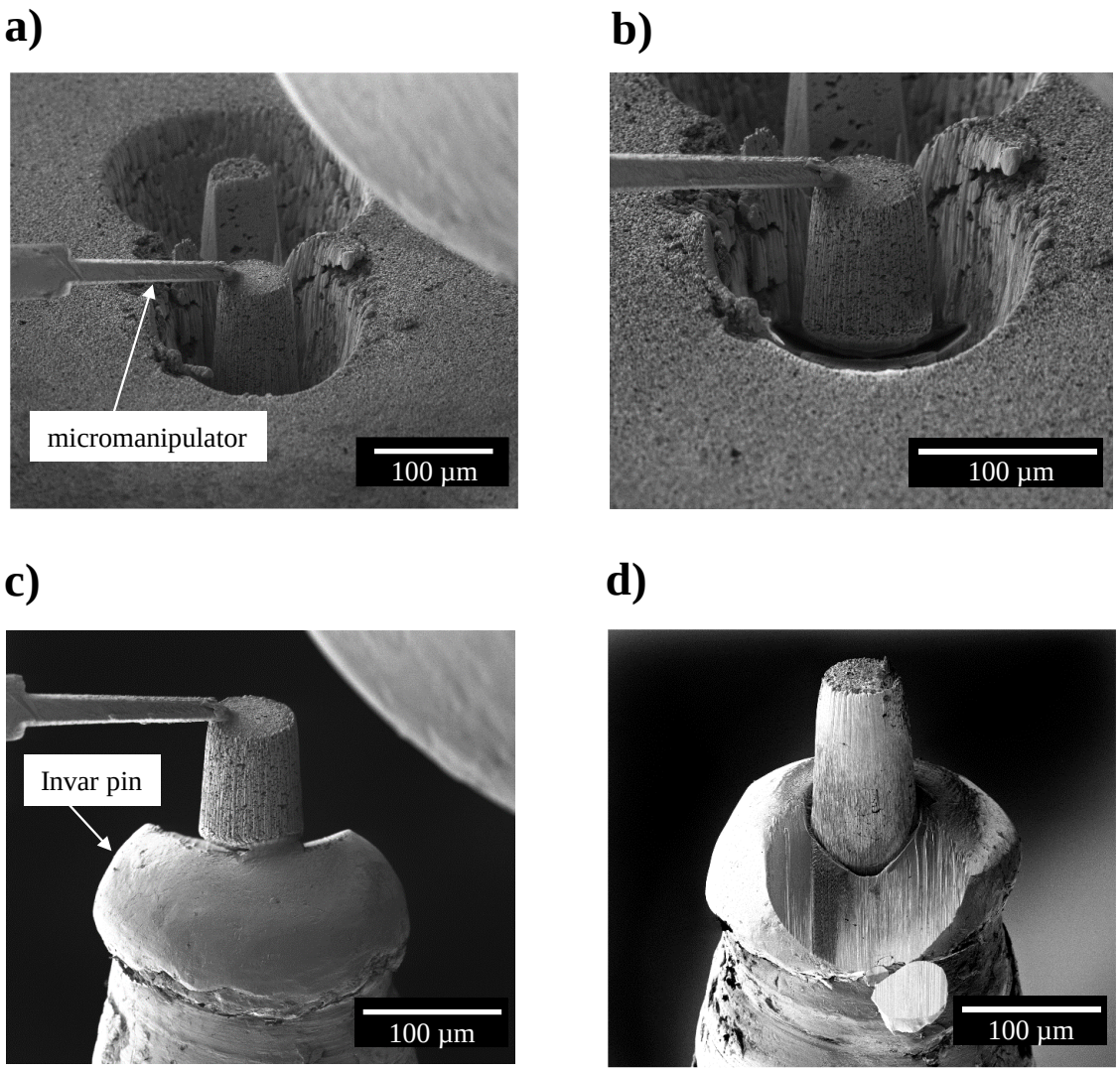

Fig II- 2. Specimen preparation procedure for X-ray tomography: a) fixation of the micromanipulator on the pillar, b) extraction of the pillar from the pellet, c) pillar moved by the micromanipulator to the invar pin, d) pillar mounted on the invar pin.

II.2. Results and discussions

II.2.1. Sample preparation

II.2.1.1. Porous pellets preparation

The microstructure of porous 8YSZ pellets after partial sintering and after Ni dissolution was characterized by image analysis on SEM micrographs of polished cross-sections (Fig. II-3).

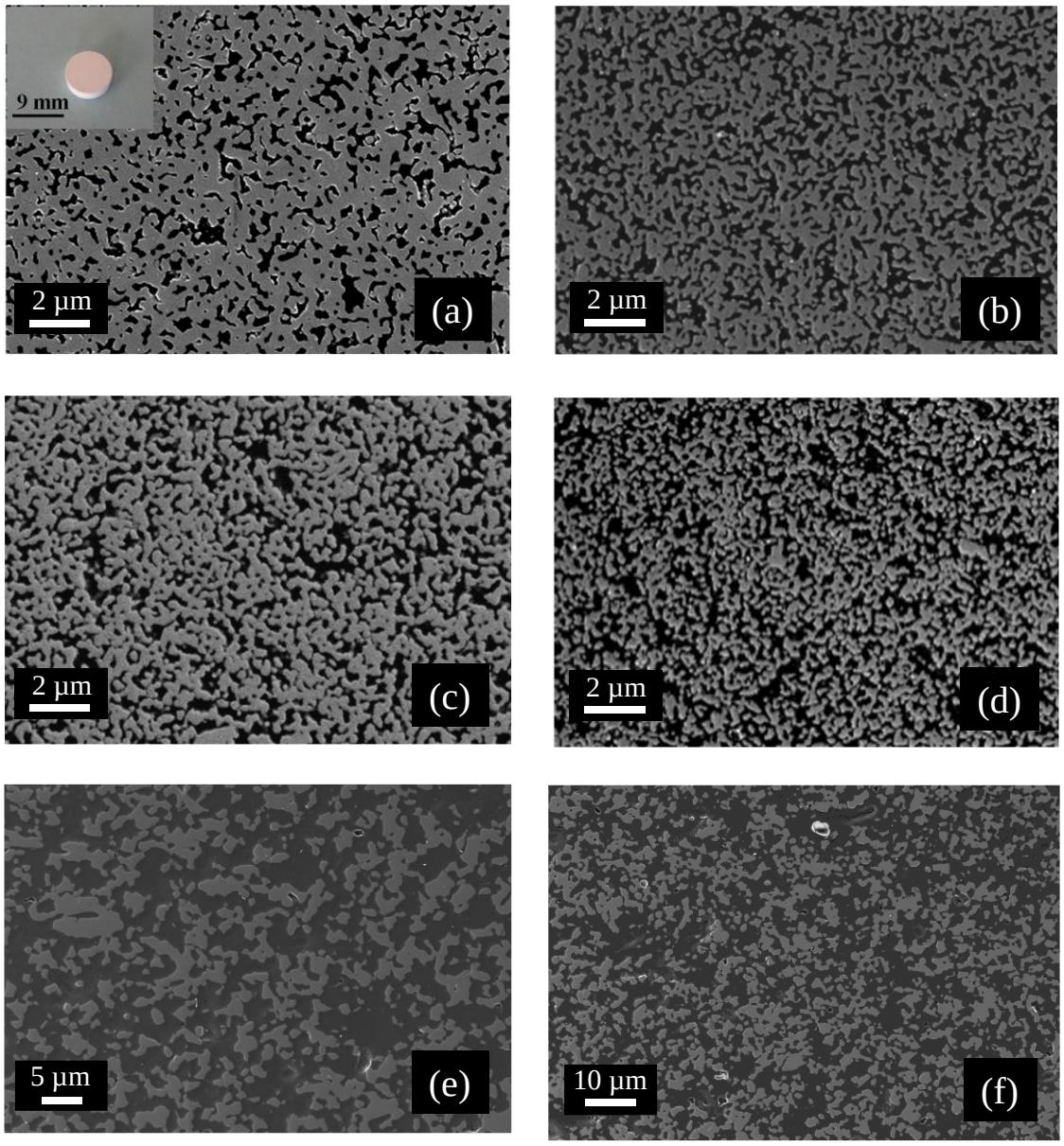

Fig II- 3. Secondary electrons SEM micrographs of 8YSZ samples prepared by partially sintering under air at: a) 1270°C, b) 1230°C, c) 1200°C, d) 1150°C. e) and f) SEM observations of the 8YSZ sample obtained by dissolving the Ni present in a cermet substrate for two magnifications. The insert in Fig. 3a shows the pellet after sintering.

For the partially sintered pellets, the micrographs were taken in a region of interest close to the top surface of the pellets, where the micro-pillars are milled. As shown in Fig. II-3a-d, SEM observations reveal that the microstructures of these samples are homogeneous with a rather uniform distribution of pores. When the sintering temperature is lowered from 1270°C to 1150°C, the porosity fraction is increased with a significant decrease in the 2D connectivity of the solid phase at the lowest temperature (Fig. II-3d). It can be pointed out that pellets sintered

below a temperature of 1150°C showed no cohesion indicating a complete loss of the macroscopic percolation for the solid phase. It has been also checked that the microstructure remains homogeneous over a depth of about 200 µm from the top surface to the bulk of the pellets. This dimension exceeds the typical height of the pillars (*i.e.* ≈130 µm) meaning that there is no porosity gradient in the volume of the tested specimen. Nevertheless, a decrease in the porosity was detected at longer range, going from the top surface to the center of the pellet. As an illustration, for the sample sintered at 1270°C (Fig II-4), the porosity measured next to the pellet surface was 33 % while the global estimation based on Archimedes principle has provided a porosity of 26 %. As a result, the manufacturing process adopted to produce porous 8YSZ pellets would not be appropriate for compression testing at macroscopic scale.

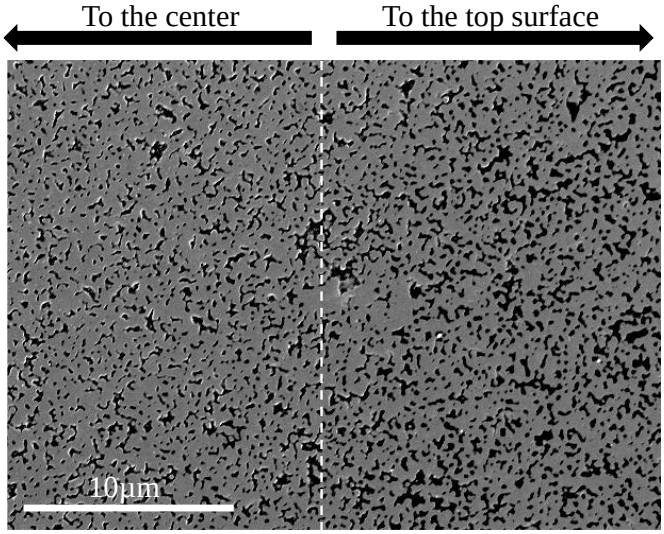

Fig II- 4. Porosity gradient in the sample sintered at 1270 °C.

Finally, the surface quality of the sintered pellets was also checked using optical microscopy. It has been found that after the mechanical polishing, the pellets are flat with a very slight residual roughness on the upper surface. It can be thus claimed that the protocol including the choice of the sintering temperatures and polishing conditions is validated for the preparation of the 8YSZ pellets at intermediate porosities (<50%).

SEM observations of the highly porous 8YSZ sample (Fig. II-3e) after Ni dissolution have revealed a rather heterogeneous microstructure with some large pores randomly distributed in the volume. The presence of these macro-pores is explained by the use of a pore-forming agent during the manufacturing.

It must be pointed out that a special attention was paid to the Ni dissolution procedure in order to avoid YSZ surface decomposition by the nitric acid attack. For instance, as shown in Fig. II-5a, defects such as holes at the surface of the 8YSZ skeleton were detected on a FIB-SEM cross section of a non-impregnated sample treated in nitric acid three times for 4h under accelerated conditions using a magnetic stirrer (Fig. II-4a). The improved procedure, which repeats the treatment in the nitric acid solution only twice without stirrer (*cf.* section II-1.1.2) allowed to dissolve the Ni by preserving the 8YSZ surface as shown in Fig. II-5b. Then, the same protocol was used to obtain the highly porous 3YSZ sample. Its microstructure was also checked after the Ni dissolution. As for 8YSZ, alterations of the 3YSZ skeleton after Ni dissolution were not observed in SEM electron images.

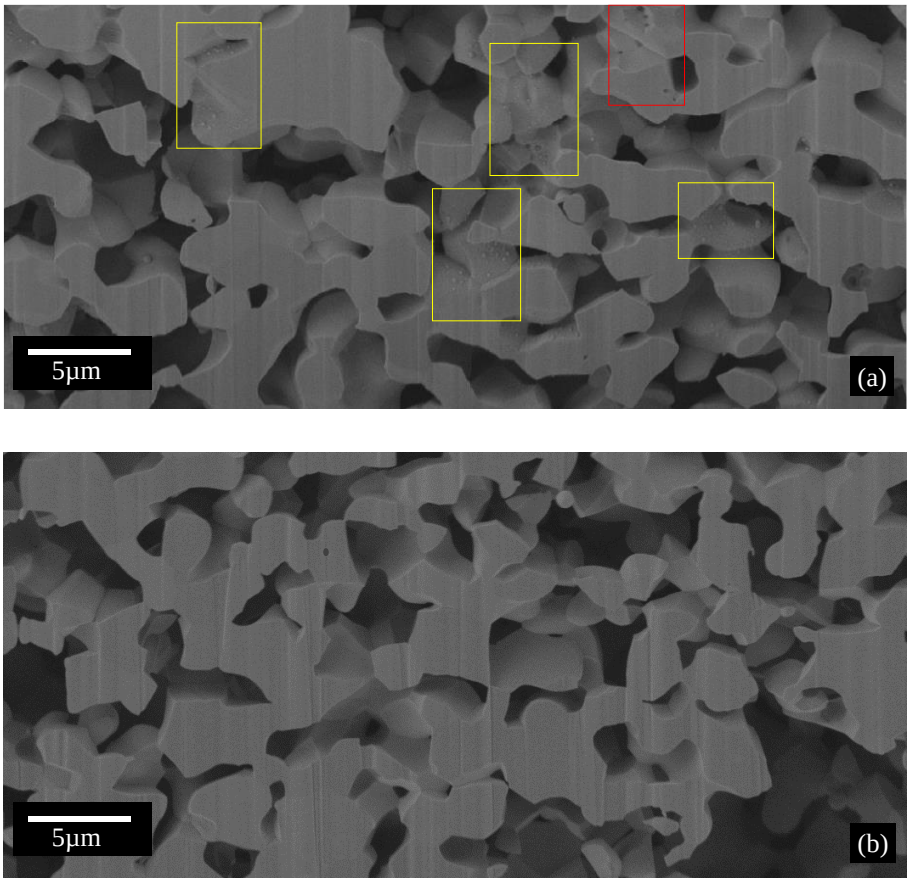

Fig II- 5. Comparison between two FIB-SEM secondary electron cross-sections of microstructures obtained after dissolution of the Ni: a) with defects (highlighted by red and yellow rectangles), b) without defects (i.e. obtained by the validated protocol).

The 3D reconstructions of the pellets at intermediate and high porosities are displayed in Fig. II-6. As shown in Fig. II-6a-b, the microstructures of the partially sintered pellets are homogeneous with an increase in the solid phase size when densifying the sample. For highly porous specimens (Fig. II-6c-d), the 3D reconstructions did not detect alterations of the YSZ

skeleton after Ni dissolution. All the visual inspections of 3D volumes confirm the conclusions deduced from the 2D observations.

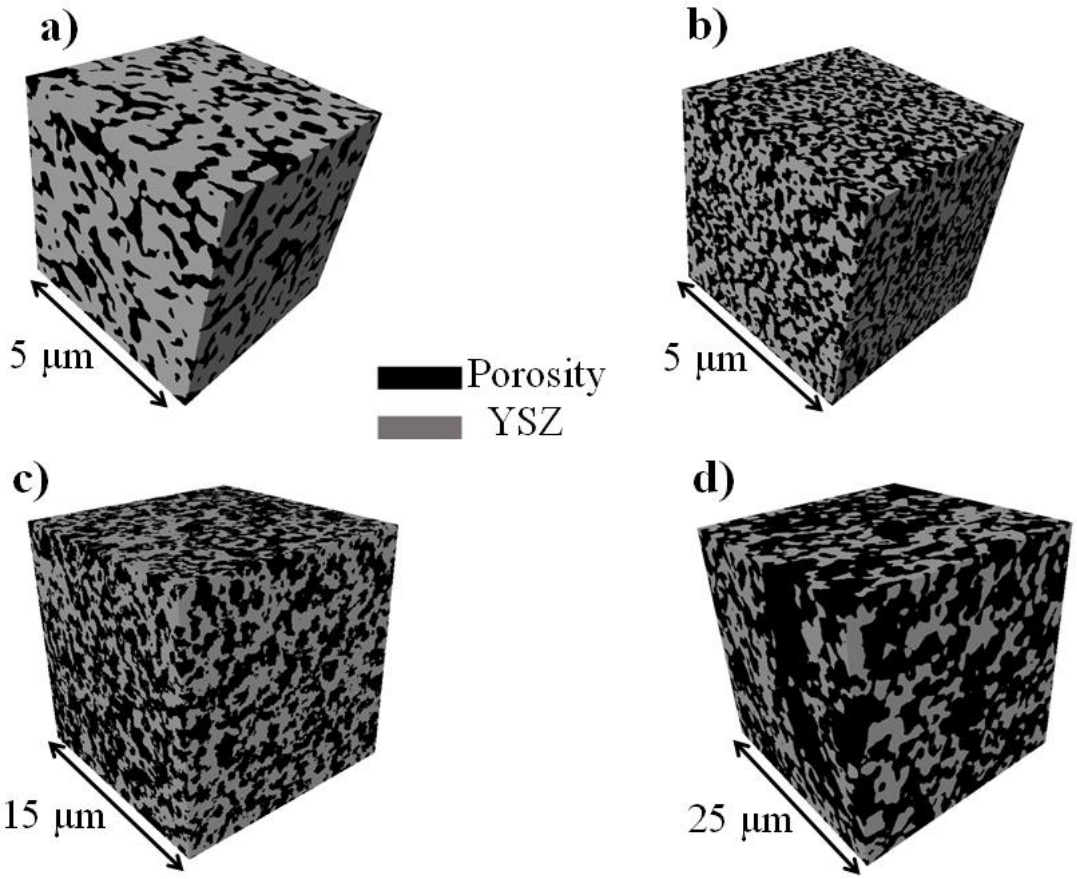

Fig II- 6. 3D rendering segmented volumes of FIB-SEM reconstructions of porous 8YSZ samples sintered at: a) 1270°C, b) 1150°C and of the whole X-ray holotomography reconstructions for c) highly porous 3YSZ, d) highly porous 8YSZ samples.

II.2.1.2. Microstructural stability upon pFIB pillar milling

As mentioned in section II-1.3.2, the impact of pFIB milling on the microstructural properties was assessed considering two 3D reconstructions, one taken in the pillar and the second one in a region close to the well in which the specimen is centered (for the pellet sintered at 1270°C: *cf.* Fig. II-7). For this purpose, the tortuosity factor as well as the specific area for solid phase were computed using a set of programs detailed in the work of Moussaoui et al. [131]. It has been found that the tortuosity factor of the solid phase remains almost unchanged, being equal to 1.349 and 1.389 in the pellet and in the pillar after milling, respectively. For the solid phase specific surface area, only a very slight variation was detected between the two volumes, which is more probably due to local variations in the microstructural properties (*i.e.* solid phase specific surface area is equal to 6.85 μm^{-1} and 6.51 μm^{-1} before and after the milling). The

absence of cracks in the material was also checked after milling. These results show that the microstructure is not affected by the pillar preparation and are in good agreement with the literature. Indeed, it has been shown in [121] that Xe ion implantation is limited to a few nanometers from the external surface and does not induce any damage in the bulk of the etched sample. As a result, the preparation of the pillar by pFIB is validated for the mechanical testing. It is worth noting that the methodology described in the present work could be adopted to prepare micro-pillars made of other porous ceramics.

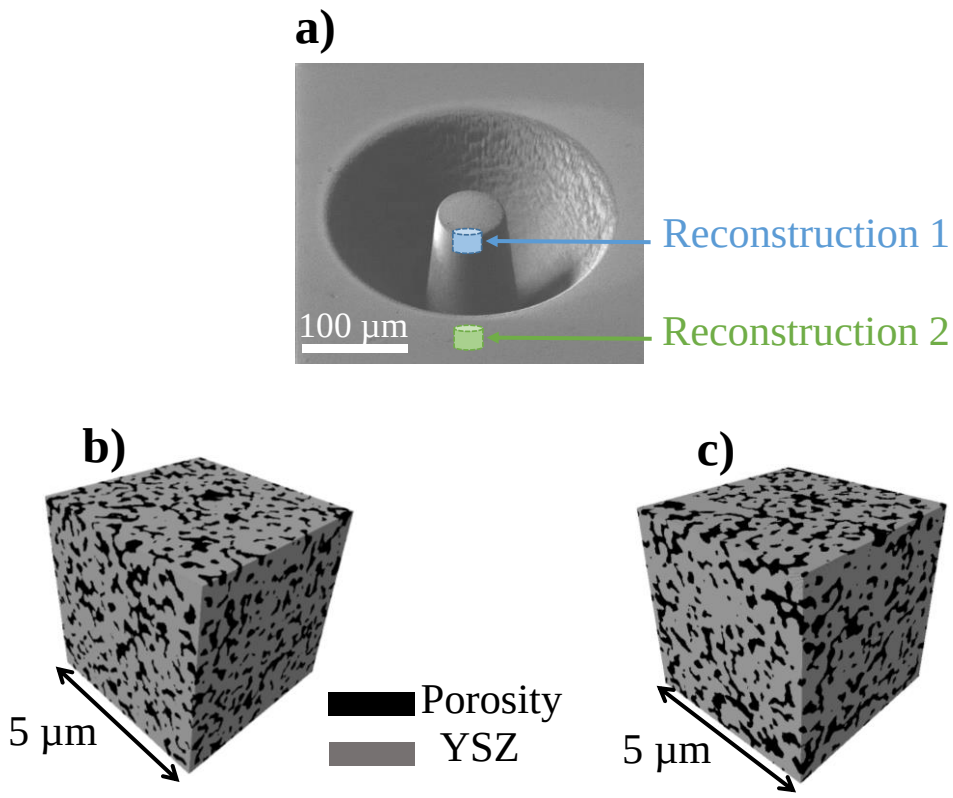

Fig II- 7. FIB-SEM segmented reconstructions of the sample sintered at 1270°C: a) illustration of the two regions of interest, 3D rendering volumes extracted from the whole FIB-SEM reconstructions b) Reconstruction 2: nearby the well in which is the pillar is centered, c) Reconstruction 1: in the pillar.

II.2.2. Microstructural properties: pore volume fraction and phase size distribution

The porosity fraction was initially estimated on segmented 2D SEM images. For this purpose, several SEM micrographs were taken for each type of pellet. The porosity estimation was further confirmed by measuring the property on the 3D reconstructions (Table II-1). This pore volume fraction was directly given by the percentage of voxels associated to the porous phase. On the one hand, it has been found that the porosity varies from 33 ± 1 % to 49 ± 1 % when decreasing the sintering temperature from 1270°C to 1150°C for the 8YSZ partially sintered

materials. On the other hand, a same porosity equal to 63 ± 3 % was measured on the both 3YSZ and 8YSZ cermet substrates obtained after Ni dissolution. It can be noticed that the slight uncertainty in the measurements of the local porosity is mainly related to the image segmentation step. For example, the operations of erosion and dilatation by a voxel (or a pixel) in 3D (or 2D) segmentation of the investigated microstructures leads to a variation in the porosity measurement ($\leq \pm 3\%$).

As expected, the comparison between the investigated microstructures showed that the highly porous samples obtained from SOC cermet supports are more heterogeneous than the partially sintered ones (Fig. II-6). It can be also seen that the porosity size of the highly porous 8YSZ sample is significantly larger than in the other samples due to the use of pore former (Fig. II-6d).

In order to quantify the difference between the investigated samples, a set of microstructural properties was assessed on 3D reconstructions. The continuous phase size distribution (PSD, *i.e.* the granulometry curves) was computed using morphological openings as described in [12,131]. The mean phase diameter, which corresponds to the particle size associated to 50% of the cumulative phase size distribution, was also determined from the granulometry curve.

Table II- 1. Microstructural properties of the investigated samples computed on 3D reconstructions.

Preparation method	Pore volume fraction [%]	Solid phase mean diameter [µm]	Porous phase mean diameter [µm]
Partial sintering at 1270°C for 8YSZ sample	33 ± 1	0.23	0.13
Partial sintering at 1230°C for 8YSZ sample	36 ± 1	-	-
Partial sintering at 1200°C for 8YSZ sample	40 ± 1	-	-
Partial sintering at 1150°C for 8YSZ sample	49 ± 1	0.09	0.09
Dissolution in nitric acid of Ni for 8YSZ cermet substrate	63 ± 3	0.62	0.99
Dissolution in nitric acid of Ni for 3YSZ cermet substrate	63	0.25	0.33

For this purpose, volumes of 5^3 µm^3 were used in the case of partially sintered samples. For the sake of clarity, the solid and porous phase size distributions are shown in Fig. II-8a only for the

8YSZ samples sintered at the highest and the lowest temperatures (*i.e.* T=1270°C and T=1150°C). The comparison between the two granulometry curves shows a similar shape. Nevertheless, the microstructure sintered at 1270°C is characterized by wider size distributions for the two phases as compared to the ones sintered at 1150°C. Moreover, as expected, the size of the solid phase increases with increasing the sintering temperature due to the coarsening of the microstructure. Therefore, the size of 8YSZ phase is larger when the sintering temperature is higher with a significant increase in the mean particle size (*i.e.* solid phase mean diameter equal to 0.23 µm and 0.09 µm for the samples sintered at 1270°C and 1150°C, respectively as reported in Table II-1). The porous phase mean diameter was found equal to 0.13 µm and 0.09 µm for the samples sintered at 1270°C and 1150°C, respectively.

The microstructural properties of highly porous 8YSZ sample have been calculated considering a larger volume of 25^3 µm^3 as the sample contains larger local heterogeneities. As shown in Fig. II-8b, the granulometry plot for the solid phase exhibits a nearly symmetric distribution around a mean value while a significant dissymmetry is observed in the distribution of the porous phase. This special feature in the PSD for the porous phase is related to the presence of a large number of macro-pores in the investigated microstructure. Moreover, the pore mean diameter, equal to 0.99 µm, is considerably larger than the ones measured for the partially sintered 8YSZ samples at intermediate porosities. This difference is mainly due to the use of pore former during the manufacturing and to the Ni phase, which was removed from the sample. It can also be noticed that the solid phase size presents a wide distribution with a solid phase mean diameter equal to 0.62 µm (Table II-1).

For the highly porous 3YSZ sample, the phase size distribution was computed considering a volume of 15^3 µm^3 adapted to the size of the heterogeneities in this microstructure (Fig. II-6c, II-8c). It can be seen that the PSD of the porous phase has an almost symmetric shape. A slight dissymmetry in the curve can be noticed for the highest values of particle diameter illustrating a rather limited heterogeneity of the microstructure. A mean pore diameter of 0.33 µm is found for this 3YSZ sample. This value is much lower than the one of the 8YSZ sample although the same pore volume fraction is maintained. This result is explained by the macro-pores present in the highly porous 8YSZ sample, generated by pore-forming agents. Finally, it can be noted that the solid phase mean diameter of the highly porous 3YSZ sample, equal to 0.25 µm, is in the same range as the one computed on the 8YSZ sample sintered at 1270°C (*i.e.* 0.23 µm) (Table II-1).

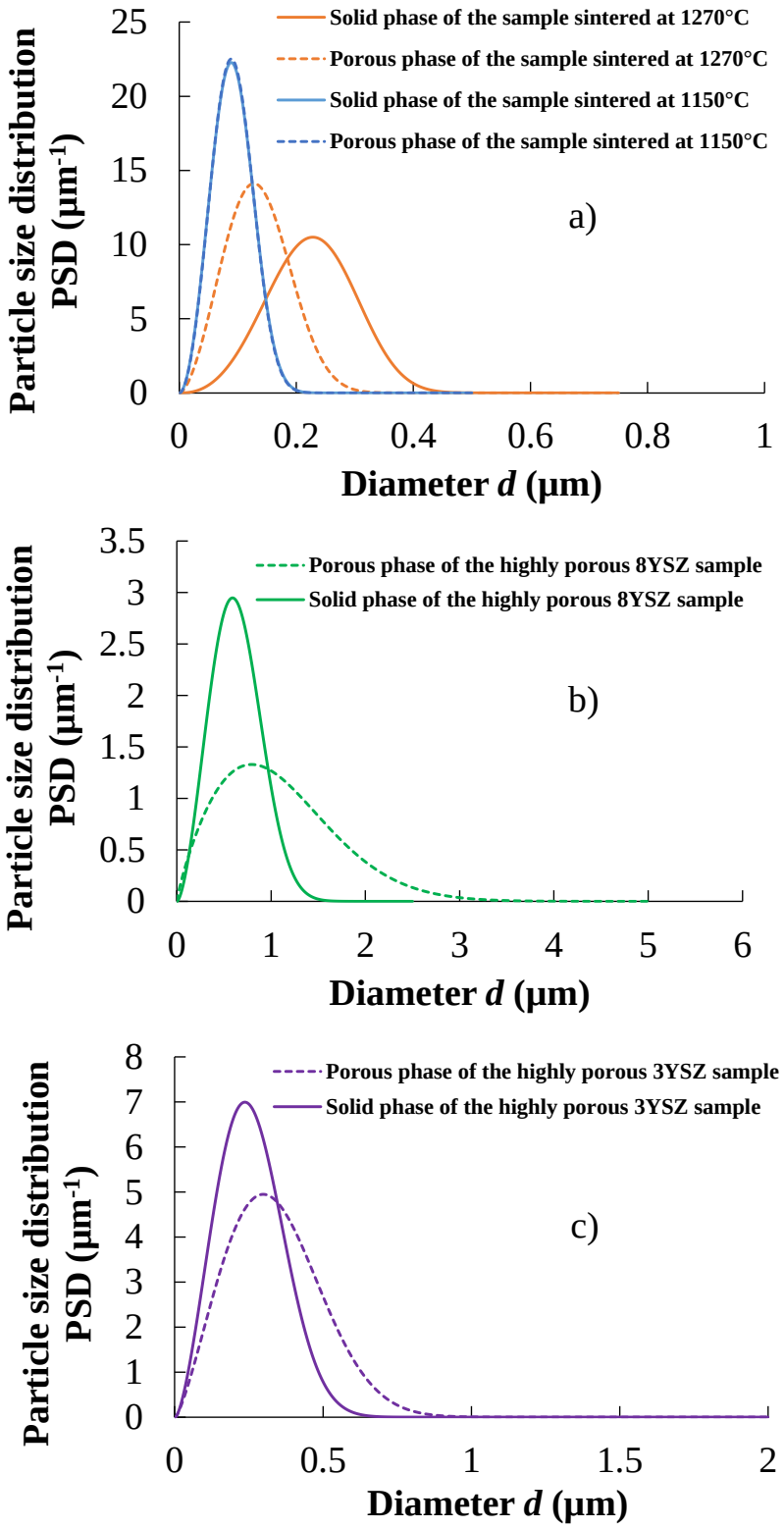

Fig II- 8. Particle size distributions of the solid and porous phases of: a) 8YSZ samples sintered at 1270°C (porosity: 33%) and 1150°C (49%), b) highly porous 8YSZ sample (63%), c) highly porous 3YSZ sample (63%).

To conclude, 8YSZ samples with a wide range of porosities from 33% to 63% were obtained allowing to test the influence of porosity fraction on the compression fracture strength. The volume fraction and PSD calculations let anticipate meaningful comparison of the mechanical behavior of highly porous 8YSZ and 3YSZ, despite the slight differences in their microstructures.

II.2.3. Micro-compression testing results

Two series of micro-compression tests were conducted on porous YSZ pillars under monotonic loading, just before specimen fracture and up to specimen collapse (*cf.* section II-1.2). The load-displacement response of each type of sample in the first series is displayed in Fig. II-9. It can be noticed that the behavior during loading is not perfectly linear especially at low displacements. During this initial stage, the pillar presents a low apparent stiffness that must be explained by the progressive setting of the contact between the specimen and the flat punch indenter. Indeed, as discussed in [106], this first non-linear step can be ascribed to the compression of the surface defects on the top of the pillars such as roughness or possible presence of some debris. It can be mentioned that this explanation is consistent with the fact that this non-linear behavior was found to be much larger on preliminary tests when the surface of the pellets were not carefully polished according to the procedure described in section II-1.1.1. This result highlights the crucial role of the surface preparation for the micro-compression testing.

This first nonlinear stage in the load-displacement curve is then followed by an almost linear response once the contact between the flat punch and the sample surface is established (Fig. II-9a-e). It is to be noted that, in contrast to other samples, the force-displacement curve for the highly porous 8YSZ pillar presents some perturbations with small steps at constant load all along the loading (Fig. II-9f). This noise on the data is related to the very low force measured for this specific sample (the force is lower than 40 mN).

The Young's moduli of the porous 8YSZ pillars were estimated from the initial slope of the unloading curves. For this purpose, finite element simulations of the compression test were conducted assuming a pure elastic behavior with a Poisson's ratio fixed to 0.31 [103]. For this modeling, a 2D approach including the full geometry of the tapered pillar attached to a part of the pellet was adopted using axisymmetric conditions. The size of the simulated pellet substrate was chosen in such a way that the mechanical response of the pillar becomes independent of

boundary conditions applied at the bottom of the substrate (*i.e.* the displacements are blocked in the axial direction). As in the experiments, the imposed displacements were applied at the top of the pillar assuming a perfect sliding between the specimen and the flat punch. For these specific experiments (*i.e*. sample size and loading), it has been checked that the potential friction between the 8YSZ and the indenter does not change significantly the pillar mechanical response. This modeling has allowed identifying the Young's modulus by fitting the experimental data recorded during the early stage of the specimen unloading (Table II-2).

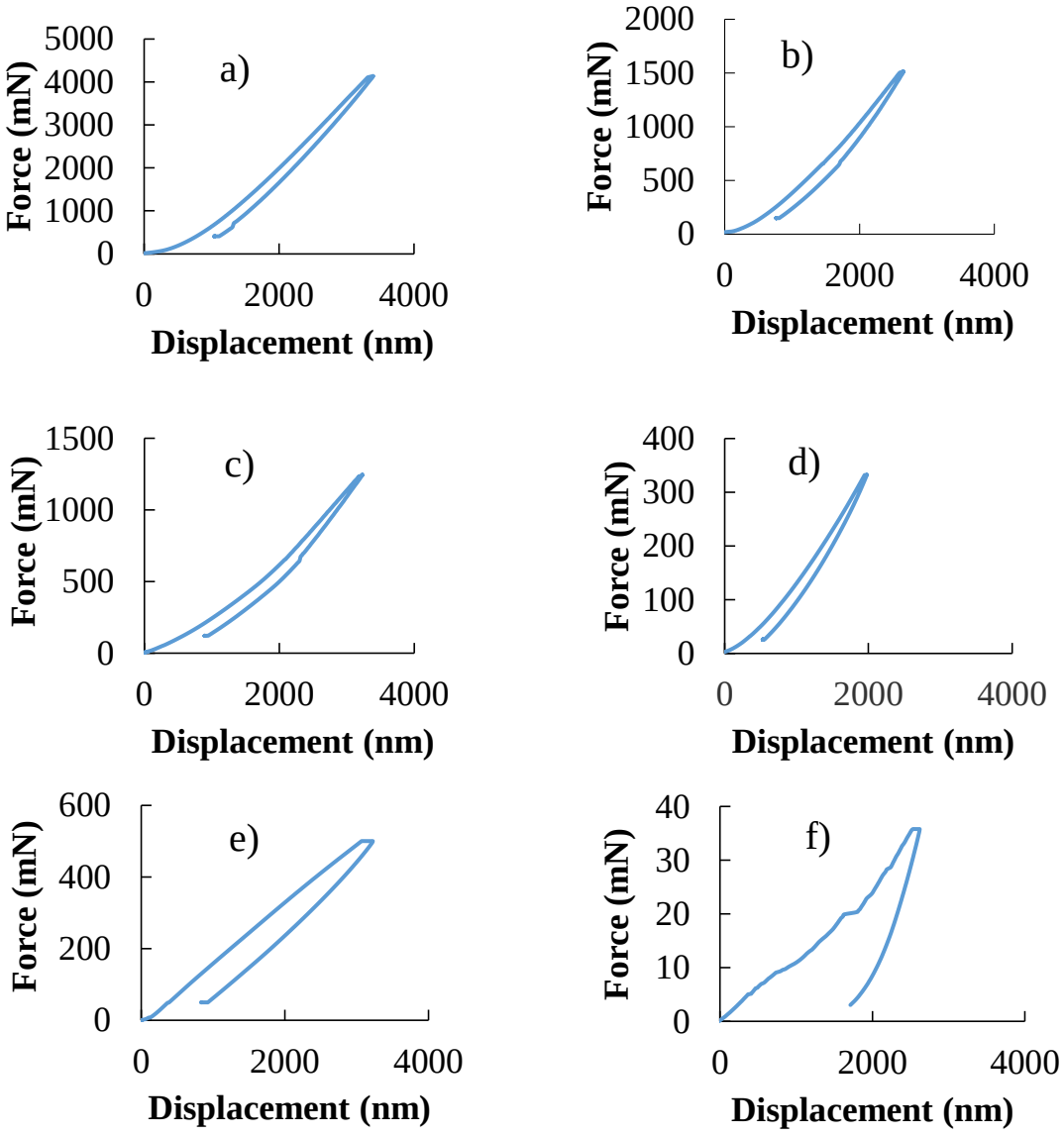

Fig II- 9. Load-displacement curves recorded for samples sintered at: a) 1270°C (porosity: 33%), b) 1230°C (36%), c) 1200°C (40%), d) 1150°C (49%) and highly porous specimens (63%) made of: e) 3YSZ, f) 8YSZ.

For each type of porous pillar, the mean slope from three tests was considered to take into account the scattering in the experimental measurements for the Young's modulus estimation. It must be noticed that the unloading curve was used as it is affected neither by the initial establishment of the contact nor by the small perturbations as noted in the loading curve.

The Young's modulus estimated by FE simulations of the experiments is plotted as function of the 8YSZ porosity in Fig. II-10. As expected, the Young's modulus E is found to be significantly decreased with increasing the porosity p. Moreover, the experimental data have been compared to the prediction of the so-called modified-exponential model (*i.e.* $E = E_0 \exp^{\left(\frac{-[E]\,p}{1-p}\right)}$ [132]), proposed for porous ceramics, considering a Young's modulus for dense 8YSZ E_0 of 216 GPa [103] and an intrinsic elastic modulus $[E]$ of 2.2 [132]. Without any fitting, it can be seen that the modified-exponential law is roughly in agreement with the measurements (Fig. II-10). Therefore, even if these experiments were mainly designed to study the fracture behavior of porous ceramics considering micro-samples, satisfactory estimation of the Young's modulus, in agreement with macro-scale testing, can also be made from the unloading curve of unbroken samples.

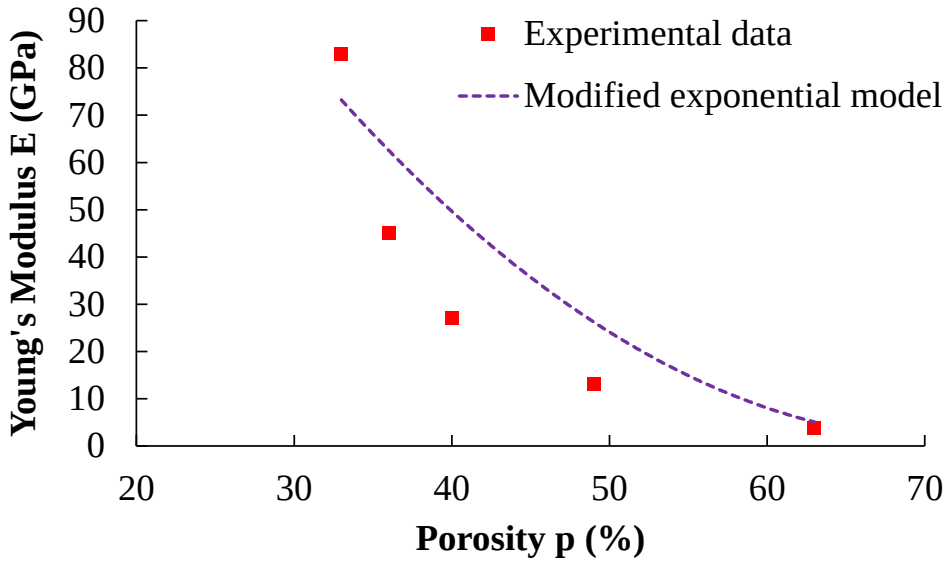

Fig II- 10. Young's modulus as a function of porosity for 8YSZ porous ceramics. Comparison with the modified exponential model proposed in [132] considering a Young's modulus of E_0 = 216 GPa for dense 8YSZ [103] and an intrinsic elastic modulus $[E]$ = 2.2 [132].

The second series of experiments were conducted on other pillars until their total collapse. Considering the initial geometry of the pillar (*i.e.* total height and top surface diameter),

engineering stress-strain data were calculated from the recorded load-displacement measurements. Examples of the typical stress-strain curves plotted until fracture are presented in Fig. II-11. As it can be seen in Fig. II-11a-d, the fracture occurs suddenly for the pillars with porosity ranging from 33 % to 49 %. No signs of damage are detected in the mechanical response before the total fracture, suggesting a pure brittle behavior of the 8YSZ ceramic at intermediate porosities. In Fig. II-11e-f, for the highly porous samples, a slight deviation in the slope just before failure is observed in the loading curve. This specific mechanical response obtained at the highest porosity (*i.e.* 63 %) could be an indicator of an internal damage starting before the total fracture. This observation thus suggests a change in the material fracture mode under uniaxial compression at high porosity.

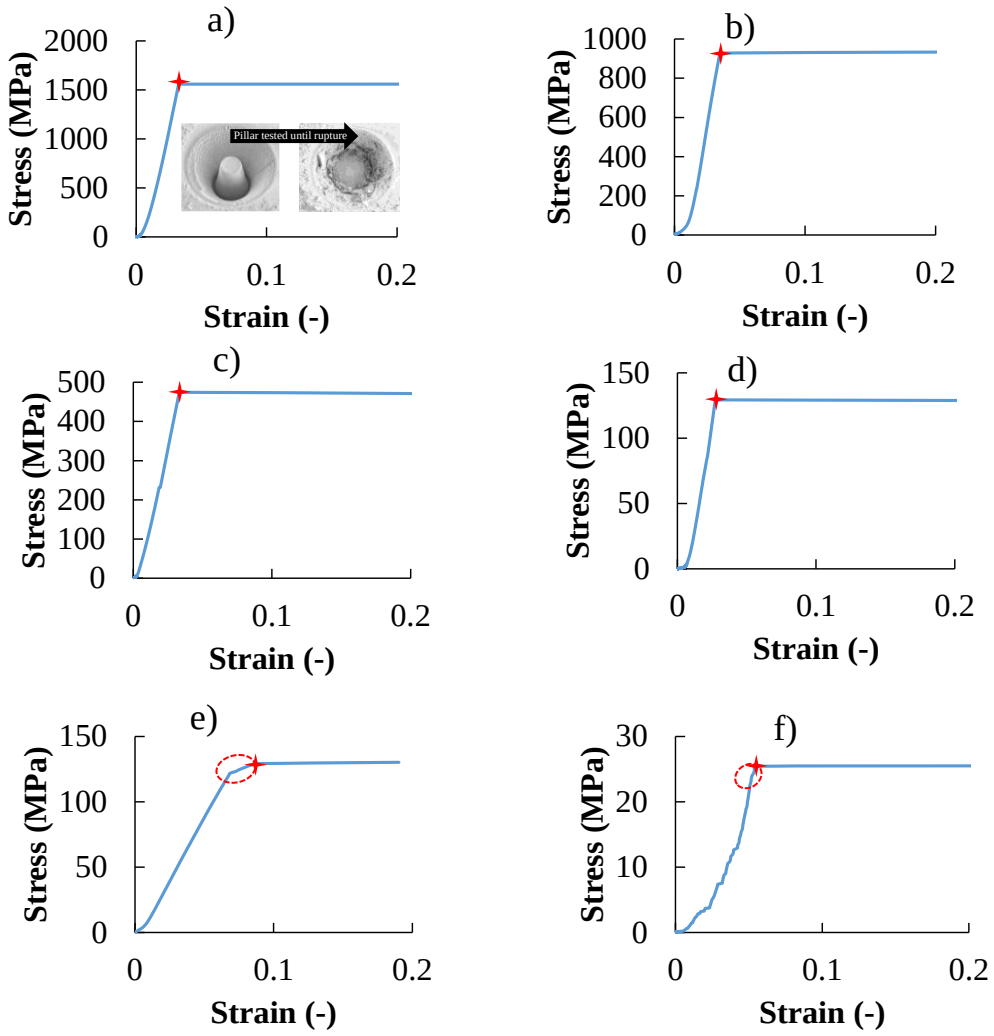

Fig II- 11. Stress-strain response for the 8YSZ micro-pillars sintered at: a) 1270°C (porosity: 33%), b) 1230°C (36%), c) 1200°C (40%), d) 1150°C (49%) and for the highly porous specimens (63%) made of: e) 3YSZ, f) 8YSZ. Fracture stress is marked with a star. The zone surrounded by the dashed line in e) and f) shows non-linearity in the stress strain curve before fracture.

For each investigated porosity and material, at least five pillars were tested to identify the compressive fracture strength and quantify the dispersion in the measurements. It is to be noted that the compressive fracture strength corresponds to the maximum strength measured just before the pillar collapse, marked by a star in Fig. II-11.

As reported in Table II-2, the standard deviation for the measured fracture strength does not exceed a few percent of the mean value. This data scatter is rather low for local measurements on micro porous samples. The evolution of the measured fracture strength is plotted as a function of the porosity in Fig. II-12 for the 8YSZ samples. It can be remarked that the compressive fracture strength is strongly decreased with increasing the porosity. Indeed, the fracture strength is divided by a factor of 58 when the porosity is increased from 33 % to 63 %. This evolution of the experimental data is well fitted by a power law equation as shown in Fig. II-12. This result is in good agreement with the strength-porosity dependence relations proposed in the literature from macro-scale measurements [70,133].

Finally, the fracture strength measured for the highly porous 3YSZ is found considerably higher than for 8YSZ at similar porosity. This difference is mainly due to the intrinsic fracture properties of each material, known to be larger in 3YSZ [16,68], as well as most probably the noticeable differences in microstructures (with the presence of macro-pores in the highly porous 8YSZ sample).

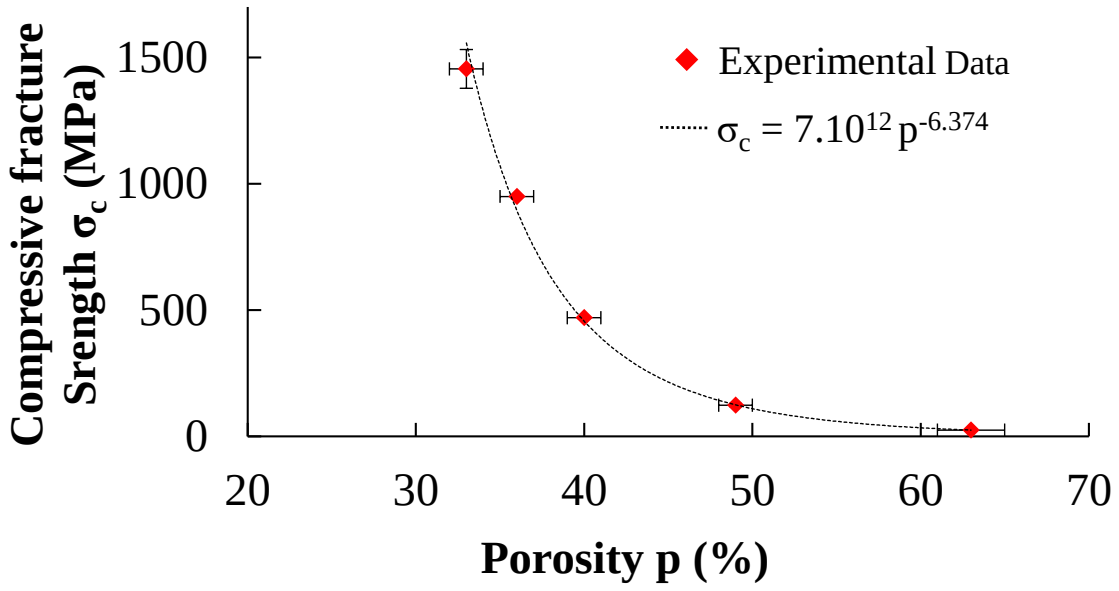

Fig II- 12. Compressive fracture strength as a function of porosity in 8YSZ ceramics, fitted by a power law model.

Table II- 2. Mechanical properties of the investigated samples under micro-compression testing.

Preparation method	Young's modulus [GPa]	Compressive fracture strength [MPa]
Partial sintering at 1270°C	83	1455 ± 77
Partial sintering at 1230°C	45	950 ± 5
Partial sintering at 1200°C	27	470 ± 4
Partial sintering at 1150°C	13	124 ± 6
Dissolution in nitric acid of Ni for 8YSZ cermet substrate	3.7	25 ± 3
Dissolution in nitric acid of Ni for 3YSZ cermet substrate	-	147 ± 22

II.2.4. Post-mortem characterizations

Pillars tested and unloaded before total fracture (first series of tests) were cross-sectioned and observed using FIB-SEM. Only the tests stopped at a loading slightly below the compressive fracture strength were selected to visualize the potential micro-cracks created in the pillars before their collapse. Since the transition from a damaged ceramic material to its totally broken state is very fast during our strain-controlled experiments, several calibration tests were required to be able to stop the loading just before the fracture. The resulting cracks within the 8YSZ sample sintered at 1270°C and the highly porous 8YSZ and 3YSZ specimens are shown in Fig. II-13-14.

As seen in Fig. II-13a-c for the lowest porosity (*i.e.* sample sintered at 1270°C), a large crack parallel to the loading direction is observed in the pillar before the total collapse (first series of experiments). The same fracture mode with very few large cracks parallel to the loading direction was observed for the samples sintered at 1230°C, 1200°C and 1150°C. Therefore, the 8YSZ material with porosities ranging from 33 % to 49 % is characterized by a brittle behavior as anticipated from the mechanical response during compression (*cf.* section II-2.3). These observations are in good agreement with the theoretical study [82] as well as with experimental results obtained on macro-samples of porous alumina [72].

According to the brittle behavior at intermediate porosity, the fracture onset must be controlled by the weakest local zones in the microstructure from which a large crack nucleates and propagates to the whole specimen. In porous materials subjected to compression, critical sites for cracks initiation are likely to be related to local microstructure characteristics (pore size,

orientation, ligament between two pores, etc.), leading to high local tensile stresses within the solid phase. The fracture triggers from one of these sites and then extends to the whole specimen [134]. Interestingly, despite the sensitivity of the compressive fracture strength to the first large crack nucleation, the experimental results were reproducible with a relative low scattering of the measurements. This could be explained by the homogeneity of the microstructure in the micro-pillar for the partially-sintered pellets with intermediate porosities.

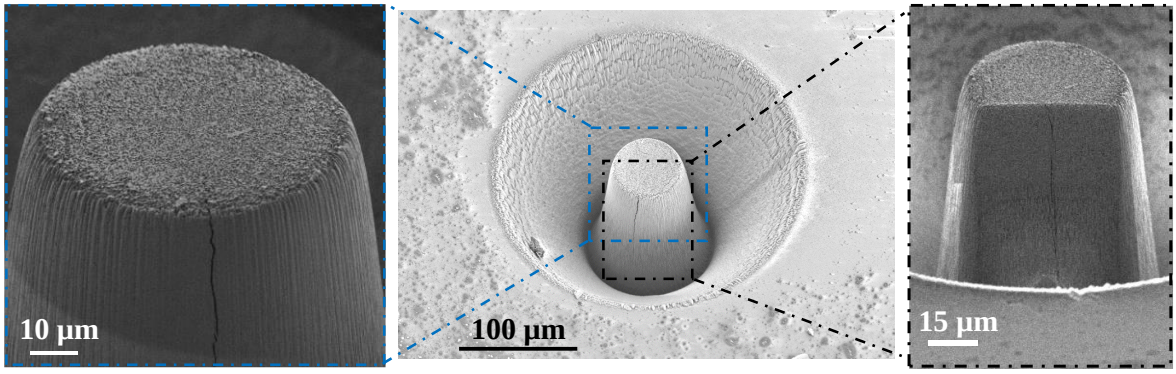

Fig II- 13. Ex-situ characterization after mechanical loading of the 8YSZ pillar sintered at 1270°C (porosity: 33%): a) SEM image of a longitudinal crack on the edge of the pillar, b) SEM image of the tested pillar, c) FIB-SEM cross section showing the large crack in the bulk of the pillar.

In contrast to the intermediate porosity case, the post-mortem characterizations of the highly porous 8YSZ pillars have revealed a distribution of micro-cracks in the microstructure. As shown in Fig. II-14a, the density of these micro-cracks is maximal in the upper part of the pillar where the compression is the highest (because of the tapered shape of the pillar as discussed in section II-1.1.3). These observations clearly indicate a different mechanism of fracture from the one at intermediate porosities. Indeed, for the highly porous sample, a local damage is induced in the material before the total fracture of the specimen. This internal damage explains the non-linear response, which is observed on the stress-strain response before the pillar fracture (Fig. II-11f). It is worth noting that this result is in good agreement with the work of Meille et al. dedicated to highly porous alumina samples tested in compression at macroscopic scale [72]. Indeed, as shown in Fig. II-14a, the authors had also observed a distribution of micro-cracks related to the local fracture of the solid walls between pores. The generation of these stable micro-cracks is also linked to local concentration of high tensile stresses in the solid phase. Then, the diffuse damage within the microstructure progressively increases until the final fracture of the material. Because of this damageable fracture mode, the fracture strength in

compression should not be controlled by the first crack initiation event. Therefore, since the total fracture is not sensitive to the weakest zone in the microstructure, the limited dispersion of the compressive fracture strength measurements must be mainly ascribed to the specific fracture mechanism based on progressive damage upon loading. A similar damage behavior has been also noted for the highly porous 3YSZ sample. Indeed, as shown in (Fig. II-14b), a network of micro-cracks between pores are also observed in the upper part of the specimen. As for the highly porous 8YSZ, this internal damage arising before the total fracture is consistent with the non-linear response of the stress-strain curve (Fig. II-11e). Therefore, despite the difference in mechanical properties with 8YSZ, the fracture mechanism of the highly porous 3YSZ is also governed by the generation of stable micro-cracks in the microstructure.

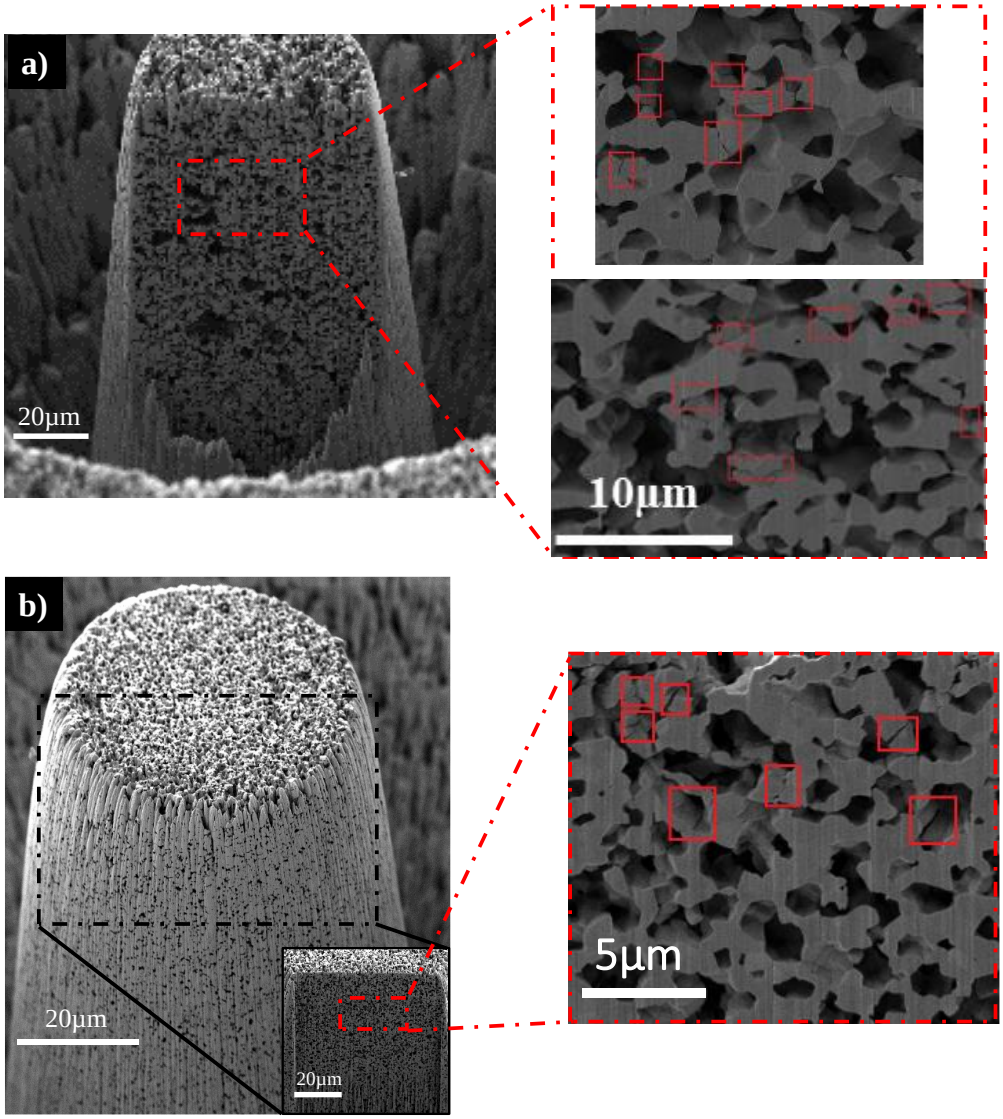

Fig II- 14. Ex-situ characterization of the highly porous (porosity: 63%) pillars after the mechanical loading with a zoom showing micro-cracks in the bulk of the pillar (highlighted by red rectangles): a) 8YSZ, b) 3YSZ. The tests were stopped before the fracture.

A transition in the fracture mode has been highlighted from a brittle behavior with large cracks at porosities below 50 %, towards local damaging with micro-cracks at high porosity, similarly to the one observed on porous alumina on macro-samples [72]. This change in mechanism could be controlled by the stored elastic energy, which decreases with increasing the pore volume fraction. A larger amount of available elastic energy favors the instable propagation of long cracks as noted at intermediate porosities. Nevertheless, further studies are still required to better understand this transition. From this point of view, the mechanical modeling of the 3D microstructure could be a relevant tool to analyze the fracture behavior of these porous ceramics [134].

II.2.5. Sample size effect

The compressive fracture strength measured in the present work on 8YSZ micro-pillars at a porosity of 63 % (*i.e.* 25 ± 3 MPa) is in good agreement with the data available in the literature obtained on macroscopic samples of 8YSZ at a porosity of 65 % (*i.e.* 27 MPa) [41,105]. It can be thus deduced that the compressive fracture properties for the highly porous 8YSZ do not depend on the size of the tested specimen. The uniaxial compressive loading and the high porosity fraction could explain this statement. Indeed, at this porosity level, a local damage by the creation of micro-cracks is observed under compression. Solid walls between pores subjected to the highest tensile stress are broken first. Due to the low stored elastic energy, the fracture remains local and does not lead to the propagation of large cracks. The diffuse damage within the microstructure then progressively increases up to the density threshold leading to the total collapse of the material. In other words, at high porosity, the compressive fracture strength level is controlled by the density of the micro-cracks created in the specimen thus explaining the absence of a sample size effect as noted in this work.

For highly porous 3YSZ material, the sample size effect is expected to be also absent but cannot be confirmed due to the lack of measurement on macroscopic specimen. Moreover, when the fracture mechanism is controlled by a pure brittle behavior at intermediate porosities, the available data at the macroscopic scale is not yet sufficient to precisely evaluate the sample size effect on the compressive fracture strength. Therefore, further investigations at porosities below 50 % are still required.

II.3. Conclusion

In this chapter, a dedicated protocol has been proposed for the testing of porous ceramics with microstructures averaging the contribution of porous and solid phases in 10-100 µm length scale, starting from micro-compression specimen fabrication and testing up to post-mortem characterizations. This original methodology has been applied to measure the fracture properties of porous Yttria-Stabilized Zirconia tested under micro-compression. The specimen for the experiments were prepared using Xe^+ pFIB, which enabled to mill into porous YSZ pellets suitable micro-pillars with a typical diameter of 60 µm. The homogeneity of the porous microstructures was estimated by measuring relevant microstructural characteristics on cross-sections and 3D reconstructions obtained by electron and X-ray microscopy.

The Young's modulus was estimated from the unloading curves of pillars tested before failure and the compressive fracture strength was measured on pillars tested until the total fracture. These properties were determined for the 8YSZ material over a large range of porosities (33 % to 63 %) and for the 3YSZ ceramic at high porosity (63 %). All the experiments were reproducible with a rather limited data scattering. A substantial decrease was found for the compressive fracture strength when increasing the porosity. Pillars tested and unloaded just before the total failure were also cross-sectioned by FIB-SEM to support the analysis of mechanical failure behavior. A transition from a brittle behavior to a damage fracture mode was highlighted when increasing the porosity. Indeed, large cracks parallel to the direction of solicitation were observed at porosities below 50 % while diffuse damage with micro-cracks was detected within the highly porous 3YSZ and 8YSZ samples at 63 %.

The measured YSZ fracture properties along with the change in the fracture mode with porosity have been used to support and validate the model developments. Nevertheless, a relevant choice of numerical framework adapted to the case of complex real porous microstructure is needed before. This is the focus of the next chapter where the choice of the numerical approach is presented, its implementation detailed and the capacity of the method to accurately predict the fracture discussed based on theoretical considerations. The thorough presentation and discussion of the validation then follows in chapter four.

III. Numerical approach to simulate the fracture in porous ceramic microstructures: the Phase-Field method

Because of the complexity of porous ceramic microstructures, the mechanical behavior and especially the fracture cannot be investigated efficiently and in full details based only on experimental studies. Indeed, it has been shown that the mechanical response of porous ceramics is strongly dependent on the microstructure [67–70,74–76]. Therefore, an analysis with a pure experimental method would require an unlimited number of mechanical characterizations. From this point of view, a numerical approach is well adapted to better understand the precise role of the microstructure by providing accurate predictions of crack initiation and propagation in porous ceramics.

As shown in the literature review presented in the first chapter, the proposed models considering simplified microstructures fail to quantitively reproduce the measurements [87,88,97]. Therefore, it is of central importance to propose predictive models that can take into account

the real morphology of porous ceramics microstructures. To the best of our knowledge, studies carried out on real 3D porous ceramic microstructures with experimental validation have not yet been reported. Moreover, the literature review in chapter one has highlighted that the local criterion that must be applied to simulate the fracture in porous ceramics is in particular still not well identified. However, as discussed in the work of Leguillon et al. [67], it can be expected that the crack initiation should be controlled by a coupled stress-energy criterion. Therefore, the reliable modeling of crack initiation, propagation and branching formulated using a relevant mixed energy-stress criterion is still required. Furthermore, because of the local heterogeneities in real 3D porous ceramic microstructures, the appropriate numerical approach must be easily implemented without too complex numerical manipulation to identify the zone where the crack initiates and to simulate its propagation. Because of all these constrains, a model based on a damage variable [80,135] for describing the crack seems to be well adapted as it does not require strategies for automated modifications of the mesh during the simulation of the fracture.

Accordingly, the objective of this work consisted in the development of a model for real 3D porous ceramic microstructures that is able to consider an energy-stress criterion. For this purpose, the so-called phase-field method (PFM) [136] has been adopted. The relevance of the choice of the phase-field approach to simulate the crack initiation and propagation in such complex materials is addressed in this chapter based on theoretical considerations. Firstly, a brief review of the different numerical approaches for fracture in the frame of the Finite Element Method (FEM) is given. Then, the controversy in the literature on the capacity of the phase-field method to accurately predict the crack nucleation is reported. Subsequently, the theoretical development of the phase-field method in this thesis is presented. Afterwards, the PFM model implementation is detailed with a numerical validation based on the benchmark configurations reported in the work of Miehe et al. [136]. Finally, the evaluation of the capacity of the PFM approach to accurately predict the fracture initiation is performed based on the comparison with the results obtained by the coupled criterion [85] on ideal geometries.

III.1. State of the art

III.1.1. Brief review on numerical approaches for fracture

In order to study the fracture initiation, propagation and branching, several numerical methods based on the explicit simulation of cracks have been developed. Two main computational

families exist in the frame of the FEM depending on the sharp or diffuse description of the simulated crack.

The first numerical approach is referred to as the discrete crack model. In this case, the sharp crack is introduced as a discontinuity in the mesh and its propagation is simulated using various numerical methods such as the extended finite element method (XFEM) [137], the phantom-node method, the element-erosion method, the generalized finite element method (GFEM) or re-meshing techniques [138–141]. The implementation of discrete crack models requires criteria for crack initiation and propagation. These criteria come from the Linear Elastic Fracture Mechanics (LEFM), which is well appropriate to describe the brittle behavior of ceramic materials (*i.e.* stress criterion, energy criterion or coupled stress-energy criterion). However, the numerical implementation of discrete crack models is typically difficult since the fracture criterion must be evaluated on the whole structure in order to identify the sites for the crack nucleation. Furthermore, special algorithms are required to introduce discontinuities by modifying locally the shape functions or by re-meshing the path for the propagation. For all these reasons, discrete crack models are not well adapted to simulate complex cases like the branching and multiple cracks problem. Therefore, their application to porous ceramics with complex and heterogeneous microstructures can be anticipated inefficient.

In order to overcome the limitations inherent to the discrete approach, several models have been proposed in the frame of the continuous fracture mechanics theory. All are based on a 'diffuse' or 'smeared' description of the discontinuity where the crack is implicitly modeled through a smooth scalar damage variable. In this context, Marigo and coauthors have proposed for the development of these models a rigorous theoretical framework using the variational approach and the gamma-convergence theory for the regularization of the free-discontinuity medium [142–145]. As a result, the fracture problem has been reformulated as the minimization of an energy functional without any additional criterion. On the basis of these developments, Miehe et al. [136,146] have proposed a specific smeared crack model referred to as the Phase-Field Method (PFM) for fracture mechanics. Thanks to the thermodynamic consistency of this model, a staggered scheme has been proposed for the numerical resolution [136], allowing a simple implementation in FEM codes [138,141,147,148]. The crack extension is governed by an energy driving force that can be interpreted as a Griffith criterion. Several studies have shown that the model is able to simulate accurately the propagation, the branching and the multi-cracking problem in complex geometry [139,141]. For example, Nguyen et al. [135] have successfully simulated the cracks evolution in a lightweight concrete microstructure with

encapsulated pores. For all these reasons, the PFM seems suitable to study the fracture in porous ceramics.

III.1.2. Controversy on the capacity of the Phase-Field method to accurately predict the crack initiation

In the formulation of the phase-field method, a regularization length scale parameter, denoted ℓ, is introduced to control the width of the smeared crack (cf. section III.2). Therefore, because of the dependency of the PFM approach on this parameter, a controversy on its capacity to accurately predict the crack initiation arose in the community.

On the one hand, Amor et al. [149] have suggested that the PFM approach can predict the crack initiation by choosing an ad-hoc value for the length scale parameter ℓ. Indeed, they have proposed to relate this regularization length for the phase-field method to the Irwin characteristic length linked to the material properties, *i.e.*, strength and toughness. For this purpose, they have derived an expression of ℓ considering a one-dimensional traction test [149,150]. It can be noticed that some authors have successfully tested the relevance of this approach to simulate the crack nucleation for simplified geometries [139,151]. Besides, Molnár et al. [152] have recently proposed a generalization of the expression derived by Amor and co-workers for the 2D case, still considering a homogeneous phase-field. They have found that the length scale parameter must be also a function of the ratio of the principal stresses suggesting a dependence to the local geometry where the crack nucleates. However, the generalization and the relevance of these expressions for complex 3D geometries without neglecting the gradient term in the phase-field is still questionable.

On the other hand, Kumar et al. [153] have recently criticized the above interpretation of ℓ as a material constant. They have claimed that 'the fracture nucleation cannot be properly modelled by the phase-field formulation' since 'it is purely energetic' and does not take into account the material fracture strength. In this view, the regularization length is presented as a numerical 'parameter that is void of any further physical meaning'. To overcome this difficulty, they have proposed to add an external driving force to the classical formulation depending on the material strength and supplementary numerical correction factors [153].

The recent literature mentioned above indicates that the interpretation of the regularization length scale parameter ℓ and the use of the PFM to accurately simulate the crack nucleation is still a subject of investigation.

To advance the field, the comparison of the PFM results with the predictions of the well-established coupled criterion [85] on ideal geometries appears as an appropriate approach to unravel the nature of ℓ and assess the capacity of the PFM model to accurately simulate the crack nucleation.

III.2. PFM model description

The PFM approach described in Miehe et al. [136,146] has been adopted in this work. The model has been built considering quasi-static and isothermal conditions with the assumption of small strain. The variables of the problem are time dependent because the damage evolves during the loading. Nevertheless, the time step t is not 'real' and is introduced only through the loading increment in the simulation. Hereafter, the studied domain and the position are denoted V and $\overline{\boldsymbol{x}}$, respectively.

The crack is modelled through a smooth scalar damage variable $d(\overline{\boldsymbol{x}})$ referred to as the phase-field. Besides, a regularization length scale parameter ℓ has been introduced to control the region of transition from the pristine state ($d(\overline{\boldsymbol{x}}) = 0$) to the fully broken state ($d(\overline{\boldsymbol{x}}) = 1$) (Fig. III-1). In order to propose a specific expression for the smeared crack surface $\Gamma_\ell(d)$, depending on the damage variable, Miehe et al. [136] have assumed that the evolution of the damage in one-dimension can be approximated by an exponential function $d(x) = e^{-\frac{|x|}{\ell}}$. This hypothesis has allowed expressing $\Gamma_\ell(d)$ in 1D, which has been directly extended to the three-dimensional case as follows:

$$\Gamma_\ell(d) = \frac{1}{2\ell}\int_{\mathrm{V}} d^2 + \ell^2 \overline{\nabla} d \cdot \overline{\nabla} d \, d\mathrm{V} \text{ with } \mathrm{V} \subset R^\delta, \delta \in [1,2,3] \qquad \text{(III-1)}$$

It is worth noting that the minimization of the functional Γ_ℓ provides an approximation of the phase-field $d(\overline{\boldsymbol{x}})$, which is a solution of the associated Euler-Lagrange type equation:

$$d - \ell^2 \Delta d = 0 \text{ in V with } \overline{\nabla} d \,.\, \overline{\mathbf{n}} = 0 \text{ on } \partial \mathrm{V} \qquad \text{(III-2)}$$

where $\overline{\mathbf{n}}$ is the outward normal on ∂V considering the natural boundary conditions.

The PFM formulation is mainly based on an energy balance. Indeed, the evolution of the potential energy during the loading $\dot{\pi}$ is the sum of three contributions, namely the rate of the

stored elastic energy $\dot{E}_s$, the rate of the work of the external forces $\dot{P}_c$ and the energy dissipation rate $\dot{W}_c$ due to crack propagation:

$$\dot{\pi} = \dot{E}_s + \dot{W}_c - \dot{P}_c \tag{III-3}$$

where the symbol $\dot{X}$ denotes the time derivative of X.

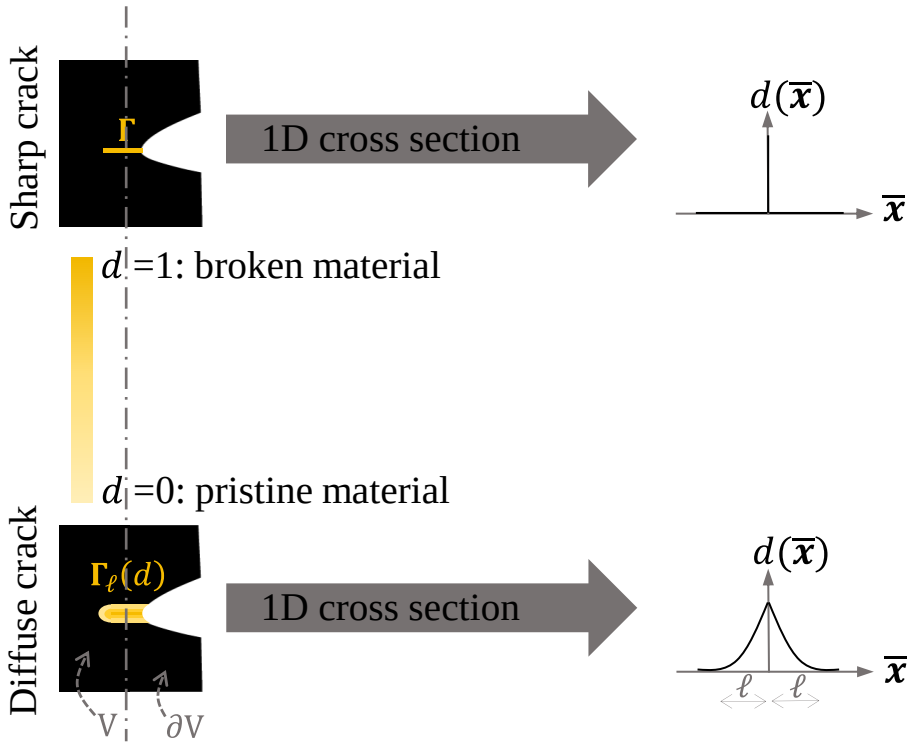

Fig III- 1. Sharp and diffuse crack description.

• The last term of this equation is classically expressed through the displacement field $\overline{\boldsymbol{u}}$ and the applied force $\bar{\boldsymbol{t}}$ on the edge of the domain:

$$\dot{P}_c = \int_{\partial V} \bar{\boldsymbol{t}} . \dot{\overline{\boldsymbol{u}}}\, ds \tag{III-4}$$

• The energy dissipation rate ascribed to the evolution of the damage can be expressed as the rate of the work W_c required to create a diffuse crack in the volume:

$$W_c = \mathrm{G}_c \Gamma_\ell(d) \text{ and } \dot{W}_c = \mathrm{G}_c \frac{d\Gamma_\ell(d)}{dt} = \mathrm{G}_c \int_V \left(\frac{1}{\ell} d - \ell \Delta d\right) \dot{d}\, d\mathrm{V} \tag{III-5}$$

Where G_c is the critical energy release rate of the material.

• The rate of stored energy is expressed by the integral of the density of elastic strain energy Ψ:

$$\dot{E}_s = \int_V \dot{\Psi} dV \tag{III-6}$$

In the implemented model, it is assumed that the crack cannot propagate under compression. To fulfil this requirement, a spectral decomposition of the strain tensor $\bar{\bar{\boldsymbol{\varepsilon}}}$ is carried out and the density of the strain energy is split into a sum of two contributions Ψ^+ and Ψ^-, related to tension and compression, respectively:

$$\Psi = (g(d) + \alpha)\Psi^+ + \Psi^- \tag{III-7}$$

Where $g(d)$ is a degradation function introduced to take into account the material softening during damage. Among several options [154], $g(d)$ is chosen, in this work, as a quadratic function with $g(d) = (1-d)^2$. It can be noticed that the numerical parameter α, which is assigned a very low positive value, is added to ensure the stability of the simulation when d tends to 1. Therefore, this numerical parameter can be interpreted as an artificial residual stiffness when the material is totally broken (d = 1).

To express Ψ^+ and Ψ^- in Eq. III-7, the strain tensor must be split into a sum of positive $\bar{\bar{\boldsymbol{\varepsilon}}}_+$ and negative $\bar{\bar{\boldsymbol{\varepsilon}}}_-$ principal strain which correspond to the tensile and the compressive mode, respectively. For this purpose, let us remind that the spectral decomposition of the elastic strain tensor is expressed as: $\bar{\bar{\boldsymbol{\varepsilon}}} = \sum_{i=1}^{3} \langle \bar{\bar{\boldsymbol{\varepsilon}}}^i \rangle \, \bar{\boldsymbol{n}}^i \times \bar{\boldsymbol{n}}^i$ where $\bar{\bar{\boldsymbol{\varepsilon}}}^i$ is the principal strain and $\bar{\boldsymbol{n}}^i$ is the principal strain direction with $i \in [1,2,3]$. Therefore, the decomposition of the strain tensor is given by:

$$\bar{\bar{\boldsymbol{\varepsilon}}} = \bar{\bar{\boldsymbol{\varepsilon}}}_+ + \bar{\bar{\boldsymbol{\varepsilon}}}_- \tag{III-8}$$

$$\text{with } \bar{\bar{\boldsymbol{\varepsilon}}}_\pm = \sum_{i=1}^{3} \langle \bar{\bar{\boldsymbol{\varepsilon}}}^i \rangle_\pm \bar{\boldsymbol{n}}^i \times \bar{\boldsymbol{n}}^i \tag{III-9}$$

Using these relations, the two contributions of the elastic strain energy are written as follows:

$$\Psi^\pm = \mu \, \langle \bar{\bar{\boldsymbol{\varepsilon}}} \rangle_\pm : \langle \bar{\bar{\boldsymbol{\varepsilon}}} \rangle_\pm + \frac{\lambda}{2} \langle tr(\bar{\bar{\boldsymbol{\varepsilon}}}) \rangle_\pm^2 \tag{III-10}$$

Where μ and λ are the Lamé constants for an isotropic elastic material

Thanks to the introduction of the degradation function in the formulation of the density of the strain energy (Eq. III-7), the stress tensor $\overline{\overline{\boldsymbol{\sigma}}}$ is dependent on the damage field $d(\overline{\boldsymbol{x}})$ as follows:

$$\overline{\overline{\boldsymbol{\sigma}}}(\overline{\overline{\boldsymbol{\varepsilon}}}, d) = \frac{\partial \Psi(\overline{\overline{\boldsymbol{\varepsilon}}}, d)}{\partial \overline{\overline{\boldsymbol{\varepsilon}}}} \tag{III-11}$$

Besides, the thermodynamic driving force f for crack extension is expressed in the PFM model as the derivative of the elastic strain energy stored in the material with respect to the damage field:

$$f = -\frac{\partial \Psi(\overline{\overline{\boldsymbol{\varepsilon}}}, d)}{\partial d} = 2(1-d)\Psi^{+} \tag{III-12}$$

In this condition, the driving force is controlled by the part of the strain energy due to the tension. Finally, the rate of the stored energy can be written as follows:

$$\dot{E}_s = \int_V \left[\overline{\overline{\boldsymbol{\sigma}}} : \left\{ \frac{1}{2} \left(\overline{\nabla} \dot{\overline{\boldsymbol{u}}} + \overline{\nabla}^T \dot{\overline{\boldsymbol{u}}} \right) \right\} - f \dot{d} \right] dV \tag{III-13}$$

The governing equation to solve the problem is given by the rate of the potential energy Eq. (III-6) combined with Eqs. (III-4), (III-5) and (III-13). For each increment of loading (or time), the minimization of this energy functional must be carried out on each variable d and $\overline{\boldsymbol{u}}$. In a staggered approach for the resolution, the minimization at a frozen damage state for the phase-field (*i.e.* $d(\overline{\boldsymbol{x}}) = \text{cte}$) leads to solve a 'classical' elastic problem:

$$\overline{\nabla} \cdot \overline{\overline{\boldsymbol{\sigma}}}(\overline{\overline{\boldsymbol{\varepsilon}}}, d) = 0 \text{ for the domain } V \text{ with } \overline{\overline{\boldsymbol{\sigma}}} . \overline{\boldsymbol{n}} = \overline{\boldsymbol{t}} \quad on\ \partial V \tag{III-14}$$

Then, the resolution at a given loading (*i.e.* $\overline{\boldsymbol{u}} = cte$) yields the equation for the phase field computation when the crack propagates with $\dot{d} > 0$:

$$f = 2(1-d)\Psi^{+} = \mathrm{G}_c \left(\frac{1}{\ell} d - \ell \Delta d \right) \text{ with } \overline{\nabla} d \,.\, \overline{\mathbf{n}} = 0 \text{ on } \partial \mathrm{V} \tag{III-15}$$

It can be noticed that Eq. (III-15) expresses a 'classical' energy criterion. Indeed, the crack is assumed to propagate when the driving force equivalent to an energy release rate in $\mathrm{J \cdot m^{-3}}$ is equal to the density of energy created in the domain by the apparition of the cracked surface. Moreover, the creation of cracks is an irreversible process, so that the phase-field $d(\overline{\boldsymbol{x}})$ cannot decrease during the loading. To take into account this supplementary constrain, Miehe et al. [136] have proposed to introduce in Eq. (III-15) an 'history' loading field $\mathcal{H}(\overline{\boldsymbol{x}}, t)$ stipulating

that Ψ^+ can only increase over the time. The partial differential Eq. (III-15) is thus rewritten as follows:

$$2(1-d)\mathcal{H} = \mathrm{G}_c\left(\frac{d}{\ell} - \ell\Delta d\right) \quad \text{with } \mathcal{H}(\bar{\boldsymbol{x}},t) = \max_{s\in[0,t]} \Psi^+(\overline{\boldsymbol{u}}(\bar{\boldsymbol{x}},t)) \tag{III-16}$$

III.3. PFM implementation

In the PFM approach, the fracture problem is described through a system of partial differential equations without any additional criterion. As presented in section III.2, the theoretical development of the phase-field method allows to establish the strong form of the governing equations (*i.e.* Eq. (III-14) and Eq. (III-16) for the mechanical and phase-field problem, respectively).

Considering the test functions $\delta\overline{\boldsymbol{u}}$ and δd, their weak forms are expressed as follows:

$$\int_V \bar{\bar{\boldsymbol{\sigma}}} : \delta\bar{\bar{\boldsymbol{\varepsilon}}}\, dV - \int_{\partial V} \bar{\boldsymbol{t}}\,.\,\delta\overline{\boldsymbol{u}}\, ds = 0 \tag{III-17}$$

$$\int_V -2(1-d)\,\mathcal{H}\,\delta d\, dV + \int_V \mathrm{G}_c\left(\ell\bar{\nabla}d.\bar{\nabla}\delta d + \frac{1}{\ell}\, d\,\delta d\right) dV = 0 \tag{III- 18}$$

In the frame of the finite element method, the discretization in space using the classical matrix-vector notation yields:

$$\overline{\boldsymbol{u}} = N_u\widehat{\overline{\boldsymbol{u}}},\ d = N_d\hat{d} \tag{III- 19}$$

$$\delta\overline{\boldsymbol{u}} = N_u\widehat{\delta\overline{\boldsymbol{u}}},\ \delta d = N_d\widehat{\delta d} \tag{III-20}$$

$$\bar{\bar{\boldsymbol{\varepsilon}}} = B_u\widehat{\overline{\boldsymbol{u}}},\ \nabla d = B_d\hat{d} \tag{III-21}$$

$$\delta\bar{\bar{\boldsymbol{\varepsilon}}} = B_u\widehat{\delta\overline{\boldsymbol{u}}},\ \nabla\delta d = B_d\widehat{\delta d} \tag{III-22}$$

Where $\widehat{\overline{\boldsymbol{u}}}$, $\widehat{\delta\overline{\boldsymbol{u}}}$, $\hat{d}$ and $\widehat{\delta d}$ are the vectors of nodes. The matrices N_u and N_d denote the shape functions while B_u and B_d are the derivatives of the shape functions.

Adopting these notations, the weak forms of the governing equations are thus rewritten as follows:

$$(\delta\overline{\boldsymbol{u}})^{\mathrm{T}}\int_V B_u^{\mathrm{T}}\,\mathfrak{D}\,B_u\, dV\,\overline{\boldsymbol{u}} - (\delta\overline{\boldsymbol{u}})^{\mathrm{T}}\int_{\partial V} N_u^{\mathrm{T}}\,\bar{\boldsymbol{t}}\, ds = 0 \tag{III- 23}$$

$$\left(\widehat{\delta d}\right)^{\mathrm{T}}\int_V 2\,\mathcal{H}\,N_d^{\mathrm{T}}\, dV - \left(\widehat{\delta d}\right)^{\mathrm{T}}\int_V B_d^{\mathrm{T}}\,\mathrm{G}_c\ell\,B_d + N_d^{\mathrm{T}}\left(\frac{\mathrm{G}_c}{\ell} + 2\,\mathcal{H}\right)N_d\, dV\,\hat{d} = 0 \tag{III- 24}$$

As presented in the work of Zhou et al. [148], the weak form of the mechanical problem (Eq. (III- 23)) allows to formulate the stiffness matrix, denoted herein $\mathfrak{D}$, as a function of the damage variable d. Thanks to the symmetry of the elasticity tensor (denoted $\mathfrak{E}$), $\mathfrak{D}$ is calculated as follows:

$$\mathfrak{D} = \begin{pmatrix} \mathfrak{E}_{1111} & \mathfrak{E}_{1122} & \mathfrak{E}_{1133} & \mathfrak{E}_{1112} & \mathfrak{E}_{1123} & \mathfrak{E}_{1113} \\ \mathfrak{E}_{1122} & \mathfrak{E}_{2222} & \mathfrak{E}_{2233} & \mathfrak{E}_{2212} & \mathfrak{E}_{2223} & \mathfrak{E}_{2213} \\ \mathfrak{E}_{1133} & \mathfrak{E}_{2233} & \mathfrak{E}_{3333} & \mathfrak{E}_{3312} & \mathfrak{E}_{3323} & \mathfrak{E}_{3313} \\ \mathfrak{E}_{1112} & \mathfrak{E}_{2212} & \mathfrak{E}_{3312} & \mathfrak{E}_{1212} & \mathfrak{E}_{1223} & \mathfrak{E}_{1213} \\ \mathfrak{E}_{1123} & \mathfrak{E}_{2223} & \mathfrak{E}_{3323} & \mathfrak{E}_{1223} & \mathfrak{E}_{2323} & \mathfrak{E}_{2313} \\ \mathfrak{E}_{1113} & \mathfrak{E}_{2213} & \mathfrak{E}_{3313} & \mathfrak{E}_{1213} & \mathfrak{E}_{2313} & \mathfrak{E}_{1313} \end{pmatrix} \quad \text{(III-25)}$$

It is to be noted that the fourth order elasticity tensor $\mathfrak{E}$ depends on the phase-field variable as follows:

$$\mathfrak{E} = \frac{\partial \bar{\bar{\boldsymbol{\sigma}}}(\bar{\bar{\boldsymbol{\varepsilon}}}, d)}{\partial \bar{\bar{\boldsymbol{\varepsilon}}}} = \lambda \left\{ \left[(1-d)^2 + \alpha \right] \mathbf{H}_{\boldsymbol{\varepsilon}}\left(tr(\bar{\bar{\boldsymbol{\varepsilon}}})\right) + \mathbf{H}_{\boldsymbol{\varepsilon}}\left(-tr(\bar{\bar{\boldsymbol{\varepsilon}}})\right) \right\} \mathrm{J} + 2\mu \left\{ \left[(1-d)^2 + \alpha \right] \boldsymbol{P}^{+} + \boldsymbol{P}^{-} \right\} \quad \text{(III-26)}$$

Where $\mathbf{H}_{\boldsymbol{\varepsilon}}$ is the Heaviside function and J is the Kronecker tensor $\left(\mathrm{J}_{ijkl} = \delta_{ij}\delta_{kl}\right)$. The fourth order tensors $\boldsymbol{P}^{+}$ and $\boldsymbol{P}^{-}$ are given by: $\boldsymbol{P}^{\pm}_{ijkl} = \sum_{a=1}^{3}\sum_{b=1}^{3} \mathbf{H}_{\varepsilon}(\varepsilon_a)\delta_{ab} n_{ai} n_{aj} n_{bk} n_{bl} + \sum_{a=1}^{3}\sum_{b\neq a}^{3} \frac{1}{2} \frac{\langle \varepsilon_a \rangle_{\pm} - \langle \varepsilon_b \rangle_{\pm}}{\varepsilon_a - \varepsilon_b} n_{al} n_{bj} (n_{ak} n_{bl} + n_{bk} n_{al})$ [148].

The nonlinearity of the stress-strain response and the material anisotropic behavior induced by the introduction of $g(d)$in III-7 are thus taken into account through the stiffness matrix $\mathfrak{D}$.

Finally, the implementation of the Phase-Field method has been performed in Comsol Multiphysics® considering the strong form of the governing equations (*i.e.* Eq. (III-14) and Eq. (III-16)) along with the stiffness matrix $\mathfrak{D}$. The mechanical, phase-field and history field problems were solved using the Solid Mechanics module, Helmholtz equation and Ordinary Differential equation proposed in Comsol Multiphysics ®, respectively.

III.4. Numerical validation of the PFM implementation

The validation of the Phase-Field method implementation has been carried out by referring to the benchmark configuration of single edge notched sample reported in the work of Miehe et al. [136]. For this purpose, the geometry, material properties and loadings used by Miehe et al. [136] have been considered. The geometry was fixed to a square of 1 mm in length with a single edge notch of 0.5 mm (Fig. III-2). The assigned material properties were G_c = 2.7 10^{-3} kN/mm

($2.7\ 10^3$ J/m^2) for the fracture toughness, λ = 121.15 kN/mm^2 (121.15 GPa) for the elastic bulk modulus and μ = 80.77 kN/mm^2 (80.77 GPa) for the shear modulus. The mesh was constructed using quadrilateral elements. The cases of shear and traction were both investigated. The 2D simulations were performed in displacement controlled loading mode with the plane strain assumption. Two values for the regularization parameter ℓ_1= 0.015 mm and ℓ_2= 0.0075 mm have been considered.

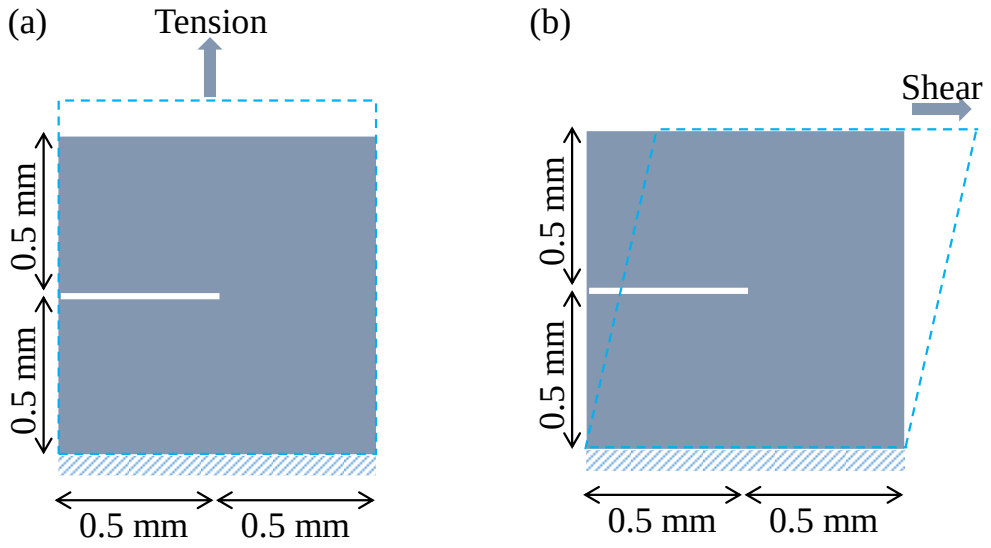

Fig III- 2. Geometry of the single edge notched sample as reported in the work of Miehe et al. [136] subjected to: a) tension and b) shear loadings.

III.4.1. Single edge notched sample under tensile loading

The boundary conditions used for the tensile loading on the single edge notched sample are indicated in Fig. III-2a. The PFM simulations obtained for the two values of ℓ are depicted in Fig. III-3. As expected, the direction of the crack propagation is found independent of the regularization parameter ℓ. Indeed, the crack extends in the same direction of the notch. However, the width and the length of the propagated crack are risen when increasing the regularization parameter ℓ. Moreover, the load-displacement responses are also found in good agreement with those published by Miehe et al. [136]. For instance, the critical load, triggering the fracture, is retrieved almost perfectly. Indeed, the discrepancy between the two predictions is less than 2.8% for the two length scale parameters.

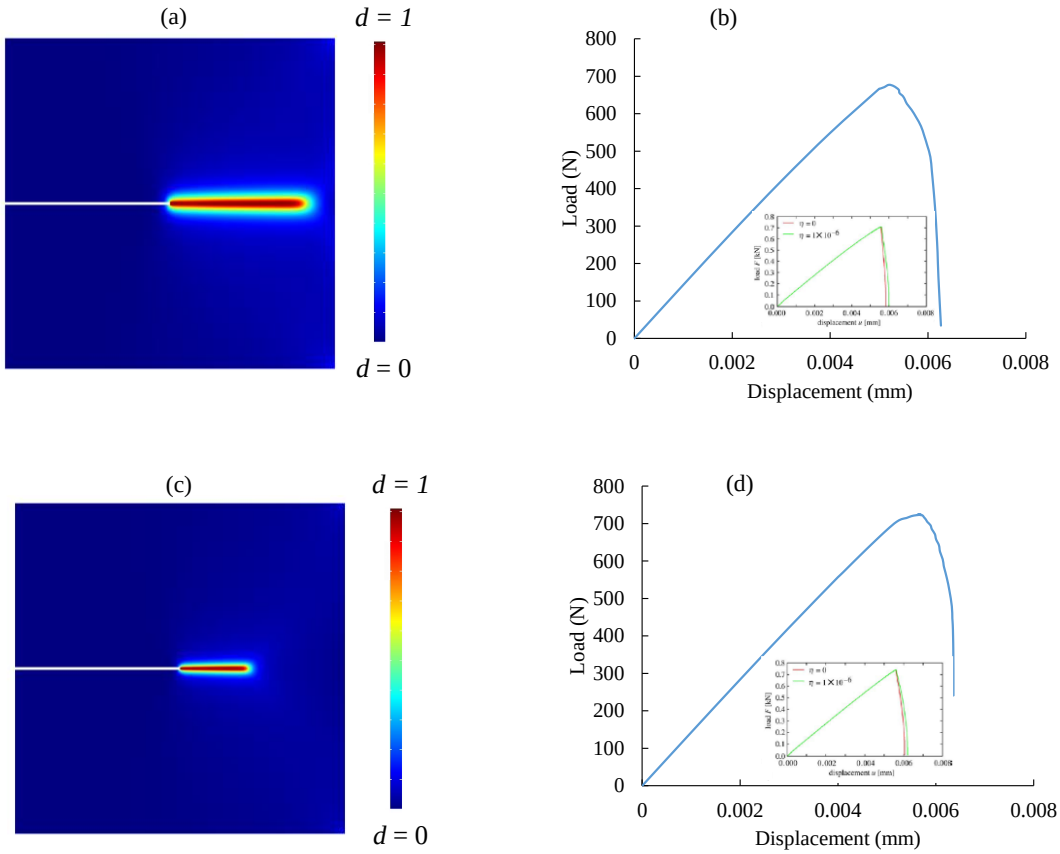

Fig III- 3. Phase field reasults for a single edge notched sample under tensile loading: pattern crack with a) ℓ_1= 0.015 mm, c) ℓ_2= 0.0075 mm and load-displacement response with b) ℓ_1= 0.015 mm, d) ℓ_2= 0.0075 mm. The insert in (b) and (d) corresponds to the results reported in Miehe et al. [13].

III.4.2. Single edge notched sample under shear loading

For the pure shear test, the boundary conditions are depicted in Fig. III-2b and the PFM results are shown in Fig. III-4. In this configuration, the crack is found to propagate with a given angle from the initial-crack plane. As expected, the simulated direction of propagation of the crack is independent of the choice of the length scale parameter ℓ (Fig. III-4a,c). Moreover, this angle agrees with the one reported in Miehe et al. [136]. In addition, as shown in (Fig. III-4b,d), the load-displacement evolution and the critical load triggering the fracture are retrieved. Indeed, the critical fracture load is found equal to around 565 N and 595 N for ℓ_1 and ℓ_2, respectively which are consistent with the predictions in Miehe et al [13]

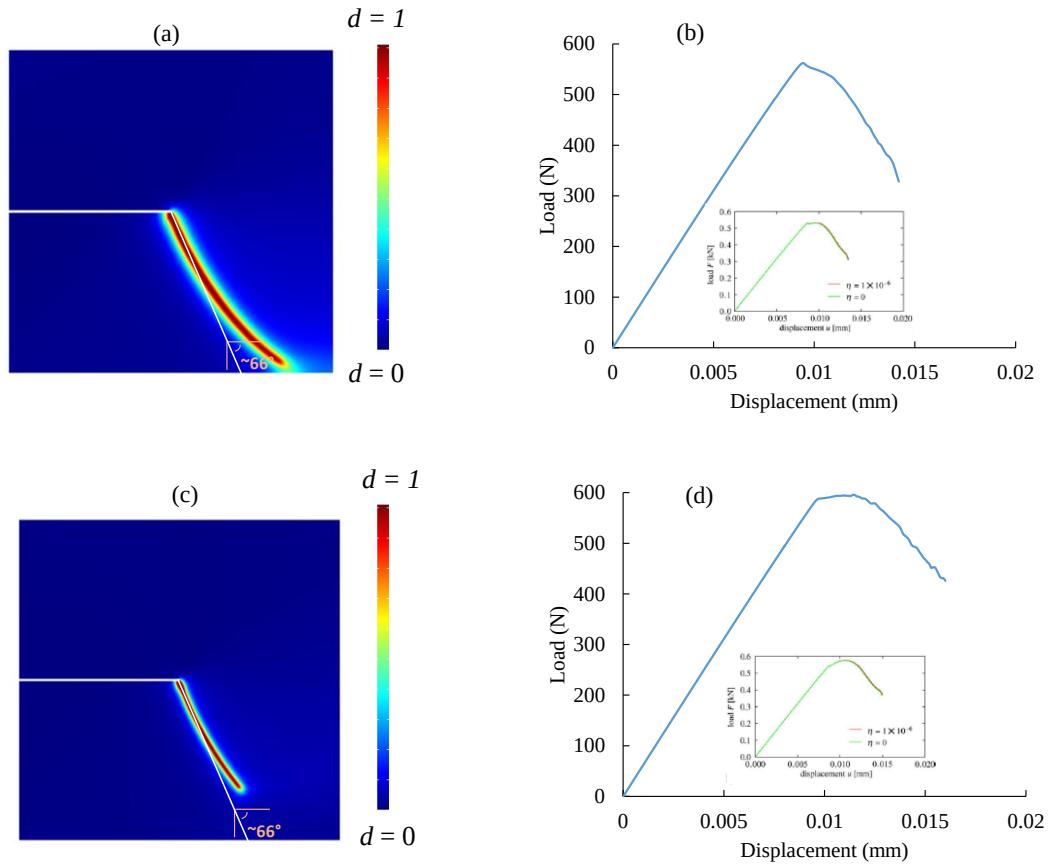

Fig III- 4. Phase field reasults for a single edge notched sample under shear loading: pattern crack with a) ℓ_1= 0.015 mm, c) ℓ_2= 0.0075 mm and load-displacement response with b) ℓ_1= 0.015 mm, d) ℓ_2= 0.0075 mm. The insert in (b) and (d) corresponds to the results reported in Miehe et al. [13].

To conclude, for both shear and traction configurations, a good agreement has been found between the simulated results and the data reported in the work of Miehe et al. [136], thus validating the PFM model implementation.

III.5. Evaluation of the PFM capacity to accurately predict the crack nucleation

III.5.1. Methodology

In order to evaluate the capacity of the phase-field approach to accurately predict the crack nucleation and investigate the nature of the length scale parameter ℓ, the PFM results have been compared to the predictions given by the coupled criterion [85] on ideal geometries. Firstly, V-notched samples with different opening angles have been studied to address the case of crack nucleation from an ideal stress singularity [85]. Secondly, in order to mimic the fracture in

porous ceramics, the crack nucleation from a stress concentration represented by a macro-crack blunted by a cavity [67,155] has been simulated.

It is to be noted that the comparison has been conducted considering the two types of zirconia stabilized with 3% and 8% molar of Yttria (3YSZ and 8YSZ), classically used in the electrolyte and electrode SOC layers, exhibiting different fracture properties. Indeed, as reported in Table III-1, the yttrium content in YSZ has a strong impact on the material fracture properties. For example, the strength and toughness of dense 3YSZ are roughly two and three times higher than dense 8YSZ, respectively [16].

All the simulations have been performed with the plane strain elasticity assumption for a classical three-point bending symmetric test, ensuring the creation of the crack under a pure symmetric mode. Moreover, for all the phase-field computations, it is worth noting that a special attention was paid to check the convergence of the simulations. More specifically, the number of iterations for the staggered resolutions was chosen so that the results are independent of the loading step. For this purpose, when the damage parameter exceeds 0.4 during the simulations, the loading increment was divided by 100. Besides, the independence of the result with the mesh size was also verified for all the simulations. It can be noticed that a very fine mesh was considered in the anticipated damage zone: for instance, more than 15 elements were included in the width 2ℓ for the 2D simulations. Finally, all the simulations have been carried out in such a way that the softening effect on the load-displacement curve due to a large damage zone remains negligible.

Table III- 1. Mechanical properties of 3YSZ and 8YSZ.

Material	E [GPa]	$\boldsymbol{\nu}$	$\boldsymbol{K_{Ic}}$ [MPa.$\sqrt{\mathbf{m}}$]	$\boldsymbol{\sigma_c}$ [MPa]	$\boldsymbol{l_{Irwin}} = \left(\frac{K_{Ic}}{\sigma_c}\right)^2$ [µm]	reference
3YSZ	214	0.31	5.1	583	76.5	[68]
8YSZ	216	0.31	1.61	245	43.2	[102,103]

III.5.1.1. Crack nucleation from a stress singularity: V-notched sample

The considered geometry of the V-notched sample with different opening angles 2β is illustrated in Fig. III-5. The length and height of the beam are L = 8 mm and h = 2 mm, respectively, while the notch depth is a_n = 0.4 mm.

It is worth noting that the coupled criterion allows computing the apparent toughness K_{Ic}^{notch} for the notch while the critical load F_c triggering the crack initiation is calculated with the PFM

model. Therefore, the two approaches have been compared using the following expression [156]:

$$K_{Ic}^{notch} = \left(\frac{3F_c L}{2bh^2}\right) h^{(1-\lambda)} f\left(\frac{a_n}{h}\right) \quad \text{(III-27)}$$

Where b denotes the beam thickness taken to the unity for the 2D simulations. The exponent λ is the singularity order for a symmetric loading, which is obtained by solving the following equation [156]:

$$\lambda sin(\pi - \beta) + sin\big(2\lambda(\pi - \beta)\big) = 0 \quad \text{(III-28)}$$

The dimensionless factor $f\left(\frac{a_n}{h}\right)$ in Eq. (III-27) is the polynomial function given in eq. (III-29):

$$f\left(\frac{a_n}{h}\right) = c_1 \frac{a_n}{h} + c_2 \frac{{a_n}^2}{h} + c_3 \frac{{a_n}^3}{h} + c_4 \frac{{a_n}^4}{h} + c_5 \frac{{a_n}^5}{h} \quad \text{(III-29)}$$

The coefficients c_i are tabulated in [156] for a ratio $\frac{a_n}{h}$ ranging between 0.05 and 0.7. It can be noticed that the dimensions of the simulated specimen have been chosen to fulfill this condition on the ratio $\frac{a_n}{h}$. Three notch angles $2\beta \in \{60°, 90°, 120°\}$ have been investigated to sweep a large range of singularity orders, from a crack initiation mainly controlled by the energy criterion for $2\beta = 60°$ to a non-negligible contribution of the stress criterion for $2\beta = 120°$.

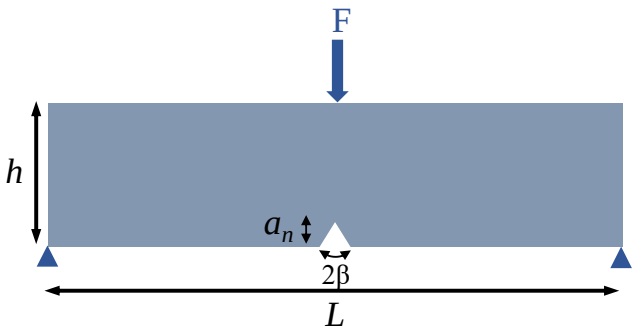

h (mm)	2
L (mm)	8
a_n (mm)	0.4
β (°)	{30, 45, 60}

Fig III- 5. Three-point-bending test on a V-notched sample.

III.5.1.2. Crack nucleation from a stress concentration: crack blunted by a cavity

The simulated beam with a preexisting crack blunted by a cavity is shown in Fig. III-6. Its geometry is the same as the previous V-notched case with same crack length of a_c = 0.4 mm.

In this case, the fracture toughness K_{Ic} and the applied critical loading F_c are linked as follows:

$$K_{Ic} = \left(\frac{F_c}{b\sqrt{h}}\right) f\left(\frac{a_c}{h}\right) \tag{III-30}$$

The dimensions of the studied geometry fulfil the condition $\frac{a_c}{h} \in [0.05, 0.7]$ for which the dimensionless factor $f\left(\frac{a_c}{h}\right)$ is expressed as [157]:

$$f\left(\frac{a_c}{h}\right) = \frac{3\frac{L}{h}\sqrt{\frac{a_c}{h}}}{2\left(1+2\frac{a_c}{h}\right)\left(1-\frac{a_c}{h}\right)^{\frac{3}{2}}}\left[1{,}99 - \frac{a_c}{h}\left(1-\frac{a_c}{h}\right)\left\{2{,}15 - 3{,}93\left(\frac{a_c}{h}\right) + 2{,}7\left(\frac{a_c}{h}\right)^2\right\}\right] \tag{III-31}$$

Four porosities have been considered with a radius r ranging from 0.01 mm to 0.03 mm. These cavity sizes remain very small with respect to the crack length so that Eqs. (III-30) and (III-31) remain valid for assessing the apparent fracture toughness K_{Ic}^{app}. Moreover, the width δ_c of the preexisting crack introduced in the mesh was small as compared to the pore size (*i.e.* δ_c= 3 µm << $2r$).

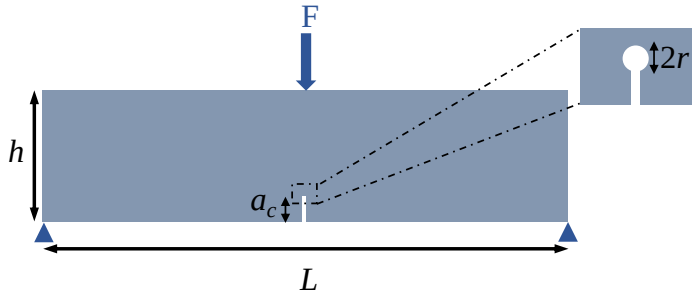

h (mm)	2
L (mm)	8
a_c (mm)	0.4
r (mm)	{0.01, 0.02, 0.03}

Fig III- 6. Three-point-bending test on a sample with a crack blunted by a cavity.

III.5.1.3. Coupled criterion

The coupled criterion stipulates that the crack initiation is triggered when both the stress and energy criteria are fulfilled. This condition can be reached when the applied stress σ_0 reaches a critical value σ_0^c leading to the nucleation of a crack with an initial length l_0^c [85]. When the crack initiation occurs with an initial length l_0, the stress criterion requires that the local stress must exceed the material strength σ_c along the expected crack path, as expressed in Eq. (III-

32). Regarding the energy criterion, the incremental energy release rate G_{inc}, which is the change in the potential energy W_p due to the crack nucleation, must be higher than the material fracture toughness G_{c} as formulated in Eq. (III-33):

$$\sigma(x) \geq \sigma_c \quad \text{for} \quad 0 < x < l_0 \tag{III-32}$$

$$\mathrm{G_{inc}}(l_0) = -\frac{\delta W_p}{l_0} \geq \mathrm{G_c} \tag{III-33}$$

The local stress $\sigma(x)$ and the energy release rate $\mathrm{G_{inc}}(l_0)$ introduced in the two last equations can be expressed as a function of the applied stress σ_0 using matched asymptotic expansions between the singular and the far fields [158]:

$$\sigma(x) = k(x)\,\sigma_0 \quad \text{for} \quad 0 < x < l_0 \tag{III-34}$$

$$\mathrm{G_{inc}}(l_0) = A(l_0)\,\sigma_0^2 \tag{III-35}$$

Where the dimensionless coefficients k and A depend on the crack length l_0, the material properties and the local geometry where the crack initiates.

It is worth noting that the coefficient k decreases with increasing l_0 whereas A is an increasing function of l_0. Therefore, combining Eqs. (III-32) and (III-34), the stress condition provides an upper bound for the nucleation since the applied loading σ_0 increases with l_0 (Fig. III-7). The lower bound for nucleation is provided by the energy condition combining Eqs. (III-33) and (III-35). The coupled criterion corresponds to the configuration where the two conditions are fulfilled by minimizing the applied stress σ_0 denoted σ_0^c. In this condition, a unique solution for a critical crack length l_0^c is obtained, as shown in Fig. III-7.

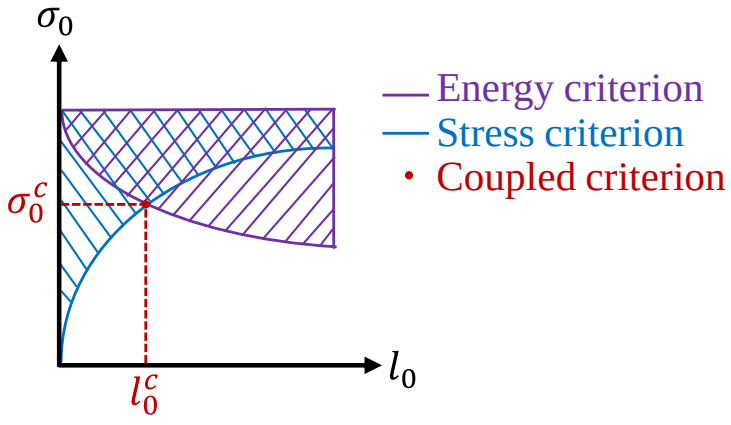

Fig III- 7. Applied loading as a function of crack length obtained using the stress (in blue) and the energy (in purple) criteria. The coupled criterion is chosen among the admissible solutions such that l_0^c minimizes the applied loading σ_0^c (in red).

In the case of the V-notched sample submitted to a symmetric loading, the coupled criterion is formulated as follows [85]:

$$K_{\mathrm{I}} \geq K_{Ic}^{notch} \text{ with } K_{Ic}^{notch} = \left(\frac{G_{\mathrm{c}}}{\Lambda(\beta)}\right)^{1-\lambda} {\sigma_c}^{2\lambda-1} \tag{III-36}$$

Where K_{I} is the generalized stress intensity factor and the term $\Lambda(\beta)$ is a scaling coefficient depending on the notch opening angle. In this case, an analytical expression can be derived for the critical length:

$$l_0^c = \frac{1}{\Lambda(\beta)} \frac{G_{\mathrm{c}}}{{\sigma_c}^2} = \frac{1}{\Lambda(\beta)\hat{E}} \frac{{K_{\mathrm{Ic}}}^2}{{\sigma_c}^2} \tag{III-37}$$

Where $\hat{E}$ is the Young modulus for the plane strain condition ($\hat{E} = \frac{E}{1-\nu^2}$). Eq. (III-37) indicates that the critical length is proportional to the Irwin length ($l_{\mathrm{Irwin}} = \frac{{K_{\mathrm{Ic}}}^2}{{\sigma_c}^2}$) through a factor depending on the notch opening and the Young modulus.

For a crack blunted by a cavity, it is worth mentioning that the matched asymptotic expansion for expressing $\sigma(x)$ and $\mathrm{G_{inc}}(l_0)$ has been conducted using the pore size to describe the local geometry at the crack tip [67,155]. Therefore, the apparent toughness for a blunted crack K_{Ic}^{app} is not only dependent on l_0 but also on the pore radius r [67]:

$$K_{Ic}^{app} = \left(\frac{G_{\mathrm{c}}}{\mathrm{D}(r, l_0)}\right)^{1/2} \tag{III-38}$$

Where D is a function of r and l_0. In this case, the critical length for the crack nucleation must depend on both the pore radius and the Irwin length (*i.e.* $l_0^c = f\left(r, \frac{{K_{\mathrm{Ic}}}^2}{{\sigma_c}^2}\right)$). However, there is no analytical expression for this length, which must be calculated by solving a non-linear equation as detailed in [155].

The computation for the coupled criterion has been carried out with the FE free software code Modulef.

III.5.2. Results and discussions

In this section, the results of the PFM simulations, conducted on the stress singularity and stress concentration configurations, are presented and compared to those performed using the coupled criterion. The capacity of the model to predict accurately the crack nucleation is evaluated and the nature of the length scale parameter ℓ is discussed.

III.5.2.1. V-notched 8YSZ sample

Preliminary computations have been conducted with the PFM model to simulate the crack pattern in the V-notched 8YSZ sample considering two length scale parameters (*i.e.* ℓ_1=0.01 mm and ℓ_2=0.04 mm). It can be noted that the classical undamaged condition ($\overline{\nabla} d \,.\, \overline{\mathbf{n}}$ =0) was retained for the notch. As shown in Fig. III-8a and III-8b, the crack initiates from the stress singularity and propagates in pure symmetric mode for both cases. Therefore, as stated during the benchmark analysis, the PFM is able to identify correctly the zone where the crack nucleates as well as its direction of propagation whatever the value of ℓ [136] (Fig. III-8a and III-8b). Moreover, it can be seen that the crack becomes thicker when ℓ is larger since this regularization parameter controls the width of the region of transition from the pristine material to the fully broken state. Fig. III-8c further shows that the force-displacement curve for ℓ = 0.04 mm is slightly below the one calculated for ℓ = 0.01 mm before the rupture. This result is due to the material softening effect during the loading, which is more pronounced when ℓ is larger as previously mentioned.

As discussed in section III.1.2, the critical loading triggering the fracture is found to be strongly dependent on the choice of ℓ. To investigate the role of ℓ on the crack onset, the critical loading has been determined for several opening angles of the V-notched 8YSZ specimen.~

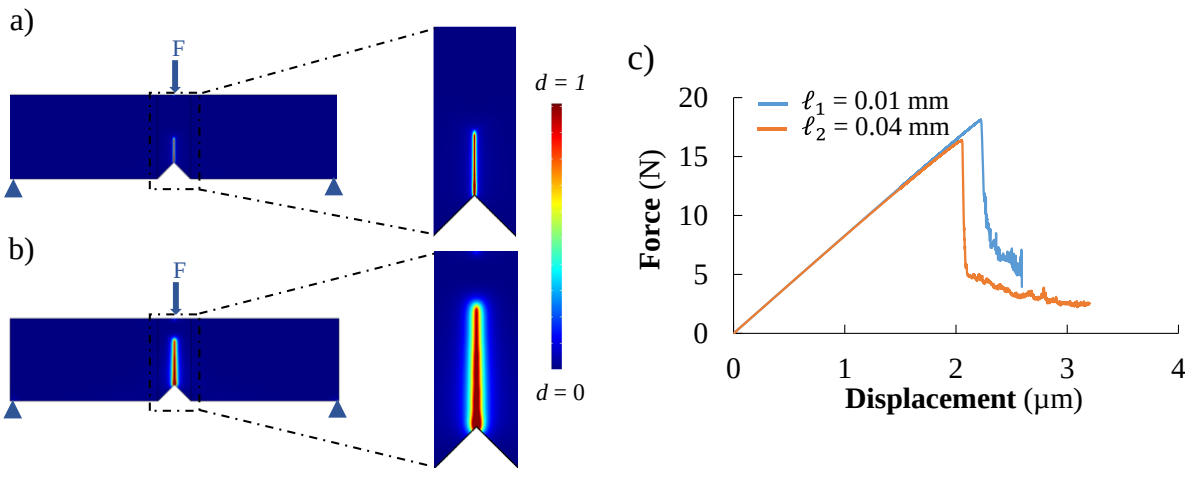

Fig III- 8. Visualization of the crack pattern initiated from a notch at an opening angle 2β of 90° for: a) ℓ_1 = 0.01 mm, b) ℓ_2 = 0.04 mm. c) Force-Displacement curves considering the 8YSZ material at a V-notch angle 2β of 90° for ℓ_1 = 0.01 mm and ℓ_2 = 0.04 mm.

The critical loading F_c was retrieved from the simulated force-displacement curves at the increment when the phase-field parameter d reaches ≈1 at the notch tip. The evolutions of the apparent facture toughness deduced from these computations are compared to the coupled criterion predictions in Fig. III-9a. When the regularization parameter is increased, the apparent fracture toughness computed with the phase-field is increased especially at the highest opening angles. At the lowest angle ($2\beta = 60°$), it can be noted in Fig. III-9a that the apparent fracture toughness is almost independent of ℓ. This behavior is explained since the singularity order at $2\beta = 60°$ is very close to the exponent 0.5 for a perfect crack (*i.e.* $\lambda = 0.5122$ for $2\beta = 60°$). In this condition, the crack initiation is mostly governed by an energy criterion. As pointed out by Tanné at al. [151], the phase-field method, which is based on a pure energetic approach for the crack propagation, is thus able to simulate the fracture initiation from a sharp singularity with a low sensitivity on the length scale parameter ℓ. On the contrary, at the highest opening angle, the apparent fracture toughness is strongly dependent on the choice of ℓ for the simulations (Fig. III-9a). Indeed, the low singularity order at $2\beta = 120°$ (i.e. $\lambda = 0.6157$) means that the fracture behavior is partially controlled by the stress criterion [85,155]. In this regime, the prediction provided by the phase-field method, which does not consider the stress criterion, becomes a function of the regularization parameter. In other words, the choice of ℓ is crucial for accurate predictions by the phase-field model when the fracture is partially controlled by the stress criterion.

Owing to the above discussion, the regularization parameter ℓ could be seen as a pure numerical parameter that must be adapted for each configuration, as suggested by Kumar et al. [153]. Nevertheless, inspection of the results indicates that a single value of ℓ denoted ℓ_{8YSZ} can be identified in such a way that the apparent fracture toughness computed by the phase-field matches the coupled criterion prediction over the full span of investigated angles (Fig. III-9a). Indeed, the PFM simulations obtained with ℓ_{8YSZ}= 0.01 mm provides a precise prediction of the crack nucleation with a mean relative error lower than 2.4 %. For this *ad-hoc* value of ℓ, the PFM model is thus able to accurately reproduce the apparent toughness evolution when the fracture mechanism is changed from an energy controlled criterion to a coupled criterion. In other words, the length scale parameter allowing retrieving the coupled criterion predictions is found to be independent of the notch opening angle. The possibility to identify a single value of ℓ_{8YSZ} suggests that this parameter could have a physical meaning and would contain the information to take into account the fracture properties involved in both criteria (*i.e.* toughness and strength). From this point of view, ℓ_{8YSZ} could be related to a characteristic length of the

material such as the Irwin length l_{Irwin} or the critical length l_0^c involved in the coupled criterion (*cf*. Eq. (III-37)). This statement is in good agreement with Tanné et al. [151] and suggests that, as for the uni-axial traction [150], the length scale parameter must be proportional to the Irwin length.

The critical loading leading to the fracture is plotted in Fig. III-9b as a function of the opening angles 2β for the investigated length scale parameters. As expected, the critical force is almost independent of ℓ at the lowest angles, whereas it decreases with increasing ℓ at the highest angles (Fig. III-9b-c). This dependence of the critical force (Fig. III-9b) associated to the apparent fracture toughness (Fig. III-9a) with the regularization parameter at high opening angles was also observed in Tanné et al. [151]. This behavior can be interpreted through the relationship between the regularization parameter and a material characteristic length (l_{Irwin} or l_0^c). Indeed, if ℓ is proportional to l_{Irwin} or l_0^c, a large value of this parameter is related to a very low material strength. Since the fracture at high opening angle is partially governed by the strength criterion [85], the critical force or the apparent fracture toughness must decrease with increasing ℓ.

Due to this evolution, a decrease of the critical loading F_{c} is observed when increasing 2β for $\ell = 0.4$ mm (Fig. III-9b). Under this condition, the material fracture strength must be very low in such a way that the stress criterion is more easily fulfilled while the contribution of the energy criterion is enhanced. In this case, the force triggering the fracture is decreased with increasing 2β since the energy criterion is more easily fulfilled when the opening angle is large (note that K_{Ic}^{notch} is still an increasing function of 2β at $\ell = 0.4$ mm due to the evolution of the term $h^{(1-\lambda)}$ in Eq. (III-27)). This discussion reinforces the claim that, for a V-notched singularity, the regularization parameter in the phase-field model must be related to a material characteristic length such as l_{Irwin} or l_0^c.

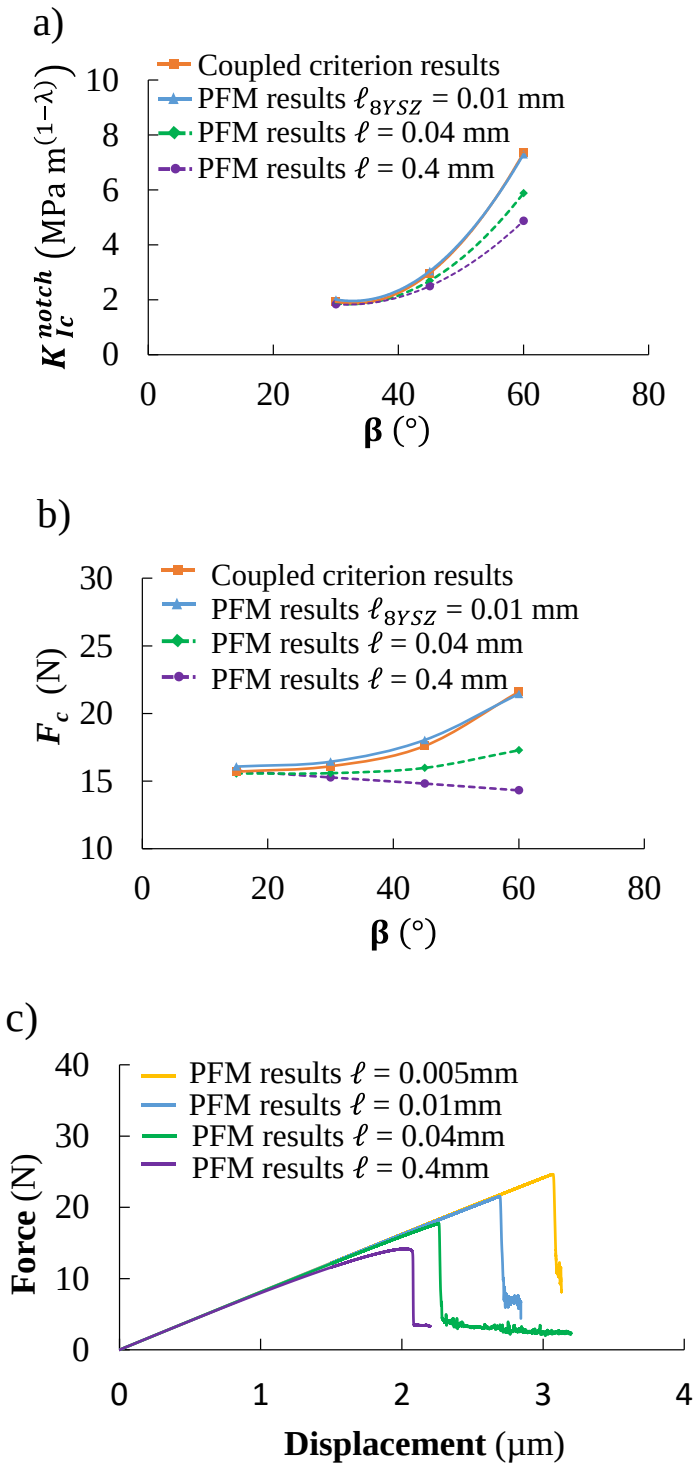

Fig III- 9. Dependence of the mechanical response of the V-notched 8YSZ sample on the opening angle considering different values of the length scale parameter ℓ: a) apparent fracture toughness, b) critical force triggering crack initiation. ℓ_{8YSZ} refers to the length scale parameter that provides close agreement between the coupled criterion and the PFM results over the whole considered range of notch angles, c) force-displacement curves at a V-notch angle 2β of 120°.

III.5.2.2. V-notched 3YSZ sample

The role of the material properties on the regularization parameter has been investigated by repeating the same study considering 3YSZ instead of 8YSZ. The apparent fracture toughness calculated with the PFM model is plotted in Fig. III-10 as a function of the V-notched opening angles for different values of ℓ. The results are consistent with the previous analysis since the same evolutions of K_{Ic}^{notch} with 2β and ℓ than the ones discussed for 8YSZ are observed. These evolutions are compared to the predictions given by the coupled criterion in Fig. III-10. As for the 8YSZ ceramic, it has been possible to identify an *ad-hoc* length scale parameter ℓ_{3YSZ} that allows retrieving the evolution of the theoretical fracture toughness with the opening angle. Indeed, the PFM results obtained for ℓ_{3YSZ} = 0.02 mm match the coupled criterion predictions with a mean relative error on the apparent fracture toughness estimated to 1.9 %. It is here worth noting that ℓ_{3YSZ} is two times higher than ℓ_{8YSZ}. This statement clearly shows that the regularization parameter changes with the simulated material. Moreover, the ratio $\frac{\ell_{3YSZ}}{\ell_{8YSZ}}$ =2 for the phase-field approach is almost equal to the theoretical ratio $\frac{l_{\text{Irwin}}^{3YSZ}}{l_{\text{Irwin}}^{8YSZ}} = \frac{l_0^{c,3YSZ}}{l_0^{c,8YSZ}}$ =1.8. Therefore, this analysis confirms that when considering the crack onset from a singularity, the regularization parameter in the phase-field method is proportional to the material characteristic length. This statement has far-reaching practical implications for the study of the V-notch configuration with the PFM model. Indeed, only a single study considering one material could be sufficient to determine the corresponding ℓ for any other brittle material.

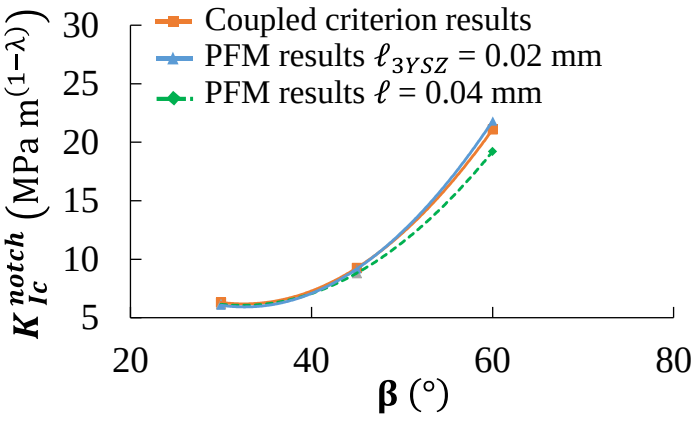

Fig III- 10. Dependence of the apparent fracture toughness on the opening angle for the 3YSZ material considering different values of the length scale parameter ℓ. ℓ_{3YSZ} refers to the length scale parameter that provides close agreement between the coupled criterion and the PFM results over the whole considered range of notch angles.

III.5.2.3. Crack blunted by a cavity in 8YSZ and 3YSZ

To study the crack nucleation from a stress concentration, a crack blunted by a cavity has been simulated for the 8YSZ and 3YSZ ceramics. The relative toughness $R = K_{Ic}^{app}/K_{Ic}$ obtained with the PFM method as well as the theoretical predictions given by the coupled criterion are plotted as a function of the pore radius in Fig. III-11. It can be noticed that the phase-field simulations have been carried out for various length scale parameters. As shown in Fig. III-11, the dependence of the PFM results on the regularization parameter is less pronounced when the pore radius is lowered. As for the notch configuration, this evolution can be explained since the geometry tends towards a sharp crack entirely controlled by a pure energy criterion. On the contrary, the dependence on the apparent toughness calculated with the PFM becomes significant at the highest investigated pore radius for which the contribution of the stress criterion to the fracture is non-negligible. In this case, the apparent fracture toughness is lowered with increasing ℓ. This evolution can be interpreted through a very low facture strength associated to the large length scale parameter. This explanation would mean that the regularization parameter can be still related to a material characteristic length for a stress concentration [151]. As illustrated in Fig. III-11a for 8YSZ, this dependence can lead to an incoherent behavior for ℓ =0.04 mm with a weakening effect with increasing the pore radius.

For both materials, it has been possible to identify two specific values for the regularization parameters ℓ_{8YSZ} and ℓ_{3YSZ} to fit accurately the predictions given by the coupled criterion (Fig. III-11). Indeed, the mean relative error on the relative fracture toughness simulated with ℓ_{8YSZ} = 0.005 mm and ℓ_{3YSZ} = 0.007 mm is equal to 1.1% and 1.2% for 8YSZ and 3YSZ respectively. Therefore, for a given value of ℓ, the PFM model is able to capture the expected strengthening effect due to the crack blunting by a cavity [67]. Nevertheless, it can be noted that the length scale parameters ℓ_{8YSZ} and ℓ_{3YSZ} identified for the V-notch singularity are not the same than the ones obtained for the blunted crack (for the same specimen submitted to a three-point bending test). For instance, the regularization parameter identified for the notch (ℓ_{8YSZ} = 0.01 mm) is significantly higher than the one for the blunted crack (ℓ_{8YSZ} = 0.005 mm). It can be noticed that if the length scale parameter for the notch is taken to ℓ_{8YSZ} =0.005 mm, the phase field results overestimate the coupled criterion predictions. In this case, the discrepancy between the critical forces provided by the coupled criterion and the phase field reaches almost 20% for a notch opening angle of 2β=120°. Such a discrepancy cannot be explained by the numerical inaccuracies in the phase-field simulations, which have been checked to be very

limited in our case. This result would thus suggest that the regularization parameter could be also a function of the type of local geometry where the crack nucleates.

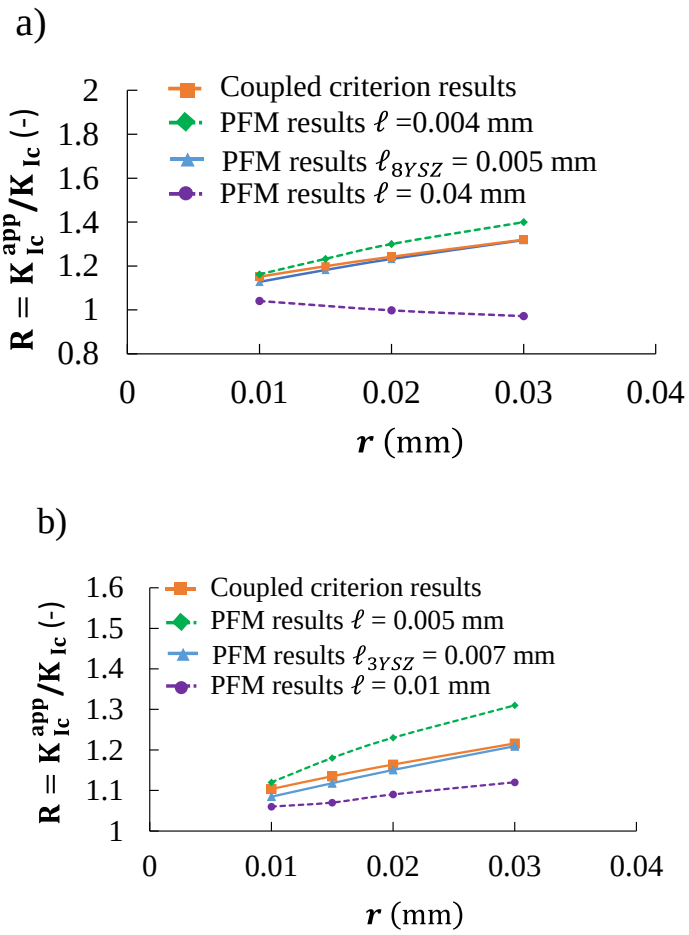

Fig III- 11. The dependence of the relative toughness on the cavity radius considering different values of the length scale parameter ℓ for: a) 8YSZ material, b) 3YSZ material. ℓ_{8YSZ} and ℓ_{3YSZ} refer to the length scale parameters that provide close agreement between the coupled criterion and the PFM results over the whole considered range of cavity radii.

It can be noticed that the ratio $\frac{\ell_{3YSZ}}{\ell_{8YSZ}}$ =1.4 obtained with the phase-field method for the blunted crack is different from the Irwin one $\frac{l_{\text{Irwin}}^{3YSZ}}{l_{\text{Irwin}}^{8YSZ}}$ =1.8. However, it is almost equal to the ratio of the characteristic length in the coupled criterion $\frac{l_0^{c,3YSZ}}{l_0^{c,8YSZ}}$ =1.5. This statement means that the length scale parameter ℓ for the phase-field method is related to the coupled criterion characteristic length l_0^c. For a V-notch singularity, the ratio $\frac{l_0^{c,3YSZ}}{l_0^{c,8YSZ}}$ is equivalent to the ratio given by the Irwin characteristic length as mentioned in the previous section. However, for a crack blunted by a

cavity, the characteristic length l_0^c is still a function of l_{Irwin} but also takes into account the local geometrical characteristics of the stress concentration [67,155] (*cf.* section III.5.1.3). This discussion reinforces the proposition that the length scale parameter must be dependent on the type of local geometry where the crack nucleates for a stress concentration. Even if further studies are still needed to investigate this possibility, it can be concluded from this analysis that the PFM model can be applied to predict the crack initiation in porous ceramic with a length scale parameter that have to be identified for each type of microstructures.

III.6. Conclusion

The relevance of the phase-field model for simulating crack nucleation and propagation has been evaluated on ideal geometries. For this purpose, the PFM results have been compared to the predictions of the coupled criterion based on linear fracture mechanics. The study has included two types of ceramics, whose fracture properties are significantly different (*i.e.* 3YSZ and 8YSZ). A pure singularity induced by a V-notch and a stress concentration related to a crack blunted by a cavity have been studied considering a three-point bending test.

In the V-notch case, considering a unique length scale parameter for the phase-field model ℓ, it has been shown that the PFM method is able to retrieve the coupled criterion predictions as a function of the notch-opening angle. Moreover, the ratio of the regularization parameter for the two ceramics is equal to the ratio for both the Irwin length and the characteristic length for the coupled criterion ($\frac{\ell_{3YSZ}}{\ell_{8YSZ}} \approx \frac{l_{\mathrm{Irwin}}^{3YSZ}}{l_{\mathrm{Irwin}}^{8YSZ}} = \frac{l_0^{c,3YSZ}}{l_0^{c,8YSZ}}$). Therefore, for an *ad-hoc* value of ℓ, the PFM method is able to predict correctly the facture initiation at singularities even when the crack nucleation is controlled by a coupled energy and stress criterion.

For a crack blunted by a cavity, the PFM model is also able to reproduce the theoretical dependence of the apparent fracture toughness on the pore size. In this case, the ratio of the selected length scale parameters for the two materials is no longer equal to the ratio for the Irwin length but remains identical to the one related to the coupled criterion ($\frac{\ell_{3YSZ}}{\ell_{8YSZ}} \approx \frac{l_0^{c,3YSZ}}{l_0^{c,8YSZ}} \neq \frac{l_{\mathrm{Irwin}}^{3YSZ}}{l_{\mathrm{Irwin}}^{8YSZ}}$). Moreover, the length scale parameter for the V-notch was found significantly different from the one identified for the blunted crack. This result suggests that the regularization parameter must be adapted for each type of local geometry from which the crack initiates. In

other words, this study indicates and lets anticipate the possibility to identify a single length scale parameter for each type of studied microstructures.

This analysis conducted with the coupled criterion and the phase-field method on ideal geometries indicates that the PFM model should be an appropriate method to predict the crack initiation in complex porous ceramic microstructures. Indeed, the PFM model was found able to accurately predict the fracture when it is not only governed by an energy criterion but also partially controlled by a stress criterion, as described by the established coupled criterion. Despite its energy-based formulation, the PFM model can be thus seen as an energy-stress criterion-based method thanks to the length scale parameter ℓ which contains information about the material fracture properties. In addition, the implementation of the PFM approach does not require additional numerical manipulation during simulation. Accordingly, the PFM model appears well adapted to the complex porous ceramic microstructures.

The next chapter is devoted to the simulation of fracture in real porous ceramic microstructures using the PFM model. The numerical results are then confronted to experimental data in order to assess the model relevance to predict the crack initiation and propagation in porous ceramics.

IV. Prediction of the crack initiation and propagation in porous ceramic microstructures: experimental validation

As discussed in the first chapter, the number of numerical studies published in the literature conducted on 3D porous ceramics is very limited. It has been shown that they were able to qualitatively reproduce the dependence of the fracture properties on porosity but failed to accurately predict experimental measurements [87,88,97]. Accordingly, an approach coupling modeling and experiments appears required to evaluate the relevance of a proposed numerical tool to study the fracture in porous ceramics.

Chapter three has shown that the PFM approach is promising to study the fracture of porous ceramics with complex microstructures. Indeed, the diffuse description of the crack through the smooth damage variable enables the simulation of the fracture without supplementary numerical manipulations to introduce and follow the crack in the computational domain (*cf.* chapter III). The mesh remains unchanged during simulations so that the model implementation is efficient in the case of complex porous microstructures. Moreover, the comparison between

the PFM simulations and the coupled criterion predictions on ideal geometries (*cf.* chapter III) has shown that the PFM model is able to capture the transition in the fracture criterion for the crack initiation. Indeed, despite the dependence of the PFM results on the length scale parameter ℓ, it has been found that accurate and physically-motivated predictions of the crack nucleation can be obtained if this parameter is correctly chosen. Further, the discussion on the nature of the length scale parameter ℓ has revealed that this parameter is dependent on the type of local geometry from which the crack initiates and contains information that enables taking into account the fracture properties involved in both criteria (strength and toughness). Therefore, the PFM model is expected able to accurately simulate with a single calibrated value of the parameter ℓ the fracture in porous ceramics for a given type of microstructure. This enables therefore to efficiently deal with the complexity related to (i) the identification of the fracture criterion (stress criterion, energy criterion or coupled stress-energy criterion) and (ii) the detection of the zone where the cracks nucleate in the complex 3D microstructure.

This fourth chapter extends the analysis of chapter three to the case of 2D and 3D computational domains representative of real porous ceramic microstructures, along with comparison with experimental results. In the first section, the methodology adopted to simulate the apparent fracture properties is detailed. In the second section, the apparent fracture toughness is computed considering porous 3YSZ microstructures with porosities ranging from 10% to 30% and compared to the published macro-scale data in [75]. Then, the compressive fracture strength of 8YSZ samples is calculated as a function of porosity (*i.e.* 33%-63%) and confronted to the micro-mechanical measurements detailed in chapter two. The underlying mechanisms of fracture in porous ceramic microstructures are discussed in the light of the simulation results. The relevance of the PFM model to predict the fracture of porous ceramics is therefore assessed.

IV.1. Methodology

The relevance of the PFM model to accurately predict the crack initiation and propagation in porous ceramics has been evaluated in two steps. Firstly, the relevance of the PFM approach for predicting the propagation of a preexisting macro-crack in real porous ceramics has been assessed using two-dimensional representative synthetic microstructures. The simulations have been performed with the plane strain elasticity assumption for a classical three-point bending symmetric test, ensuring the creation of the crack under a pure symmetric mode. The results

have been compared to the experimental data reported in [75] related to the apparent fracture toughness measured on porous 3YSZ macro-scale specimens.

Secondly, the PFM has been applied to simulate the crack initiation in real uncracked microstructures of 8YSZ samples submitted to a compression loading. The simulations have been conducted using as computational domains the 3D reconstructions of the porous 8YSZ microstructures investigated in the second chapter. The computed compressive fracture strength has been then compared to the measurements obtained on the same microstructures as a function of the porosity. The capacity of the PFM model to retrieve the change in the fracture mode from brittle behavior towards diffuse damage when increasing the porosity has been also evaluated.

IV.1.1. Propagation of a preexisting macro-crack in 2D porous ceramic microstructures

The sample geometry to simulate the crack extension with the PFM approach in 2D approximations of porous ceramics is displayed in Fig. IV-1a. The selected dimensions are L= 40 µm, h = 10 µm and a_c = 3 µm. The ratio $\frac{a_c}{h}$ is comprised between 0.05 and 0.7 in such a way that Eqs. (III-4) and (III-5) can be used to express the toughness as a function of the applied loading. As shown in Fig. IV-1a-c, three microstructures of different porosities $\varepsilon \in \{10\ \%, 20\ \%, 30\ \%\}$ have been simulated. These numerical microstructures have been generated using the Gaussian random field method [12,95]. Indeed, it has been shown that this method is able to emulate accurately the morphology of partially sintered ceramic microstructures, such as solid oxide fuel cell electrode materials [159]. The three microstructures have been generated by maintaining a constant correlation length for the solid YSZ phase [159]. As a result, the mean diameter of the YSZ phase calculated by continuous Particle Size Distribution (PSD) [160], is approximatively the same and equal to 0.45 µm for all the microstructures simulated in the present study. On the contrary, the mean pore diameter decreases from 0.22 µm to 0.05 µm when densifying the ceramic from 30% to 10%. In all cases, the size of the porosity remains small compared to the simulated preexisting crack length. Besides, the crack width set to δ_c = 0.1 µm is lower than the mean pore diameter for a porosity of 20% and 30% whereas for a porosity of 10%, the two dimensions δ_c and $2r$ are equivalent.

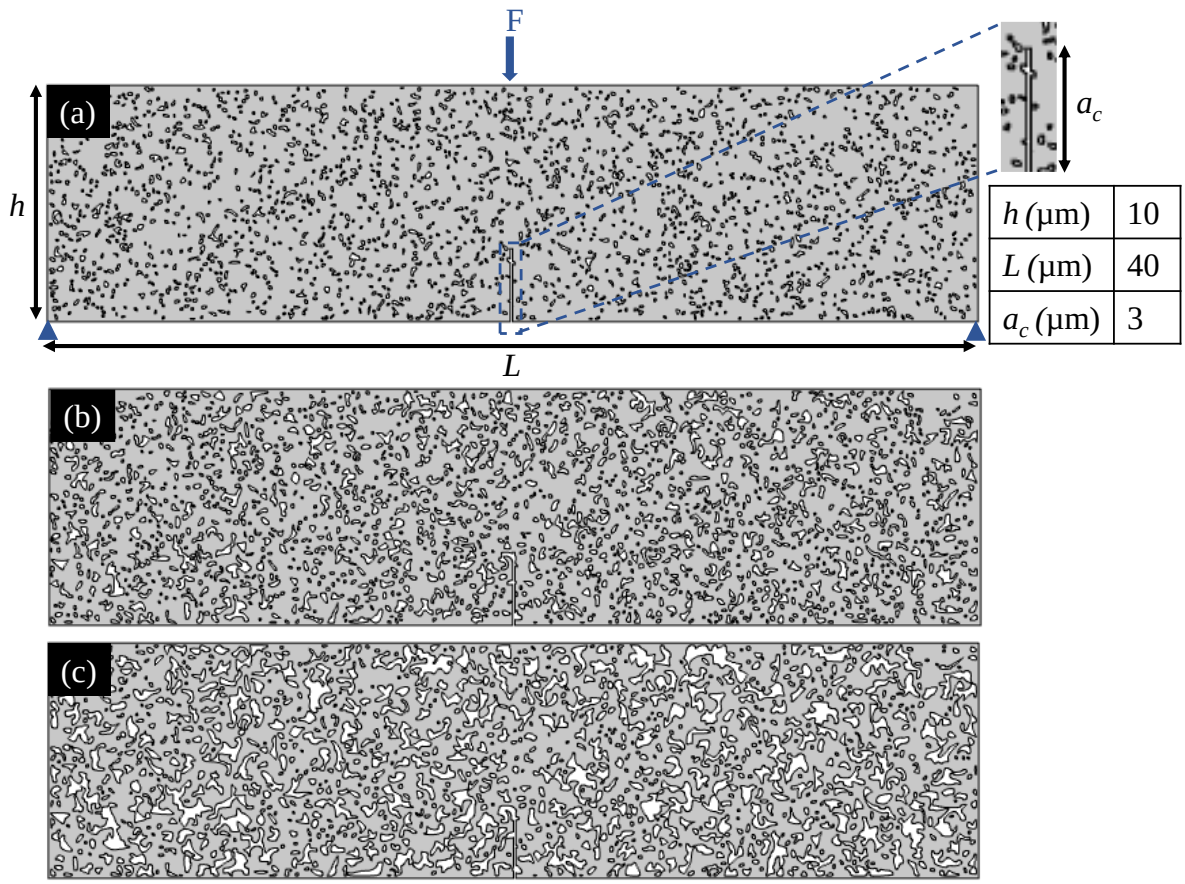

h (µm)	10
L (µm)	40
a_c (µm)	3

Fig IV- 1. Synthetic porous microstructures with different pore volume fractions ε (solid phase in grey): a) 10%, b) 20%, c) 30%.

IV.1.2. Crack nucleation in 3D

To study the crack nucleation in a real microstructure, the phase-field approach has been used to simulate the compressive fracture strength measured as a function of the porosities (from 33% to 63%) in the second chapter. A multi-scale approach has been adopted coupling computations on the whole micro-pillar (height of 130 µm, top surface diameter of 60 µm and taper angle of 6°) with simulations on 3D microstructure sub-volumes.

At the microstructure scale, the crack nucleation and propagation has been computed using the PFM method on sub-volumes extracted from the X-ray or electron microscopy reconstructions. For intermediate porosities below 50%, a volume of $4\times4\times4$ µm^3 has been simulated whereas a larger volume of $15\times15\times15$ µm^3 has been considered for the highest porosity at 63%. These dimensions of the simulated domain were chosen to be representative of the heterogeneous microstructures. Indeed, the measured pore mean phase diameter is lower than 0.13 µm for all the specimens at intermediate porosities but it is increased to 0.99 µm at 63% (*cf.* chapter II,

Table II-2). Therefore, even in the latter case, several pores remain included along an edge of the cubic computational domain (the characteristic size for the simulated volume is fifteen times larger than the mean pore diameter).

The solid phase of the reconstructed sub-volumes has been meshed using the software Avizo® considering tetrahedral elements (Fig. IV-2). This software offers the possibility to generate the 3D mesh of each phase separately. For the microstructures at intermediates porosities, the mesh was built using around 3.5×10^6 tetrahedrons (corresponding to around 17×10^6 degrees of freedom) while the volume at a porosity of 63 % contained 5.6×10^6 tetrahedrons (corresponding to around 26×10^6 degrees of freedom). The requirements in terms of mesh quality metrics were an element aspect ratio below 10 and a dihedral angle above 10°. For instance, a zoom of the generated mesh at a porosity of 63% in Fig. IV-2e shows that the surface of the solid phase inside the microstructure is smoothly meshed by the triangular elements mitigating numerical artifacts during the computation. The uniaxial compression has been simulated on the meshed reconstructions in displacement-controlled loading considering the properties of the dense 8YSZ (Table III-I).

At the micro-pillar scale, finite element simulations of the compression test were conducted assuming a homogeneous medium with a pure elastic behavior. A 2D approach including the full geometry of the tapered micro-pillar attached to a part of the pellet was considered using axisymmetric conditions (Fig. IV-3a). The size of the simulated pellet substrate was chosen in such a way that the mechanical response of the micro-pillar becomes independent of the boundary conditions applied at the bottom of the substrate (*i.e.* the displacements are blocked in the axial direction).

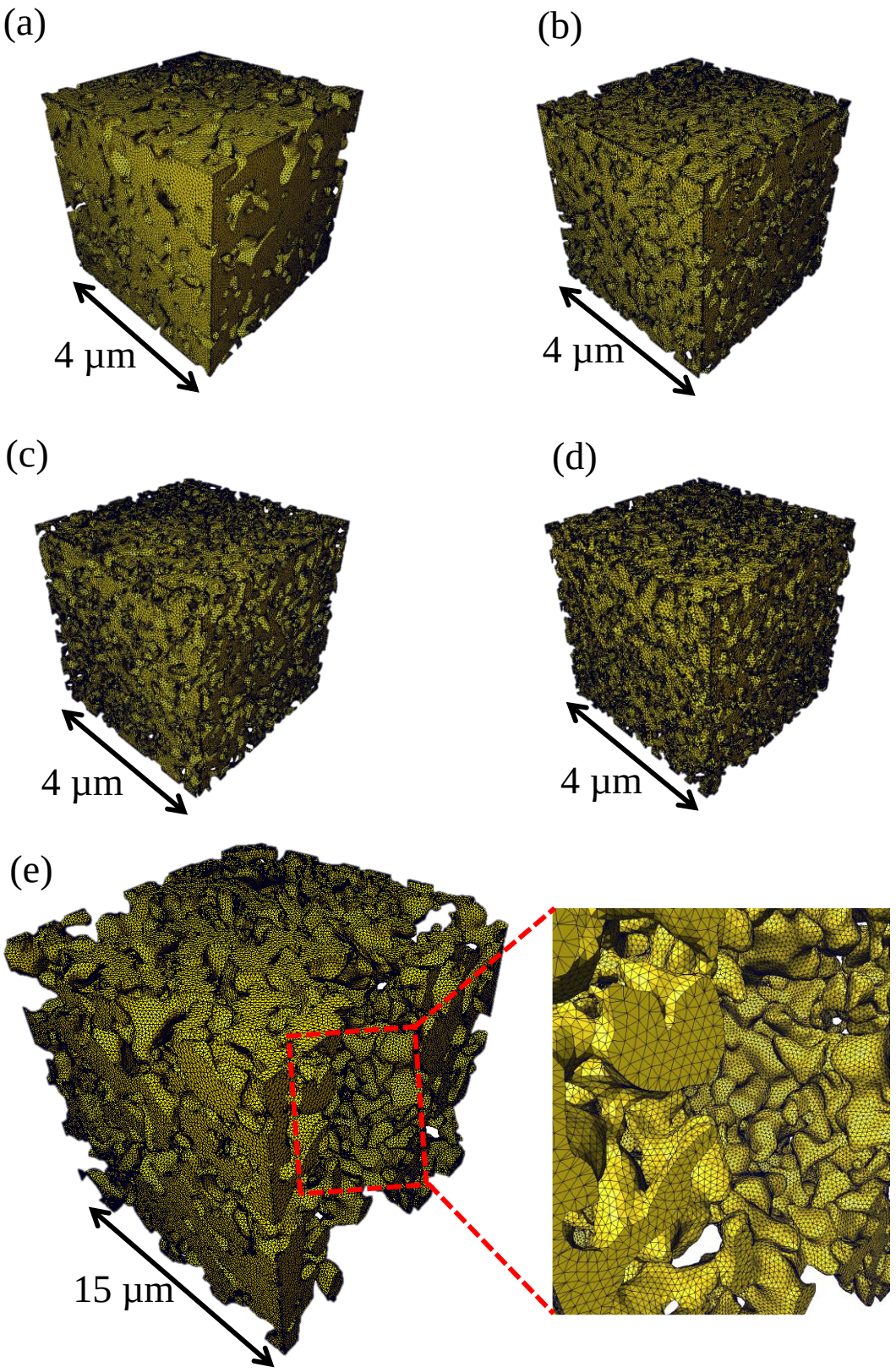

Fig IV- 2. Meshed 8YSZ microstructures at a porosity of: a) 33 %, b) 36 %, c) 40 %, d) 49 % and e) 63 %.

The simulations were performed using a Poisson's ratio of 0.31 and the effective Young's modulus measured by the micro-pillar experiments as a function of porosity in chapter two. Because of the taper angle, it is worth noting that a stress gradient appears in the pillar. For this reason, the cracks were observed during the experiments in the upper part of the pillar where the stress is the highest (*cf.* chapter II).

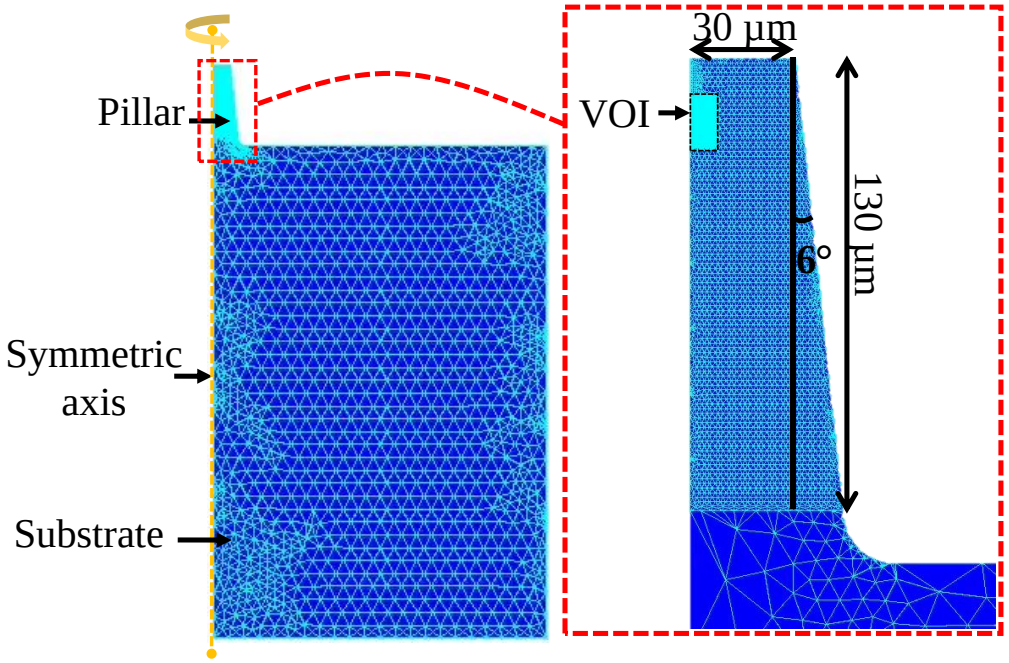

Fig IV- 3. Mesh of the tapered pillar attached to the pellet with axisymmetric conditions. A zoom on the pillar is shown together with the location of the Volume Of Interest (VOI) for the simulation at the microstructure scale using the meshes shown in Fig. IV-2.

The Volume Of Interest (VOI) for the modeling at the microstructure scale is therefore located at a short distance from the top of the pillar (*i.e.* 11 µm) where the damage is expected to occur. The difference in the displacements at the top and the bottom of the VOI surface was then extracted from the simulation at the macroscopic scale and applied on the reconstruction simulated with the phase-field. In this approach, the compressive fracture strength corresponds to the critical load applied at the top of the micro-pillar identified when the damage is initiated in the simulated microstructure.

IV.2. Results and discussions

In this section, the results of the PFM simulations obtained on 2D and 3D porous microstructures are presented and compared with the experimental data reported in [75] and [161] (*cf.* chapter II) respectively, in order to investigate the relevance of the PFM model to simulate the fracture in porous ceramics.

IV.2.1. Apparent fracture toughness of porous ceramics

To study the dependence of the apparent fracture toughness on the porosity, 2D porous 3YSZ microstructures have been generated with the random field method considering a constant correlation length for the solid phase (*cf.* section IV.1.1 and Fig. IV-1). As a result, the geometrical features of the simulated microstructures are preserved except modifications affecting mainly the porosity (*i.e.* volume fraction and pore mean diameter). Therefore, based on results presented in chapter three, a unique length scale parameter for the phase field is anticipated sufficient to predict the dependence of the apparent fracture toughness on the porosity. Two methods have been used to determine K_{Ic}^{app} from the phase-field simulations. In the first one (denoted '*method 1*' thereafter), the toughness was deduced when the fracture initiates at the tip of the preexisting macro-crack (with δ_c = 0.1 µm) blunted or not by a pore (*cf.* Fig. IV-4). In the second method (called '*method 2*'), the toughness was assessed after propagation, when the fracture is reinitiated from the first pore reached by the crack. The reason for using two methods is to provide an estimation of the toughness scattering induced by heterogeneities in the simulated microstructures.

For each porosity, two independent realizations (*i.e.* microstructures) exhibiting the same geometrical statistical properties have been generated using the Gaussian random field method. As an illustration for a porosity of 20%, it can be seen in Fig. IV-5 that the PSD of the two microstructures shown in Fig. IV-4a-b are nearly identical. The simulations of these two microstructures with a same porosity level provides a first estimation of the impact of local spatial variations on the toughness predictions. It is worth noting that these statistical variations in the local geometry preserve the same type of morphology since the same method and input parameters have been used to generate the microstructure.

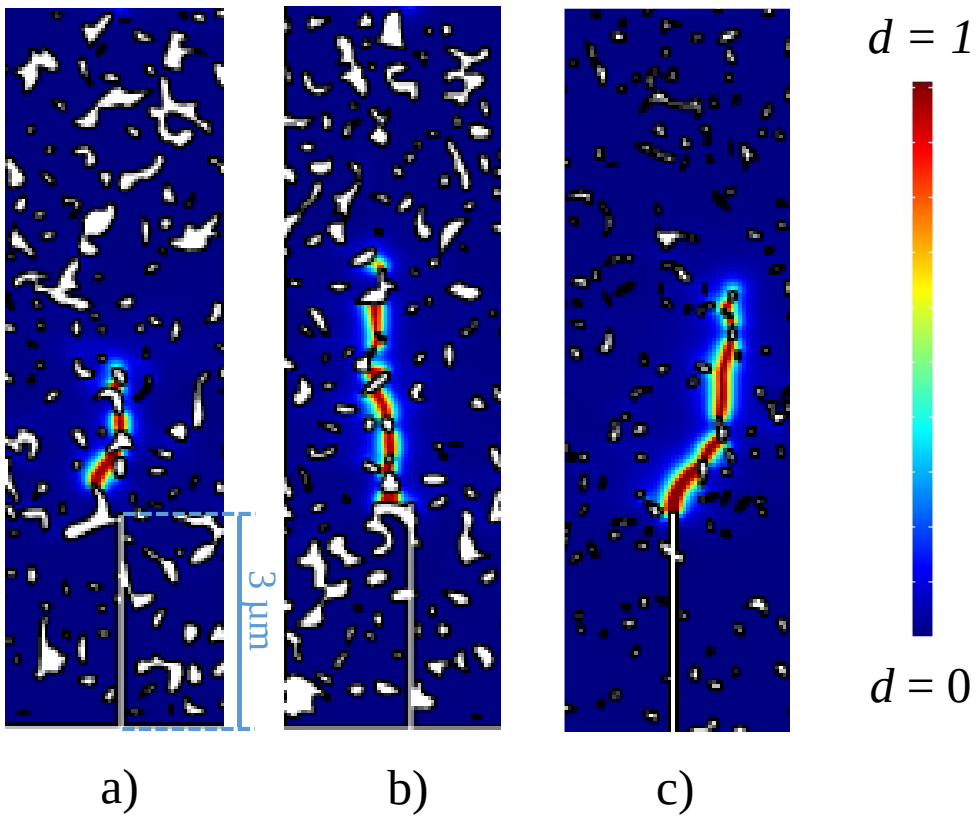

Fig IV- 4. Cartographies displaying crack paths within the porous microstructures: a) first realization at ε (porosity) = 20%, b) second realization at ε = 20%, c) first realization at ε = 10%. (ℓ_{3YSZ}= 0.1 µm).

Finally, as pointed out in section IV.1.1, the synthetic microstructures generated with the Gaussian random field method provide a good approximation of real porous ceramic microstructures produced by powder sintering [12]. Consequently, the experimental toughnesses reported in [75], which were measured using double-torsion testing on 3YSZ porous membranes produced by tape-casting have been selected for the comparison with the phase-field simulations.

All the simulations have been performed with a single length scale parameter $\ell_{3YSZ} = 0.1$ µm that remains small compared to the correlation length (*i.e.* 0.45 µm) used to generate the microstructures (*cf.* section IV.1.1).

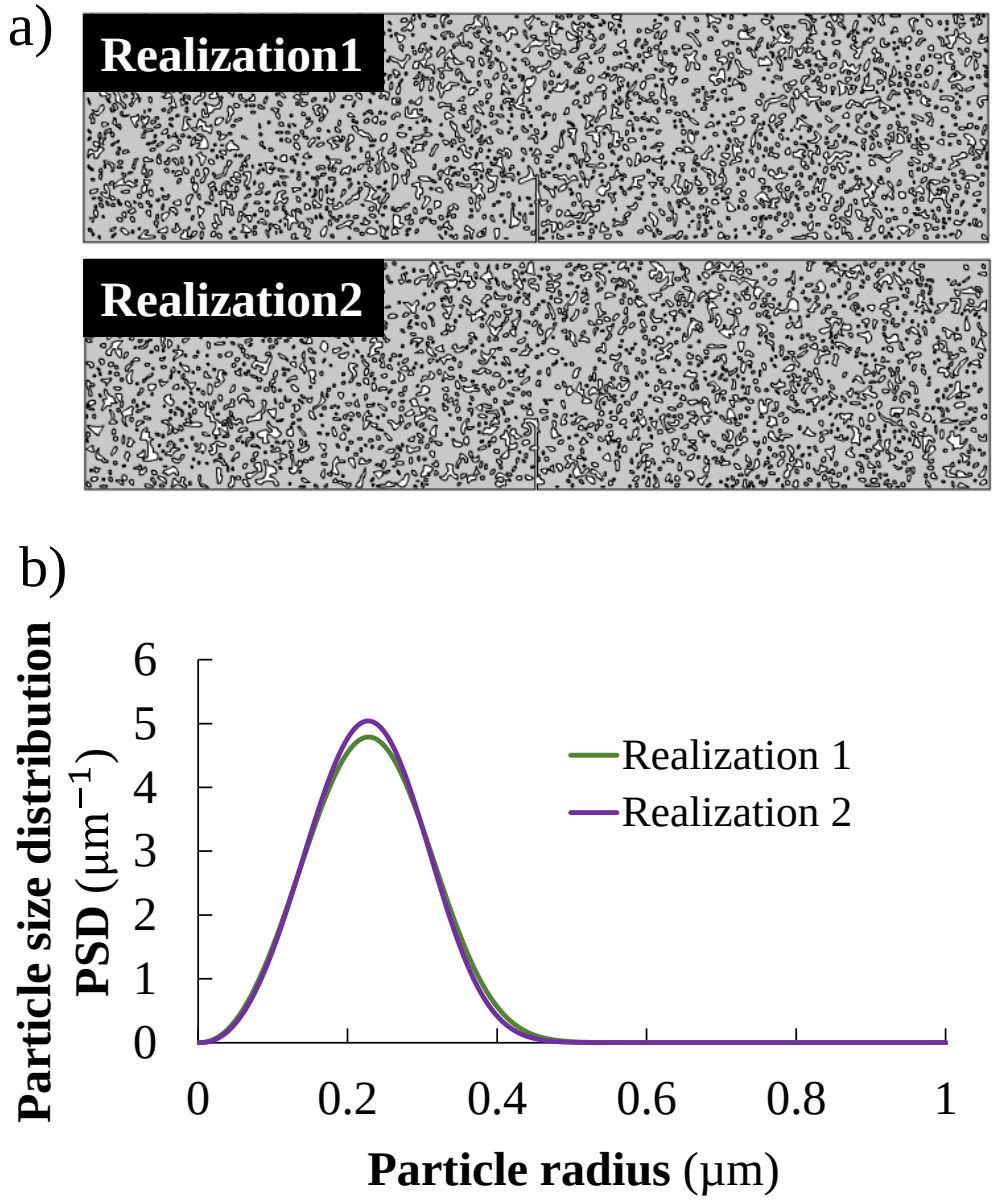

Fig IV- 5. Comparison between two generated synthetic microstructures with ε = 20%: a) visualization of the two realizations of the microstructure, b) Solid phase size distributions (2D) computed on the two realizations.

The apparent fracture toughnesses calculated on the first synthetic microstructure are compared to the experimental data in Fig. IV-6a. Independently of the method used to assess the toughness, the phase-field results are consistent with the measurements. The offset between the simulations and the experimental curve can be explained by the assumptions considered for the modeling, which are mainly (i) the hypothesis of 2D simulations for the phase-field model, and (ii) the differences between the synthetic microstructures and the real ones. Moreover, it is worth noting that the remaining disagreement offset between the experimental data and the

simulations can be further reduced by increasing ℓ_{3YSZ}. For example, it has been found that a regularization parameter ($\ell_{3YSZ} = 0.8$ µm) instead of ($\ell_{3YSZ} = 0.1$ µm) allows fitting almost perfectly the experimental data. Indeed, at a porosity of 10%, the computed fracture toughness with the *method 1* falls to $K_{Ic}^{app} = 3.8$ MPa.$\sqrt{\text{m}}$. However, a tradeoff has to be found for the length scale parameter. On the one hand, this parameter must be adapted to describe accurately the initiation step in order to predict the apparent fracture toughness. On the other hand, a sufficiently low width for ℓ must be preserved to describe correctly the subsequent crack propagation in the fine microstructure. From a practical point of view, if necessary, two length scale parameters may be considered for the simulations. The first one could be adapted to compute precisely the fracture initiation, while the second one could be chosen small compared to the size of the microstructure in order to describe the crack propagation in the porous ceramic.

Nevertheless, with a single length scale parameter, the model captures correctly the decrease of K_{Ic}^{app} with increasing the porosity. This result confirms the relevance of the phase-field method to predict the fracture toughness of porous brittle materials after calibration of the regularization parameter for a given type of microstructure. This supports the claim that this parameter contains material fracture properties so that the PFM model can be used to quantify the conditions for the propagation of a pre-existing crack in porous ceramics.

The comparison of the fracture toughness predictions as a function of the porosity for the two microstructures (displayed in Fig. IV-5) is shown in Fig. IV-6b. For the sake of clarity, only the results with the first method have been reported. The results fall within the same range for the two simulated microstructures. The slight difference between the two curves is due to local variations in the geometry at the preexisting macro-crack. Therefore, by keeping the same length scale parameter for the phase-field model, it is possible to estimate correctly the fracture toughness for two different microstructures exhibiting similar statistical features for the morphology. In other words, the fracture properties can be determined with a single regularization parameter for one type of porous media (having same morphological characteristics associated to the method of synthetic microstructure generation or to the manufacturing process). This statement is consistent with the previous discussion (*cf.* chapter III) on the dependence of the regularization parameter on the type of the local geometry where the crack initiates. For a complex microstructure, ℓ can be thus anticipated a function of metrics characterizing the shape on the solid and pore phases (*i.e.* shape of the pores, their statistical distribution, the solid ligaments between the pores, etc. [67]).

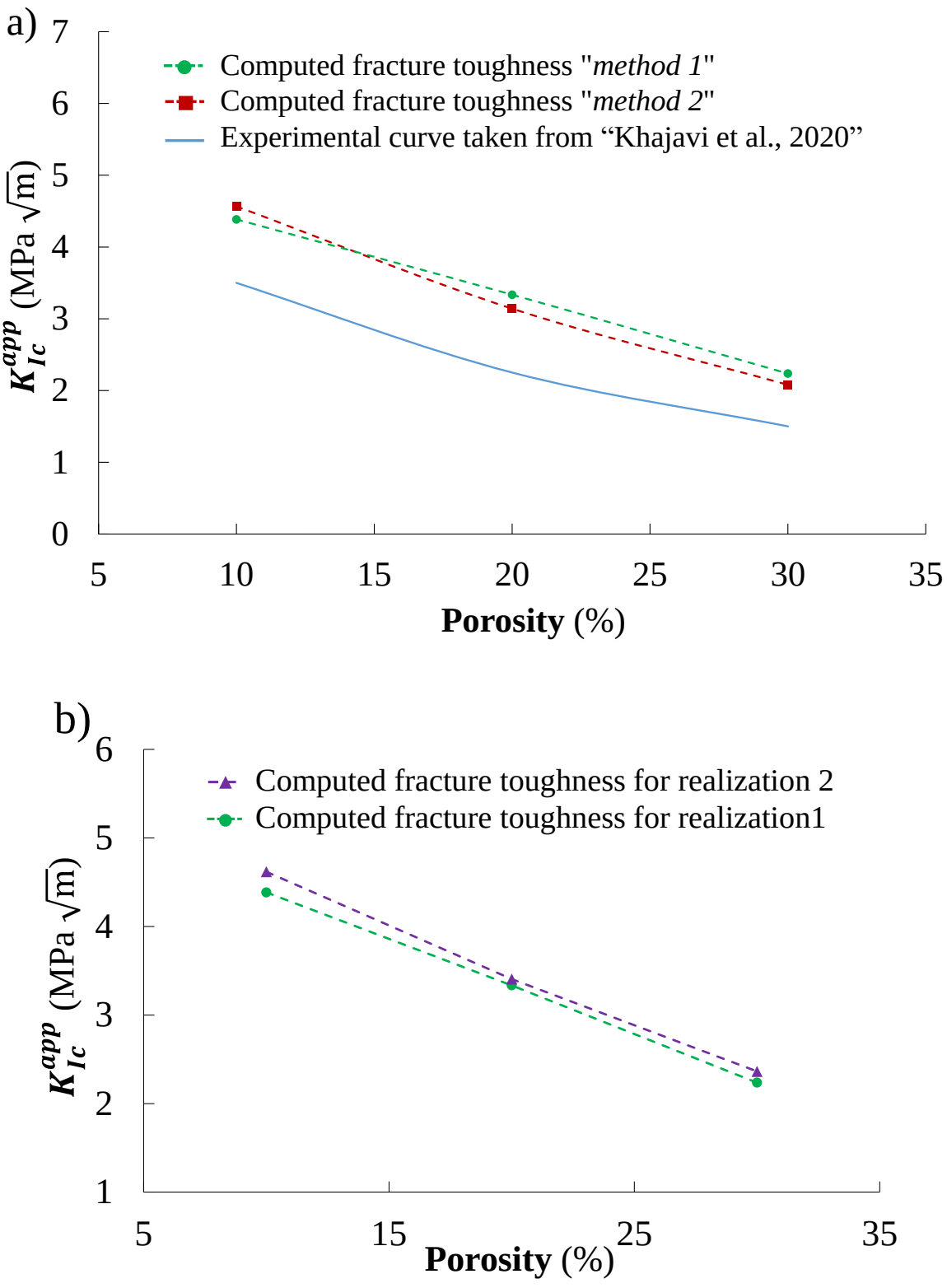

Fig IV- 6. Experimental and simulated dependences of the apparent fracture toughness on porosity using a) the two computation methods for realization 1, b) "method 1" for the two realizations.

In Fig. IV-6a, it can be noticed that the first method to compute the apparent fracture toughness leads to slightly higher K_{Ic}^{app} compared to the second one at ε = 20% and 30% and lower K_{Ic}^{app} at 10%. These results can be interpreted by inspection of the cartographies displaying the crack path within the microstructure in Fig IV-4. For instance, at ε = 20%, it can be noted that the preexisting macro-crack ends in a large pore (Fig. IV-4a). Due to the blunting effect induced by this large cavity, the first method thus yields higher apparent toughness. On the contrary, after propagation, the crack reaches a smaller pore. Therefore, the apparent toughness for the crack re-initiation from this smaller cavity is lowered knowing that the other conditions affecting the fracture remains roughly similar. Indeed, the direction of propagation remains in a quasi-pure opening mode, and the length of the ligaments between the first and second pores and between the second and third pores is almost identical (Fig. IV-4a) [67]. At the lowest porosity (ε = 10%), the initial macro-crack tip is located in the 3YSZ solid phase (Fig. IV-4c). Therefore, in this particular case, the crack tip is no longer blunted by a cavity explaining the lower value of K_{Ic}^{app} obtained with the first method with respect to the second one. Moreover, it can be noticed that the direction of propagation remains similar (only the length of the ligaments between the initial macro-crack tip and the first pore and between the first and second pores is changed).

IV.2.2. Fracture of porous ceramic microstructures under compression

IV.2.2.1. Dependence of the compressive fracture strength on the porosity

To study the crack nucleation in pristine porous ceramics, the compressive fracture strength measured in [161] (*cf.* chapter II) as a function of porosity for 8YSZ has been calculated with the PFM model. The simulations have been conducted on 3D microstructures according to the methodology detailed in section IV.1.2. Two values of the length scale parameters ℓ = 0.4 µm and ℓ = 0.8 µm have been considered for the computations.

The calculated compressive fracture strength is compared to the experimental data as a function of porosity in Fig. IV-7. It can be seen that the numerical predictions are in very good agreement with the measurements. Especially at ℓ = 0.8 µm, the model captures closely the decease of the fracture strength with the porosity. This result confirms that, with a single regularization parameter, the phase field method is also able to predict accurately the crack nucleation in partially sintered ceramics. Therefore, for a given type of microstructure for which the regularization parameter has been identified, the phase-field approach can be seen as a

predictive tool to study the fracture behavior of pristine microstructures. In other words, as already discussed on ideal geometries, the length scale parameter must be identified and assigned to contain the material properties so that the phase field model can be used to predict the fracture in complex porous microstructures.

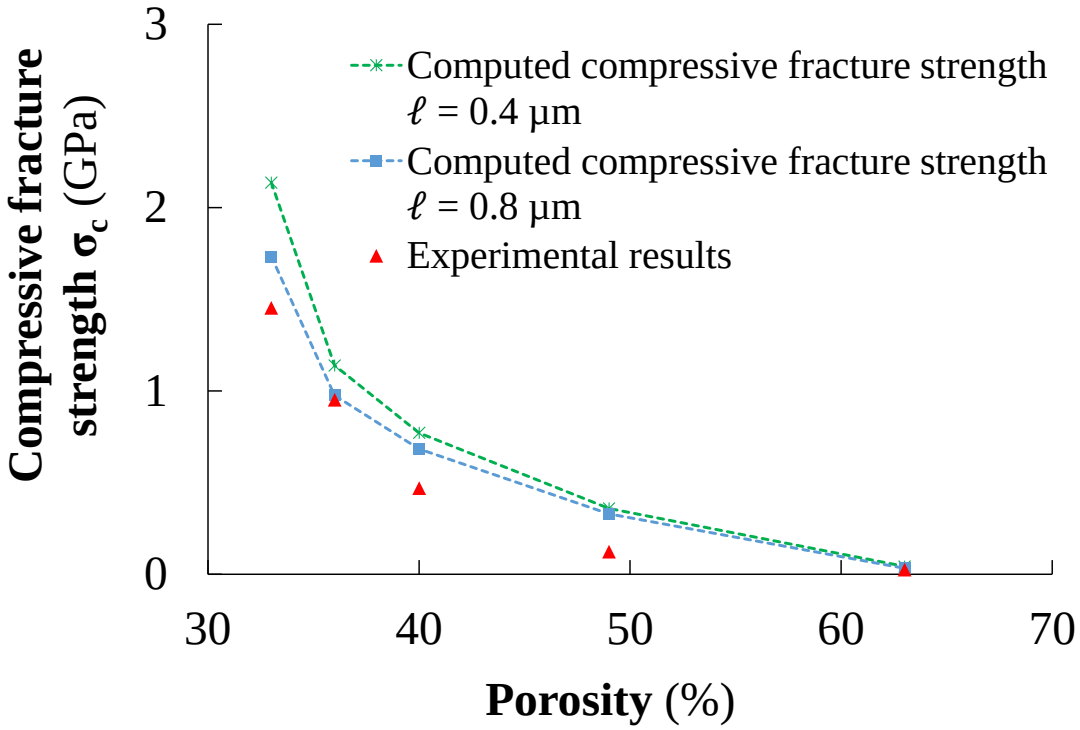

Fig IV- 7. Comparison between the calculated compressive fracture strength and the experimental data [161] as a function of porosity.

IV.2.2.2. Change in the fracture behavior with porosity: brittle behavior towards diffuse damage

In the second chapter, it has been shown that a transition in the fracture mechanism was detected in the micro-compression tests [161]. Indeed, at low porosity, the fracture was found controlled by a pure brittle behavior whereas a diffuse damage with the generation of stable micro-cracks in the microstructure was observed at high porosity. The results in the previous sections indicate that this change in behavior regime is well predicted by the PFM model and can be thus analyzed in further details with the simulated results obtained on the 3D volumes Fig. IV-8.

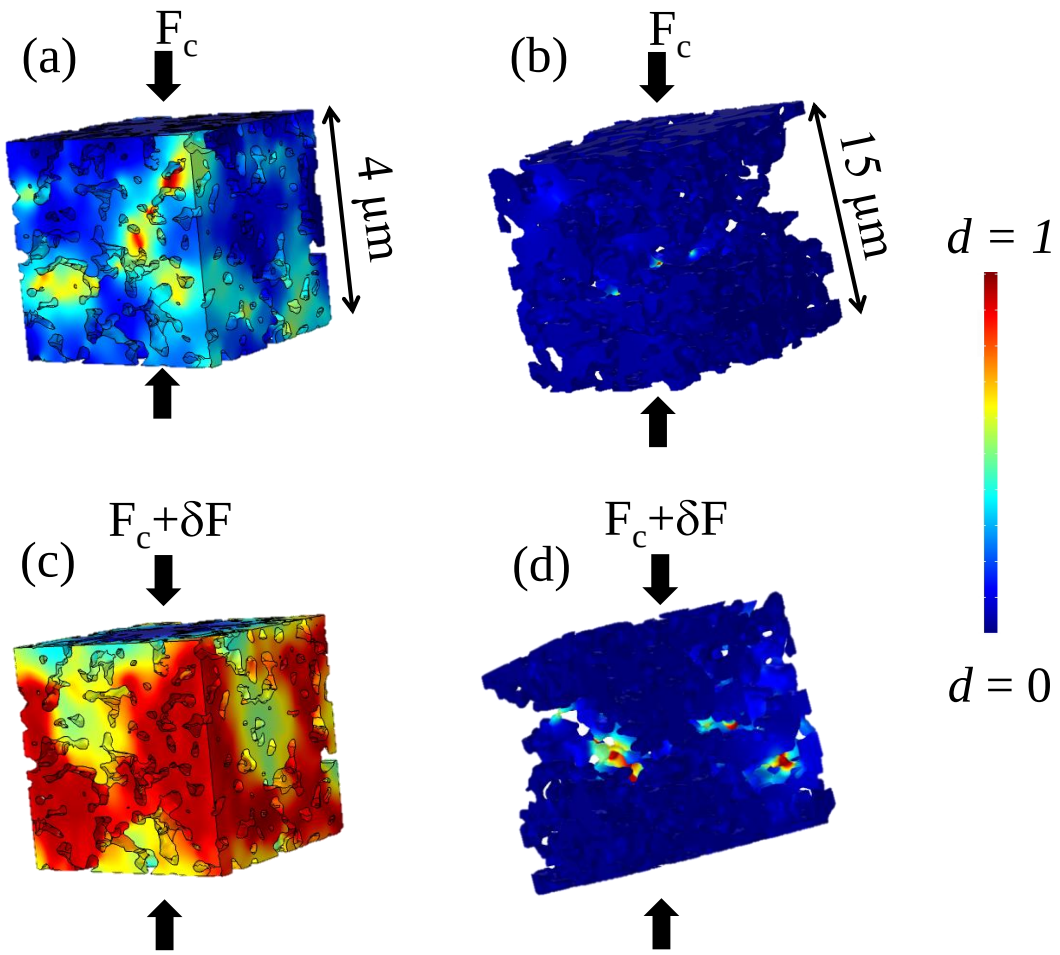

Fig IV- 8. Visualization of the cracks created in porous microstructures submitted to compression: First micro-cracks created in the microstructure with a porosity of a) 33 % and b) 63 %. Evolution of the damage variable after a small increment of charge at c) 33 % and d) 63 % (ℓ = 0.4 µm).

For instance, as shown in Fig. IV-8a-b for a porosity of 33%, the apparition of the first crack in the microstructure is almost instantaneously followed by the complete damage of the whole microstructure. Indeed, the first cracks are detected in the volume for an applied force on the micro-pillar of 6.04 N (Fig. IV-8a). Then, for a small increment in charge (less than 25%), the damage variable takes a value of d = 1 in the whole simulated domain indicating the total fracture of the specimen. Therefore, as soon as the first cracks are initiated in the volume, they lead to the complete fracture of the material as observed during the micro-mechanical experiments (*cf.* chapter II). It can be also noticed that the first micro-cracks are roughly aligned and parallel to the direction of the applied solicitation as detected during the tests (*cf.* chapter II). On the contrary, for the highest porosity, the simulation predicts the formation of a network of stable micro-cracks distributed in the microstructure during the loading (Fig. IV-8c-d). As

shown in FigIV-8c, the first micro-cracks appear at an applied force of 0.09 N. Then, the density of cracks is progressively increased during the loading. The repartition of micro-cracks in the volume is for example shown in Fig. IV-8d at an applied force of 0.16 N. The total collapse arises only when the load is increased up to 0.17 N. These results, which are in good agreement with the experiments, constitutes a further proof of the relevance of the phase approach to calculate accurately the fracture initiation in complex porous ceramics.

The modeling results have been used to analyze this transition in the fracture mechanism as a function of the porosity. For this purpose, the density of elastic strain energy ξ stored in the solid phase of the microstructure has been extracted just before the first crack nucleates in the volume:

$$\xi = \frac{1}{V_{YSZ}} \int_{V_{YSZ}} \Psi dV \qquad \text{(IV-1)}$$

Where V_{YSZ} is the volume of the solid phase.

The plot of the density of energy as a function of the porosity (Fig. IV-9a) shows a strong decrease of the strain energy with increasing porosity.

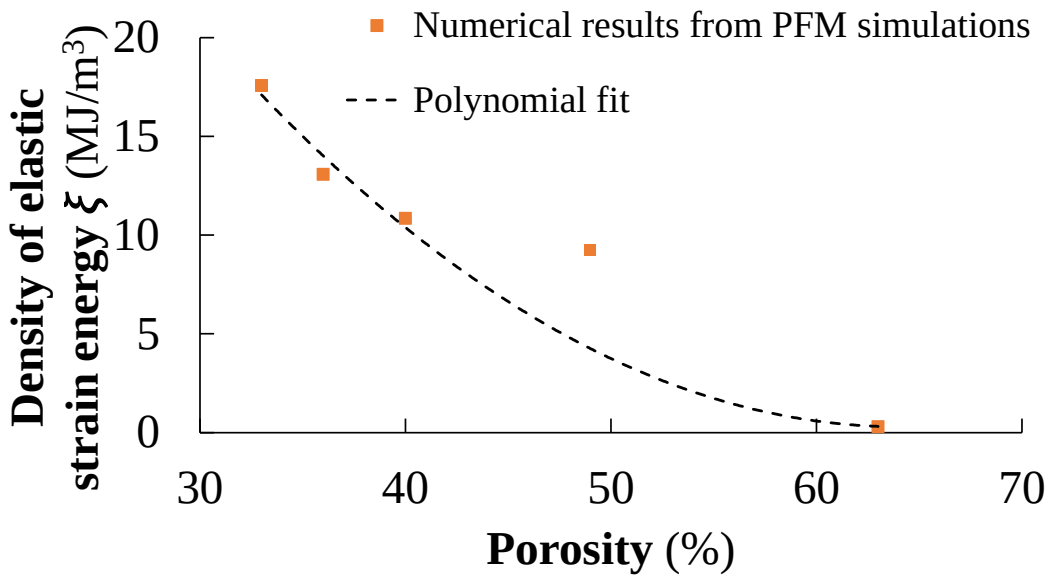

Fig IV- 9. Evolution of the density of elastic strain energy as a function of porosity (ℓ = 0.8 µm).

The high stored energy at low porosity should thus constitute the driving force to propagate the first nucleated micro-cracks to the whole microstructure explaining the brittle behavior of the ceramic. At the opposite, for the highly porous material, the stored energy becomes insufficient to ensure the propagation to the whole specimen. In this condition, the fracture proceeds as a diffuse damage as shown by the modeling and experimental results.

Moreover, the mean value of the local maximum principal stress, which was taken in the ligament where the first crack appears, has been also retrieved from the simulated data just before the fracture (*i.e.* the loading step corresponding to the time when the stress is the highest in the ligament before relaxation due to the fracture). It can be noticed that this first principal stress is in traction. Indeed, due to the complexity of the microstructure loaded under a macroscopic compression, some parts of the ceramics are submitted to a bending moment leading to local tensile stress. It is worth noting that this local tensile stress triggering the fracture is roughly equal to 4 GPa whatever the investigated porosities (33 %-63 %). This high value could be consistent with the apparent fracture strength of the 8YSZ ceramic when considering the very small volume of the ligament submitted to the tensile loading [113,162].

As for the ideal 2D geometries, the above discussion shows that the phase-field model is able to capture a change in the fracture criterion after adequate identification of the regularization parameter. For a porous ceramic loaded under compression, it enables explaining the observed transition in the fracture mechanism from a brittle towards a diffuse damage behavior. From all these results, the phase-field model appears as a relevant tool to quantify the crack nucleation in porous ceramics but also to analyze the underlying mechanisms controlling the fracture.

IV.3. Conclusion

The relevance of the PFM model for simulating the crack nucleation and propagation in real porous ceramic microstructures has been assessed. The conditions for the propagation of a pre-existing crack have been computed with the phase-field method on 2D synthetic microstructures with porosities ranging from 10-30%. A unique length scale parameter has been identified in such a way that the evolution of the apparent fracture toughness is in good agreement with a published experimental dataset for a 3YSZ ceramic over the whole porosity range. Moreover, the conditions of crack re-initiation from pore-solid interfaces during the propagation has been discussed in the light of local microstructural parameters (*i.e.* pore size, length of the ligaments between the pores and direction of propagation). These statements extend the results on ideal

geometries in chapter three to 2D porous ceramic microstructures, confirming that the phase-field method is able to predict accurately the fracture toughness of porous brittle materials after calibration of the regularization parameter.

The fracture initiation in uncracked porous ceramics have been studied on real 3D microstructures. For this purpose, the compressive fracture strength has been computed with the PFM model for 8YSZ with porosities ranging from 33% to 63%. For a single length scale parameter, it has been found that the compressive strengths computed as a function of the porosity are in very good agreement with the micro-mechanical testing data on 8YSZ presented in chapter two. Besides, it has been shown that the model predicts the transition from a brittle behavior at low porosity towards a diffuse damage at high porosity that was observed during the experiments. This change in the fracture mechanism has been analyzed with the model. It has been shown that this transition is related to the elastic strain energy stored in the microstructure. At low porosity, the excess of strain energy allows the unstable crack propagations in the whole specimen. Conversely, at high porosity, the strain energy is insufficient to propagate the nucleated micro-cracks to the whole microstructure. All these results show that the PFM method is a relevant tool to study the fracture behavior of the porous ceramics.

The present chapter concludes the core model developments and validations performed in this thesis. For the SOCs application, the fracture of the YSZ skeleton induced by the Ni re-oxidation within the hydrogen electrode can be therefore simulated using the PFM approach. For this purpose, an extension of the PFM model is first needed to simulate the Ni volume expansion during its re-oxidation. In the fifth chapter, the simplified modeling approach of the Ni re-oxidation and its implementation in the existing model are detailed. 3D reconstructions of two typical cermet supports (Ni-8YSZ and Ni-3YSZ) are considered for the simulations. The numerical results are analyzed and the impact of the microstructural properties on the redox mechanical stability is discussed.

V. Simulation of the mechanical damage in the hydrogen electrode induced by Ni re-oxidation

As presented in the first chapter, because of system component failures in operation causing for instance the re-introduction of air during the system shutdown, the Ni in the cermet is liable to re-oxidize. It has been shown that the Ni re-oxidation is one of the most detrimental issue regarding the SOC durability. Indeed, the Ni swelling upon its re-oxidation generates high tensile stresses in the YSZ skeleton leading to the formation of micro-cracks and alterations of the Ni phase after re-reduction, therefore to a degradation of the overall cell performances [40,54,163].

In this context, a predictive numerical tool of the YSZ skeleton micro-cracking of the hydrogen electrode is of high interest to design better microstructures. For this purpose, the results presented in the previous chapters highlight the phase-field model as a relevant and powerful candidate approach to simulate the electrode mechanical damage. Indeed, the relevance of the PFM model to accurately predict the crack initiation and propagation in real porous ceramic

microstructures has been confirmed up to the three-dimensional case. The model was shown able to retrieve the compressive fracture strength as well as the apparent toughness of the porous YSZ samples as a function of the porosity. It is to be noted that the compression testing of porous YSZ specimens generates complex local stresses in the microstructure and the fracture occurs in the regions subjected to tensile stresses. Accordingly, as the model has shown its efficiency for the micro-compression testing, it should be relevant to study the fracture of the YSZ skeleton, within the hydrogen electrode, induced by Ni re-oxidation.

This chapter is thus devoted to the simulation of the micro-cracks induced by the Ni re-oxidation using the PFM model. Firstly, the assumptions for the modeling of the Ni re-oxidation are described and the numerical implementation is detailed. In order to assess the impact of the material and microstructural properties on the cermet mechanical robustness during Ni re-oxidation, the study has been conducted considering two different Ni-3YSZ and Ni-8YSZ cermets. For this purpose, 3D reconstructions by X-ray tomography of the two studied electrodes have been performed. The investigated microstructures have been characterized by calculating a set of properties allowing to assess their role on the critical degree of oxidation. For the PFM simulations, volumes of 5^3 µm^3, representative of the cermet microstructure, have been considered and the value of the length scale parameter ℓ has been chosen, for each microstructure, based on the results of the previous chapters. Finally, the critical degree of oxidation has been calculated and the impact of the microstructural properties has been discussed.

V.1. PFM-based model to simulate the fracture induced by Ni re-oxidation

V.1.1. Ni re-oxidation modeling

As discussed in the first chapter, a significant volume expansion of the Ni particle occurs during the re-oxidation (*cf.* chapter I section I.6.1.2). In the present work, the Ni swelling has been modeled as a thermal dilatation. Therefore, the Ni re-oxidation is assumed geometrically driven without additional creation of contact between the Ni and YSZ phases. In other words, this approach is a simplification of the real situation. The large decrease of porosity, non-homogeneities, phase transformation and re-distribution related to the location of the reaction front during the growth of the NiO particles are in particular not considered. This hypothesis is however considered reasonable during the early stage of Ni re-oxidation, which is actually the

first priority to advance the current understanding of mechanical damage upon Ni re-oxidation. The Ni swelling has been thus calculated in the model through a thermal dilatation as follows:

$$\bar{\bar{\varepsilon}}_{th} = \alpha_{th}(T - T_{ref}) \quad \text{(V-1)}$$

where $\boldsymbol{\alpha_{th}}$is the thermal expansion coefficient for the Ni phase. This coefficient has been taken constant implying that the re-oxidation reaction rate is treated as completely homogeneous at both the scale of Ni/NiO phase and whole microstructure. This hypothesis is here considered as reasonable when the temperature is lower than around 750°C [164,165] (*cf.* Chapter I section I.6.1.1). It is worth noting that the fictive thermal expansion coefficient for Ni has been taken arbitrarily equal to 9×10^{-6} K^{-1} while the coefficient for the YSZ phase has been set to a small value to avoid the dilation of this phase during the simulations (Table V-1). The temperature difference ($\boldsymbol{T - T_{ref}}$) has been then used to control the thermal strain $\bar{\bar{\boldsymbol{\varepsilon}}}_{\boldsymbol{th}}$ to reproduce the Ni target volume expansion.

Table V- 1. material properties used for the simulations.

Material properties	Ni	8YSZ	3YSZ
E [GPa]	190	216	214
ν [-]	0.31	0.31	0.31
G_c [J/m^2]	3000	10.85	109.86
α_{th} [K^{-1}]	9×10^{-6}	0.001×10^{-6}	0.001×10^{-6}

V.1.2. Implementation description

It is worth noting that only a thermal loading has been applied to simulate the Ni dilatation without adding any supplementary mechanical boundary conditions in the PFM model. Indeed, the simulations have been performed under the self-equilibrating condition proposed by Comsol Multiphysics® software so-called "rigid motion suppression". In addition, it is to be noted that the contact between the Ni and YSZ phases has been maintained during simulations ensuring that the two phases cannot penetrate in each other.

V.1.3. Methodology

The PFM simulations have been conducted considering two volumes of 5^3 µm^3 taken from 3D reconstructions of two typical cermet supports. The first volume was made of Ni-8YSZ while the second was made of Ni-3YSZ. It is to be noted that the cermet supports used in this study

are different from those tested under micro-compression in chapter two. The material properties of the solid phases used in the simulations (*i.e.* YSZ and Ni) are reported in Table V-1. The two volumes have been meshed using Avizo® software (Fig. V.1). The mesh for the solid phases is composed of around 6.5×10^6 (14×10^6) and 8.5×10^6 (23×10^6) tetrahedral elements for the Ni-8YSZ and Ni-3YSZ cermets, respectively.

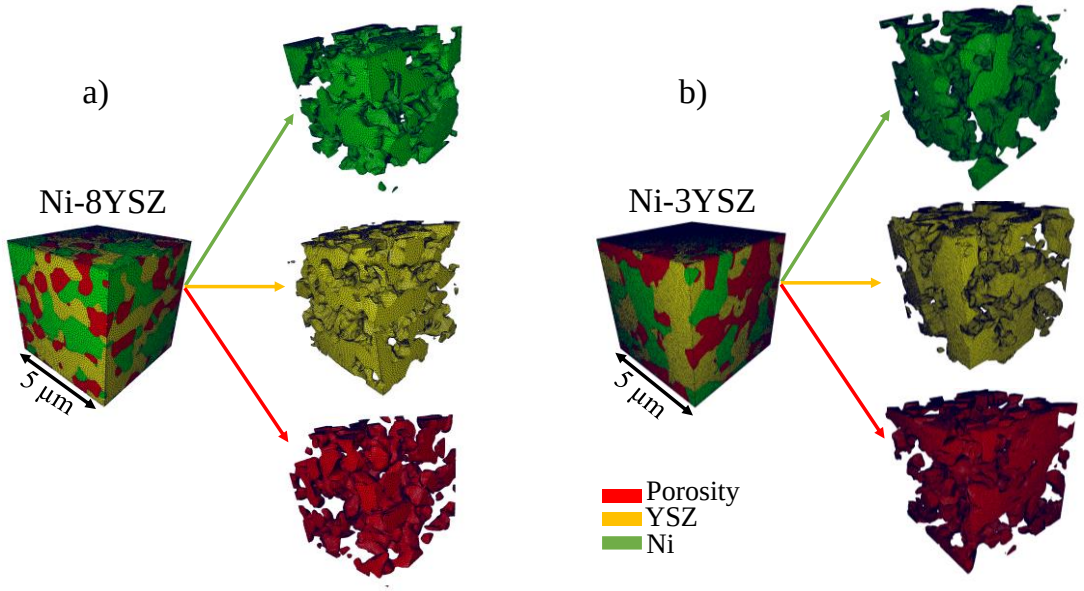

Fig V- 1. Meshes of the computation domain illustrated for the total volume and for each phase separately: a) Ni-8YSZ, b) Ni-3YSZ.

A complementary study has been conducted considering sub-volumes of 2^3 µm^3 extracted from the whole 5^3 µm^3 mesh in order to better visualize and thus analyze the crack onset in the microstructure.

The length scale parameter ℓ used in the PFM simulations has been chosen based on the results of the third and fourth chapters. Indeed, the validation with the micro-compression experiments, reported in the fourth chapter, has enabled to identify the length scale parameter for the porous 8YSZ ceramic (ℓ_{8YSZ} = 0.4 µm). Moreover, it has been found that the ratio between the length scale parameters of the two materials 8YSZ and 3YSZ is equal to $\frac{\ell_{3YSZ}}{\ell_{8YSZ}}$ = 1.4 for the simplified geometry of the crack blunted by a cavity (*cf.* chapter III). As a result, to simulate the fracture of the YSZ skeleton induced by Ni re-oxidation, the PFM simulations have been carried out using ℓ_{8YSZ} and ℓ_{3YSZ} equal to 0.4 µm and 0.6 µm, respectively. According to the results reported in chapter III, it is worth noting that these two length scale parameters (with $\ell_{8YSZ}>\ell_{3YSZ}$) take into account the difference in the material fracture properties (both

toughness and strength) between the 3YSZ and 8YSZ material to predict correctly the crack nucleation (*cf.* Table III-1 in chapter III). Finally, the critical degree of oxidation triggering the YSZ fracture has been identified and the impact of the material and microstructural properties has been discussed.

V.2. Results and discussion

V.2.1. Microstructural properties

The difference between the investigated microstructures has been first quantified by computing a set of properties on the two 3D reconstructions (Ni-8YSZ and Ni-3YSZ). The calculated volume fractions, phase mean diameters and percolations of the phases are summarized in Table V-2.

Table V- 2. Microstructural properties of the Ni-8YSZ and Ni-3YSZ cermet supports computed on 3D reconstructions.

Material	Ni-8YSZ cermet			Ni-3YSZ cermet		
Phase	Ni	8YSZ	Porosity	Ni	3YSZ	Porosity
Volume fraction ε [%]	37	38.2	24.8	29	40	31
Phase mean diameter [µm]	0.49	0.37	0.31	0.43	0.39	0.35
Percolation [-]	0.99	0.99	0.9	0.98	0.99	0.86

For the Ni-8YSZ microstructure, the PSD plots of the different phases are displayed in FigV-2a. The density for the porous phase is nearly symmetric while a dissymmetry is observed in the distribution of the solid phases especially for the Ni phase. Moreover, the microstructure is characterized by a wide size distribution for the Ni solid phase due to the presence of bigger particles. Indeed, the mean diameter of the Ni phase has been found equal to 0.49 µm while it was equal to 0.31 µm and 0.37 µm for the porosity and 8YSZ, respectively.

Regarding the Ni-3YSZ microstructure, it can be noticed that the PSD of the porosity has an approximately symmetric shape, while the PSD of the solid phases present a wider distribution (Fig.V-2b). Indeed, a mean diameter of 0.35, 0.39, and 0.43 has been calculated for porosity, 3YSZ and Ni, respectively.

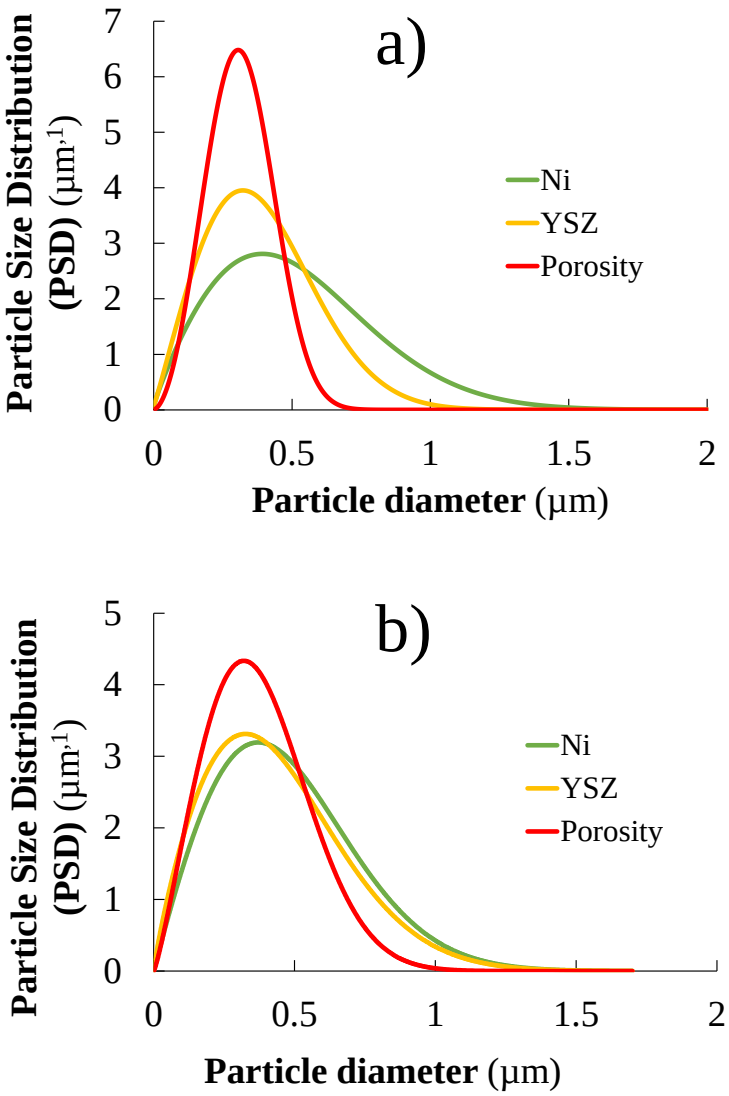

Fig V- 2. Particle size distribution (PSD) of: a) Ni-8YSZ and b) Ni-3YSZ microstructures.

The comparison between the two microstructures highlights a similarity in the distribution of the different phases. In both cases, the porosity is characterized by a quite symmetric distribution while a dissymmetry is observed in the case of the solid phases. In addition, the mean diameter of porosity is smaller than YSZ which is smaller than Ni. However, many differences between the investigated microstructures are detected. Firstly, the repartition of phases volume fraction changes from a microstructure to another (*i.e.* $\varepsilon_{pore}<\varepsilon_{Ni}<\varepsilon_{8YSZ}$ for Ni-8YSZ while $\varepsilon_{Ni}<\varepsilon_{pore}<\varepsilon_{3YSZ}$ for Ni-3YSZ). It has been found that the Ni-3YSZ cermet has a higher porosity and less Ni than the Ni-8YSZ material. Indeed, a porosity of around 31 % and 25 % has been measured for the Ni-3YSZ and Ni-8YSZ cermet supports, respectively.

Moreover, the comparison between the two microstructures reveals that the Ni-3YSZ has a higher pore mean diameter. Therefore, the Ni phase of the Ni-3YSZ should have more space to expand into porosities upon re-oxidation than in the Ni-8YSZ cermet. Furthermore, Ni-3YSZ is characterized by a larger 3YSZ mean diameter (0.39 µm) and smaller Ni particles (0.43 µm) as compared to Ni-8YSZ cermet (*i.e.* with phase mean diameter of 8YSZ and Ni of 0.37 µm and 0.49 µm, respectively). These properties are expected to play a key role on the mechanical stability of the YSZ skeleton within the cermet. Intuitively, a cermet exhibiting small Ni particles and a large mean diameter for the YSZ phase is expected able to better withstand the Ni-reoxidation before the formation of micro-cracks in the YSZ skeleton. The differences noted in the microstructural characteristics between the two investigated volumes are thus expected to affect the mechanical behavior, hence the cermet mechanical stability upon Ni re-oxidation mechanism. This is discussed, in the next section, based on the results of the phase-field simulations.

Finally, it is to be noted that the percolation for the solid phases in both microstructures was found to exceed 0.98 thus showing the relevance of the size of the studied volume (5^3 µm^3). In addition, the microstructure representativeness is ensured as the threshold rule, which is approximately fixed to 10 times the mean diameter of the largest phase, is fulfilled. Indeed, the volume edge (5 µm) is more than 10 times the mean diameter of the different phases (Table V-2).

V.2.2. Results of the PFM simulations

As mentioned before, the PFM model has been firstly applied on sub-volumes of 2^3 µm^3. The visualization of the cracks created in the microstructures are shown in Fig.V-3. It can be seen that the PFM model is able to simulate the fracture of the YSZ skeleton induced by the Ni volume expansion. As expected, the cermet microstructure failure occurs first by the formation of micro-cracks within the YSZ skeleton caused by the high tensile stress generated during the Ni re-oxidation. Indeed, it has been found that the regions, where the cracks occurred, are subjected to high tensile stress. Therefore, the model is able to retrieve the results observed during experiments. Moreover, it can be noticed that the first cracks have been created in YSZ ligaments surrounded by Ni and characterized by specific shape and characteristic length resulting in the generation of high tensile stresses during Ni re-oxidation. This indicates that the local fracture in the YSZ skeleton is strongly dependent on the microstructural properties of the cermet.

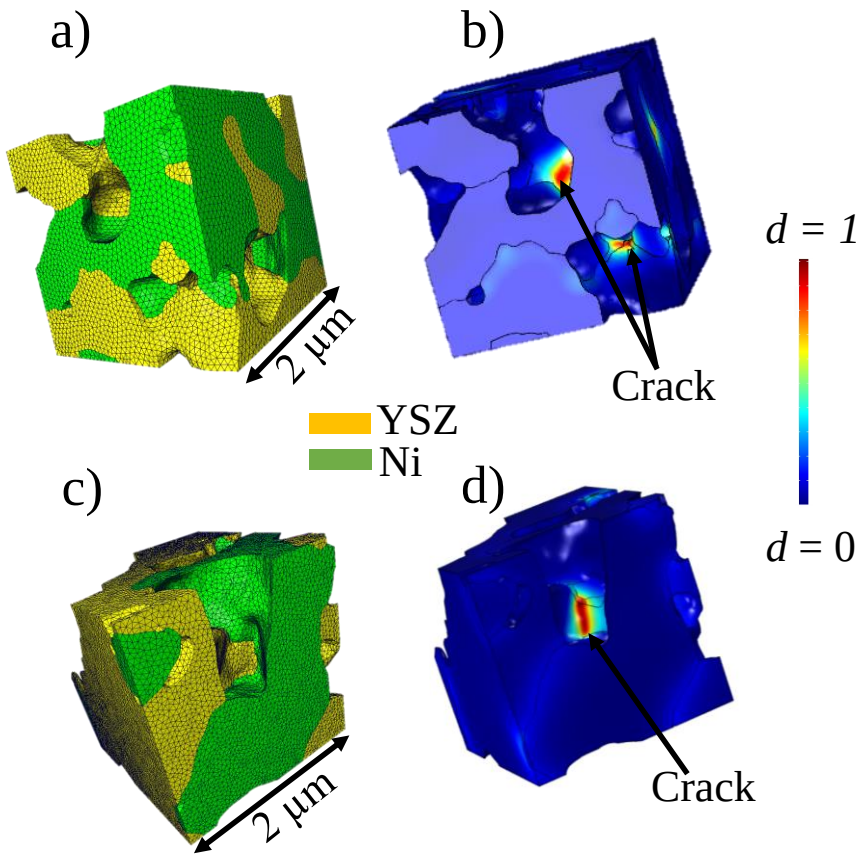

Fig V- 3. Meshes of the simulated Ni-YSZ volumes of 2^3 µm^3: a) Ni-8YSZ, c) Ni-3YSZ. Micro-cracks simulated by PFM in b) Ni-8YSZ, d) Ni-3YSZ at a critical degree of oxidation of 3% and 11%, respectively.

Besides, as mentioned in section V.1.1, the Ni swelling is directly obtained by the thermal expansion $\bar{\bar{\varepsilon}}_{th}$, as an assumption of homogeneous re-oxidation has been considered in the simulations. In addition, it has been shown in the first chapter that the complete re-oxidation of the Ni is reached for a volume expansion of 71.2 % [53,163]. Thus, a critical degree of the Ni re-oxidation can be calculated for the Ni volume expansion, which triggers the fracture within the YSZ skeleton. For the Ni-8YSZ microstructure, a Ni volume expansion of 2.1 % corresponding to a degree of oxidation DoO of 3% has been found to generate fracture in YSZ while the crack initiation in the Ni-3YSZ microstructure has been detected for a significantly higher Ni swelling of 7.4% (*i.e.* DoO of 11%). As foreseen, the model predicts that the mechanical stability of the Ni-3YSZ cermet upon the Ni re-oxidation is significantly higher than Ni-8YSZ cermet. This is an immediate consequence of the higher fracture properties inherent to the 3YSZ material. Moreover, the simulations have shown that the micro-cracks are created almost during the early stage of the Ni re-oxidation. This result is qualitatively in line

with experiments reported in the literature that have ascribed the observed loss in the cell performances to the formation of micro-cracks within the YSZ skeleton during the first stage of the Ni re-oxidation [40].

To go further in the analysis of the influence of the microstructural properties on the mechanical stability of the cermet, the PFM simulations have been then conducted on the total volumes of 5^3 µm^3 representative of the electrode microstructure. It can be noticed that the first cracks have been generated on YSZ ligaments different from the ones detected in the sub-volumes of 2^3 µm^3 (FigV-4). This statement is a further indication of the complexity of the fracture simulation in real 3D porous electrode microstructures where many morphological parameters are involved (*i.e.* distribution and characteristic length of the Ni, YSZ and porosity phases, etc.).

For the microstructures of 5^3 µm^3, the first cracks in the Ni-3YSZ and Ni-8YSZ have been initiated when the degree of Ni re-oxidation has reached a critical value of around 6.3% and 2%, respectively. As expected, the mechanical stability upon the Ni re-oxidation of 8YSZ is still much lower than 3YSZ. It is here estimated to be approximately 3 times less for 8YSZ when considering a homogeneous oxidation.

Furthermore, it is to be noted that the number of cracks in Ni-3YSZ is lower than in Ni-8YSZ microstructure. Indeed, only two cracks have been created in Ni-3YSZ while five cracks have been detected in Ni-8YSZ. Beyond the better fracture properties of 3YSZ, this statement could be also ascribed to the differences noted in the microstructural properties between the two investigated cermet supports. Indeed, the microstructure of the Ni-3YSZ (*i.e.* higher porosity, lower Ni phase volume fraction together with a larger 3YSZ phase volume fraction compared to the Ni-8YSZ) could reinforce the mechanical stability of this cermet upon Ni re-oxidation. This is in line with the results observed during experiments [40]. As mentioned in the first chapter, the microstructures with higher porosity have the advantage of higher mechanical stability upon Ni re-oxidation. In addition, the YSZ mean diameter of the 3YSZ-Ni cermet is larger compared to Ni-8YSZ cermet, that could also explain in part the lower micro-cracks number in equivalent volume size.

This ‘preliminary’ study points out that the higher mechanical stability simulated for the Ni-3YSZ cermet does not stem only from the better 3YSZ fracture properties, but most likely also from microstructural characteristics. For this reason, a special attention must be paid during the cermet microstructure manufacturing in order to guarantee a good mechanical stability of the hydrogen electrode upon the Ni re-oxidation.

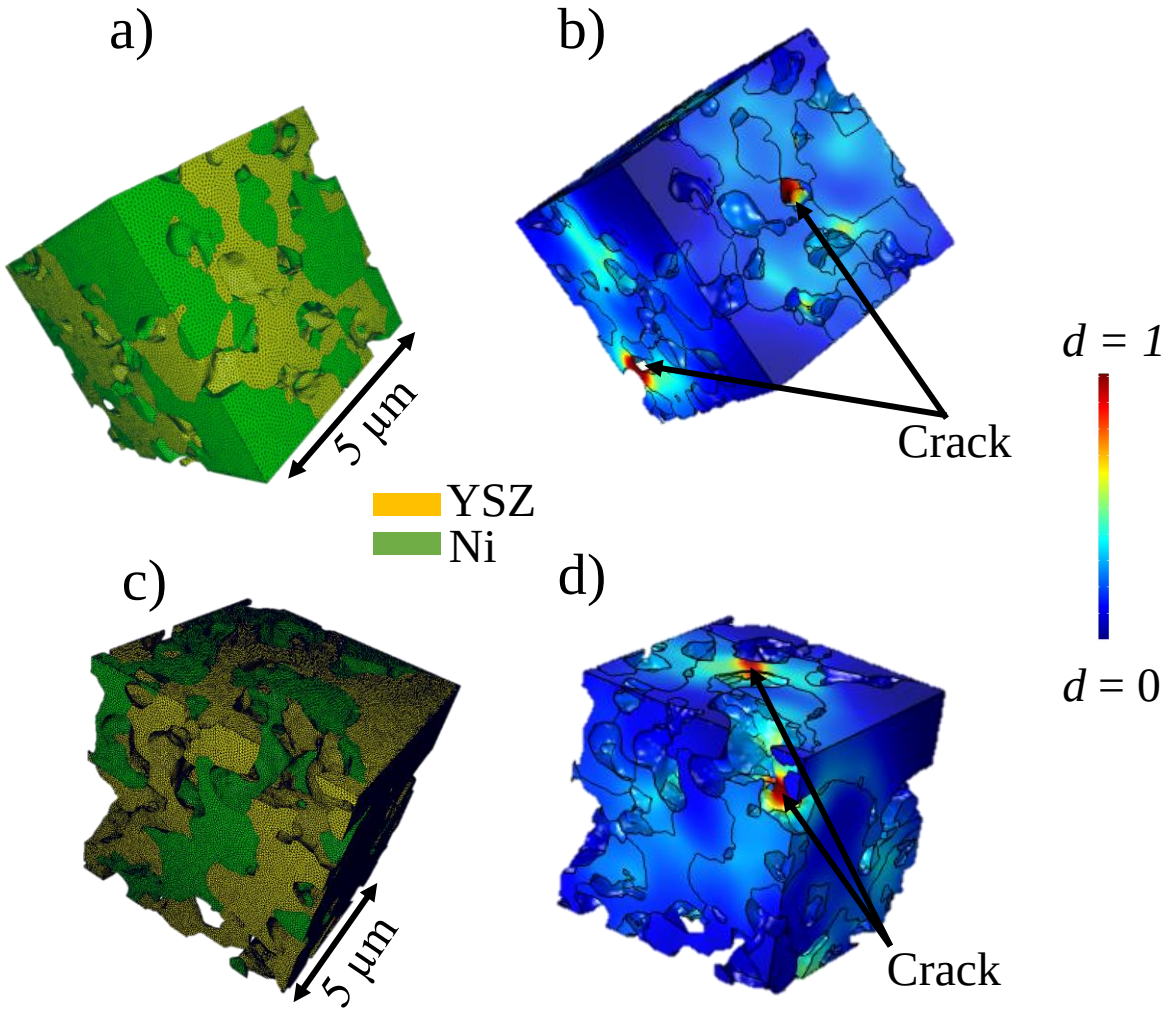

Fig V- 4. Meshes of the simulated solid phases in the Ni-YSZ volumes of 5^3 µm^3: a) Ni-8YSZ, c) Ni-3YSZ. Micro-cracks simulated by PFM in b) Ni-8YSZ, d) Ni-3YSZ.

To conclude, it is to be noted that experimental data are still needed to further validate the calculated critical degree of oxidation triggering the formation of micro-cracks within the YSZ skeleton. Moreover, the modeling of re-oxidation could be also improved to better describe the Ni/NiO transformation in the microstructure. Nevertheless, as anticipated, it can be claimed that the phase-field model appears as a powerful tool to simulate the fracture of the YSZ skeleton of the porous hydrogen electrode, thus enabling to analyze the impact of the material and microstructural properties on the porous electrode robustness. Accordingly, as the mechanical damage of the cermet can be numerically predicted, it should be possible to design Ni-YSZ microstructure with better redox tolerance along with high electrochemical performance, hence increasing the cell lifetime.

V.3. Conclusion

In this chapter, the PFM model has been applied to simulate the YSZ skeleton micro-cracking within the hydrogen electrode. In this 'preliminary' approach, the Ni swelling has been simulated through a fictive thermal expansion.

It has been confirmed that micro-cracks can appear during the early stage of the Ni re-oxidation. Moreover, it has been found that the micro-cracks are generated into the YSZ ligaments surrounded by Ni with specific morphological characteristics and submitted to high tensile stresses during the re-oxidation. In addition, the comparison between the investigated microstructures of two typical cermet supports (Ni-3YSZ and Ni-8YSZ) has confirmed the crucial role of the YSZ backbone. Indeed, the local fracture of the YSZ skeleton and the number of the created micro-cracks are strongly dependent on the fracture properties of the ceramic. As expected, it has been found that the Ni-3YSZ cermet has a higher redox tolerance with respect to Ni-8YSZ. Moreover, it has been also shown that the microstructural properties of the cermet can also play a role on the cermet mechanical stability. As observed during experiments, the microstructure with higher porosity and smaller Ni particles provides higher mechanical stability upon the Ni re-oxidation with the formation of less micro-cracks.

Thanks to the PFM model, it is thus possible to predict the mechanical damage of the hydrogen electrode as a function of its material and microstructural characteristics. Therefore, it becomes possible to accurately quantify the degradation in the cell performances induced by the formation of micro-cracks. As a consequence, the targeted microstructure fulfilling better redox tolerance can be identified, thus allowing to improve the cell lifetime.

VI. Conclusions and perspectives

This chapter synthesizes the main results of the thesis and present the perspectives for future studies.

Conclusions

The present work has been devoted to the development of a numerical tool to predict the fracture in real 3D porous ceramics such as SOC electrodes. For this purpose, the so-called phase-filed method (PFM) has been adopted. This model is based on an energy-stress criterion for crack nucleation and provides decisive advantages to take into account the characteristics of the complex electrode microstructures. Because of the lack of fracture properties data on porous Yttria-Stabilized Zirconia (YSZ), micro-mechanical characterizations have been carried out to provide experimental results for the model validation.

In this frame, a dedicated protocol has been proposed for testing in micro-compression porous ceramics with microstructures averaging the contribution of porous and solid phases in the

10−100 µm length scale. It spans from the specimen fabrication and testing up to post-mortem characterizations. Micro-compression tests were carried out on pillars of 60 µm in diameter, milled by plasma focused ion beam in porous YSZ pellets. The fracture properties were determined over a wide range of porosities (33%-63%) for 8YSZ and at a given pore volume fraction of 63% for 3YSZ. The Young's modulus was estimated as a function of the porosity from the unloading curve of tests stopped before fracture. The experiments conducted until the total fracture enabled measuring the compressive fracture strength, which was found to decrease when increasing the porosity. The decrease in strength with the pore volume fraction can be fitted according to a power law. Specimen tested and unloaded just before the total fracture were cross-sectioned by focused ion beam - scanning electron microscopy (FIB-SEM). A transition was detected from a brittle behavior, with macro-cracks parallel to the direction of solicitation, to a diffuse damage with micro-cracks, when increasing the porosity. It has been also shown that a size effect is not observed at high porosity (63%) according to the available data on macroscopic samples.

A dedicated study has been then performed to assess the relevance of the PFM model to accurately predict the crack initiation. For this purpose, a comparison was carried out on ideal geometries of stress singularity and stress concentration (*i.e.* V-notch and crack blunted by a cavity) between the PFM results and the predictions provided by the coupled criterion. The configuration of the crack blunted by a cavity was chosen as it can be seen as a first approximation of a porous media. For the two studied geometries, it was found that the PFM model is able to retrieve the coupled criterion results. In this frame, it has been established that the PFM model can capture the change in the fracture criterion when the length scale parameter ℓ is correctly chosen. Moreover, the nature of this parameter has been discussed showing that it contains information on the fracture properties but depends on the type of local geometry from which the crack initiates. Therefore, in addition to its energetic formulation, the PFM model can be seen as an energy-stress criterion based method through the length scale parameter ℓ. For the two types of studied geometry, it has been also found that the ratio between the length scale parameters for the two ceramics (8YSZ and 3YSZ) is equal to the ratio of the characteristic lengths related to the coupled criterion.

Once the capacity of the PFM model to accurately predict the crack initiation on ideal geometries was confirmed, its relevance to predict the fracture in real porous ceramic microstructures was addressed. Indeed, the apparent fracture toughness was simulated as a function of porosity considering porous 3YSZ microstructures with porosity ranging from 10%

to 30%. A good agreement with published experimental data was obtained. Besides, to validate the simulation of fracture in uncracked microstructures, a multi-scale approach to model the uniaxial compression testing on micro-pillars was implemented. The comparison with the experimental results showed that the PFM model is able to retrieve the compressive fracture strength as a function of porosity as well as the transition from a brittle behavior towards a diffuse damage when increasing porosity. As a consequence, it was claimed that the PFM model is a powerful tool enabling to better understand the underlying mechanisms of fracture in porous ceramics. To the best of our knowledge, it is the first time that the fracture is simulated in real 3D porous ceramic microstructures with a model able to reproduce correctly the experimental data.

As an illustration of the capability of the PFM model to study the porous electrodes mechanical damage for solid oxide cell application, the YSZ skeleton micro-cracking induced by the Ni re-oxidation was simulated. As a 'preliminary' approach, a thermal analogy was adopted to model the Ni volume expansion upon re-oxidation. The critical degree of oxidation was calculated considering two typical cermet microstructures (Ni-3YSZ and Ni-8YSZ). As expected, the micro-cracks were created during the early stage of Ni re-oxidation. Moreover, it was found that the Ni-3YSZ cermet offers a better Ni re-oxidation tolerance thanks to its higher fracture properties compared to the Ni-8YSZ material. The impact of the microstructural properties on the critical degree of re-oxidation and the density of micro-cracks was also discussed. As expected, small Ni particles, higher porosity and larger YSZ particles were found to be advantageous for the cermet mechanical stability during re-oxidation. Accordingly, the PFM model appears as an efficient tool to analyze the effect of the material and microstructural properties on the cermet redox tolerance and, more generally, on the mechanical robustness of porous ceramic-based electrodes.

Perspectives

In this work, it has been shown that the PFM approach is a relevant tool to study the fracture in real 3D porous ceramic microstructures. However, some improvements could be still envisaged such as testing new functionals [151] in order to attenuate the dependence of the model on the length scale parameter ℓ and therefore the material softening effect. Moreover, complementary studies are still needed to conclude the discussion on the nature of ℓ. For instance, it could be useful to study the case of the crack blunted by an ellipse instead of a cavity for different

materials, by keeping the same strategy as the one adopted in this work (i.e. comparison of the PFM results with the predictions provided by the coupled criterion). Therefore, in addition to the size effect analysis reported in this work considering a spherical pore, the shape effect on the choice of ℓ will be discussed when considering different geometries for the ellipse. According to the statements presented in this thesis, it is expected that the length scale parameter ℓ would depend on the shape of each ellipse. In other words, it should be possible to identify a single value of ℓ able to accurately predict the crack initiation as a function of the pore size only when the eccentricity of the studied ellipse is fixed. From this analysis, it would be interesting to draw the conditions that control the value of ℓ for example in terms of loading ahead a pore.

The PFM model was found efficient to analyze the impact of the material and microstructural properties on the fracture behavior. Nevertheless, there is still a serious lack of data on porous ceramics. As mentioned in the second chapter, it was not possible to thoroughly assess the size effect on fracture properties as the compressive fracture strength of porous 8YSZ is still not available on macroscopic samples for the intermediate porosities (33%-49%). Besides, using the developed protocol detailed in the second chapter, it would also be interesting to measure at the microscopic scale the compressive fracture strength as a function of porosity of different ceramics such as 3YSZ. Subsequently, the implemented multi-scale approach could be applied and a precise choice of the *ad hoc* length scale parameter ℓ for the PFM simulations could be identified to reproduce the experimental results. These additional studies would also bring new insights to interpret the nature of the length scale parameter ℓ when considering same types of microstructure.

Furthermore, because of the complexity of real 3D porous ceramic microstructures, the influence of different microstructural characteristics on the fracture properties cannot be easily decorrelated while the underlying mechanisms as well as the main activated fracture criterion remain difficult to analyze. For a better understanding of the fracture mechanisms in porous ceramics, it could be worth to study the fracture by modifying in a stepwise approach a single parameter of the porous media and to assess its effect. With this objective, PFM model should be applied on ideal 3D synthetic geometries in which the microstructural features are well defined and controlled (array of spheres for instance). It is expected to be able to establish relevant relationships between the length scale parameter ℓ and the morphological properties if experimental data are provided on ideal microstructures for validation. This study should thus allow estimating the *ad hoc* value of ℓ as a function of the computed microstructural properties.

Regarding the mechanical degradation of porous SOC electrodes, the PFM model is expected a powerful tool to simulate the mechanical damage induced by loadings such as thermal gradients, thermal cycling or redox cycling. Indeed, the study reported in the fifth chapter on the YSZ micro-cracking induced by Ni re-oxidation has confirmed the capacity of the PFM model to study the mechanical damage of porous SOC electrodes. Nevertheless, for this particular case, targeted improvements on the modeling of the Ni/NiO phase transformation would be necessary to not be limited to the first stage for a low degree of oxidation as assumed with the thermal dilatation analogy. In this frame, X-ray nanotomography is an appropriate technique to follow the microstructural evolutions as well as the micro-cracks formation during the Ni re-oxidation. Therefore, it should be possible to validate the modeling of the Ni/NiO phase transformation based on 3D reconstructions of the microstructure before and after the Ni re-oxidation [54]. In addition, experiments on Ni-8YSZ and Ni-3YSZ cermet supports with partial reoxidation will enable to characterize the evolution of micro-cracks distribution in the porous electrode (using electron and/or X-ray microscopy). The simulated results using the PFM model would be then validated based on the experiments and the *ad hoc* value of the length scale parameter ℓ will be identified. Besides, it has been shown that the PFM model can be used to assess the impact of the YSZ fracture properties and cermet microstructural characteristics on the electrode mechanical stability during Ni re-oxidation. Thanks to this approach, a sensitivity analysis could be performed to propose recommendations regarding the optimal microstructure and material fracture properties for a better redox tolerance.

For this optimization, it could be worth to assess the impact of the mechanical degradation during redox cycling on the overall cell performances. For this purpose, the PFM model should be coupled with the electrochemical multi-scale model developed at the laboratory [166] to quantify the loss in the electrode performances induced by the formation of micro-cracks within the YSZ skeleton. This multi-physic model will be then used for a sensitivity analysis by changing the cermet microstructure and YSZ material fracture properties (for instance by changing the yttrium doping rate). Accordingly, it will be possible to find a tradeoff for the cermet between its electrochemical performances and mechanical robustness.

To conclude, it is to be pointed out that a thorough study of the complex solid oxide cell technology is only ensured by adopting a threefold methodology, consisting of multi-scale and multi-physic modeling, microstructural characterization and electrochemical and mechanical experiments. In this case, relevant and efficient improvements of the solid oxide cell can be identified enabling its widespread commercialization.

References

[1] World Energy Outlook 2016 – Analysis - IEA, (2016). https://www.iea.org/reports/world-energy-outlook-2016.

[2] International Panel on Climate Change. Global Warming of 1.5°C., (2018). https://www.ipcc.ch/sr15/.

[3] World Energy Outlook 2018 – Analysis - IEA, (2018). https://www.iea.org/reports/world-energy-outlook-2018.

[4] K. Harris, Section 1: UK total energy, (2021) 56.

[5] Hydrogen Council, Https://Hydrogencouncil.Com/En/. (2021). https://hydrogencouncil.com/en/.

[6] H. Xing, C. Stuart, S. Spence, H. Chen, Fuel Cell Power Systems for Maritime Applications: Progress and Perspectives, Sustainability. 13 (2021) 1213. https://doi.org/10.3390/su13031213.

[7] S.C. Singhal, K. Kendall, High Temperature Solid Oxide Fuel Cells, Fundamentals, Design and Applications, Elsevier, 360 Park Avenue South, New York, NY 10010-1710, USA, 2003.

[8] M. Ni, M. Leung, D. Leung, Technological development of hydrogen production by solid oxide electrolyzer cell (SOEC), Int. J. Hydrog. Energy. 33 (2008) 2337–2354. https://doi.org/10.1016/j.ijhydene.2008.02.048.

[9] J.T.S. Irvine, P. Connor, Solid Oxide Fuels Cells: Facts and Figures, 1st ed., Springer, 233 Spring Street New York, NY 10013 USA, 2013.

[10] F. Monaco, M. Hubert, J. Vulliet, D. Montinaro, J.P. Ouweltjes, P. Cloetens, P. Piccardo, F. Lefebvre-Joud, J. Laurencin, Impact of Microstructure and Polarization on the Degradation of Ni-YSZ Electrode: An Experimental and Modeling Approach, ECS Trans. 91 (2019) 653–664. https://doi.org/10.1149/09101.0653ecst.

[11] Z. Zakaria, Z. Awang Mat, S.H. Abu Hassan, Y. Boon Kar, A review of solid oxide fuel cell component fabrication methods toward lowering temperature, Int. J. Energy Res. 44 (2020) 594–611. https://doi.org/10.1002/er.4907.

[12] H. Moussaoui, J. Laurencin, Y. Gavet, G. Delette, M. Hubert, P. Cloetens, T. Le Bihan, J. Debayle, Stochastic geometrical modeling of solid oxide cells electrodes validated on 3D reconstructions, Comput. Mater. Sci. 143 (2018) 262–276. https://doi.org/10.1016/j.commatsci.2017.11.015.

[13] V. Kharton, F. Marques, A. Atkinson, Transport properties of solid oxide electrolyte ceramics: a brief review, Solid State Ion. 174 (2004) 135–149. https://doi.org/10.1016/j.ssi.2004.06.015.

[14] S. Singhal, Advances in solid oxide fuel cell technology, Solid State Ion. 135 (2000) 305–313. https://doi.org/10.1016/S0167-2738(00)00452-5.

[15] E. Lay-Grindler, J. Laurencin, G. Delette, J. Aicart, M. Petitjean, L. Dessemond, Micro modelling of solid oxide electrolysis cell: From performance to durability, Int. J. Hydrog. Energy. 38 (2013) 6917–6929. https://doi.org/10.1016/j.ijhydene.2013.03.162.

[16] M. Ghatee, M.H. Shariat, J.T.S. Irvine, Investigation of electrical and mechanical properties of 3YSZ/8YSZ composite electrolytes, Solid State Ion. (2009) 6.

[17] C. Suciu, Physico-chemical properties of nanocrystalline YSZ powders as a function of doping level and electrical properties after sintering, (2018) 10.

[18] S.P. Jiang, Development of lanthanum strontium manganite perovskite cathode materials of solid oxide fuel cells: a review, J. Mater. Sci. 43 (2008) 6799–6833. https://doi.org/10.1007/s10853-008-2966-6.

[19] N.H. Menzler, F. Tietz, S. Uhlenbruck, H.P. Buchkremer, D. Stöver, Materials and manufacturing technologies for solid oxide fuel cells, J. Mater. Sci. 45 (2010) 3109–3135. https://doi.org/10.1007/s10853-010-4279-9.

[20] M.D. Anderson, J.W. Stevenson, S.P. Simner, Reactivity of lanthanide ferrite SOFC cathodes with YSZ electrolyte, J. Power Sources. 129 (2004) 188–192. https://doi.org/10.1016/j.jpowsour.2003.11.039.

[21] D.F. Sanchez, D. Grolimund, M. Hubert, P. Bleuet, J. Laurencin, A 2D and 3D X-ray μ-diffraction and μ-fluorescence study of a mixed ionic electronic conductor, Int. J. Hydrog. Energy. 42 (2017) 1203–1211. https://doi.org/10.1016/j.ijhydene.2016.11.094.

[22] G.-J. Agata, S. Detlef, Hydrogen Production: by Electrolysis, Wiley-VCH Verlag GmbH & Co, KGaA, Boschstr. 12, 69469 Weinheim,Germany, 2015.

[23] H. Yokokawa, H. Tu, B. Iwanschitz, A. Mai, Fundamental mechanisms limiting solid oxide fuel cell durability, J. Power Sources. (2008) 13.

[24] K. Chen, S.P. Jiang, Review—Materials Degradation of Solid Oxide Electrolysis Cells, J. Electrochem. Soc. 163 (2016) F3070–F3083. https://doi.org/10.1149/2.0101611jes.

[25] J. Laurencin, D. Kane, G. Delette, J. Deseure, F. Lefebvre-Joud, Modelling of solid oxide steam electrolyser: Impact of the operating conditions on hydrogen production, J. Power Sources. 196 (2011) 2080–2093. https://doi.org/10.1016/j.jpowsour.2010.09.054.

[26] F. Tietz, D. Sebold, A. Brisse, J. Schefold, Degradation phenomena in a solid oxide electrolysis cell after 9000 h of operation, J. Power Sources. 223 (2013) 129–135. https://doi.org/10.1016/j.jpowsour.2012.09.061.

[27] J. Laurencin, M. Hubert, D.F. Sanchez, S. Pylypko, M. Morales, A. Morata, B. Morel, D. Montinaro, F. Lefebvre-Joud, E. Siebert, Degradation mechanism of La 0.6 Sr 0.4 Co 0.2 Fe 0.8 O 3-δ /Gd 0.1 Ce 0.9 O 2-δ composite electrode operated under solid oxide electrolysis and fuel cell conditions, Electrochimica Acta. 241 (2017) 459–476. https://doi.org/10.1016/j.electacta.2017.05.011.

[28] P. Moçoteguy, A. Brisse, A review and comprehensive analysis of degradation mechanisms of solid oxide electrolysis cells, Int. J. Hydrog. Energy. 38 (2013) 15887–15902. https://doi.org/10.1016/j.ijhydene.2013.09.045.

[29] V. Wilde, H. Störmer, J. Szász, F. Wankmüller, E. Ivers-Tiffée, D. Gerthsen, $Gd_{0.2}Ce_{0.8}O_2$ Diffusion Barrier Layer between $(La_{0.58}Sr_{0.4})(Co_{0.2}Fe_{0.8})O_{3-\delta}$ Cathode and $Y_{0.16}Zr_{0.84}O_2$ Electrolyte for Solid Oxide Fuel Cells: Effect of Barrier Layer Sintering Temperature on Microstructure, ACS Appl. Energy Mater. 1 (2018) 6790–6800. https://doi.org/10.1021/acsaem.8b00847.

[30] H. Wang, S.A. Barnett, Degradation Mechanisms of Porous $La_{0.6}Sr_{0.4}Co_{0.2}Fe_{0.8}O_{3-\delta}$ Solid Oxide Fuel Cell Cathodes, J. Electrochem. Soc. 165 (2018) F564–F570. https://doi.org/10.1149/2.1211807jes.

[31] M. Trini, A. Hauch, S. De Angelis, X. Tong, P.V. Hendriksen, M. Chen, Comparison of microstructural evolution of fuel electrodes in solid oxide fuel cells and electrolysis cells, J. Power Sources. 450 (2020) 227599. https://doi.org/10.1016/j.jpowsour.2019.227599.

[32] F. Monaco, M. Hubert, J. Vulliet, J.P. Ouweltjes, D. Montinaro, P. Cloetens, P. Piccardo, F. Lefebvre-Joud, J. Laurencin, Degradation of Ni-YSZ Electrodes in Solid Oxide Cells: Impact of Polarization and Initial Microstructure on the Ni Evolution, J. Electrochem. Soc. 166 (2019) F1229–F1242. https://doi.org/10.1149/2.1261915jes.

[33] E. Lay-Grindler, J. Laurencin, J. Villanova, P. Cloetens, P. Bleuet, A. Mansuy, J. Mougin, G. Delette, Degradation study by 3D reconstruction of a nickel–yttria stabilized zirconia cathode after high temperature steam electrolysis operation, J. Power Sources. 269 (2014) 927–936. https://doi.org/10.1016/j.jpowsour.2014.07.066.

[34] M. Hubert, J. Laurencin, P. Cloetens, B. Morel, D. Montinaro, F. Lefebvre-Joud, Impact of Nickel agglomeration on Solid Oxide Cell operated in fuel cell and electrolysis modes, J. Power Sources. 397 (2018) 240–251. https://doi.org/10.1016/j.jpowsour.2018.06.097.
[35] J.R. Mawdsley, J. David Carter, A. Jeremy Kropf, B. Yildiz, V.A. Maroni, Post-test evaluation of oxygen electrodes from solid oxide electrolysis stacks☆, Int. J. Hydrog. Energy. 34 (2009) 4198–4207. https://doi.org/10.1016/j.ijhydene.2008.07.061.
[36] J. Laurencin, G. Delette, F. Lefebvre-Joud, M. Dupeux, A numerical tool to estimate SOFC mechanical degradation: Case of the planar cell configuration, J. Eur. Ceram. Soc. 28 (2008) 1857–1869. https://doi.org/10.1016/j.jeurceramsoc.2007.12.025.
[37] K. Chen, S.P. Jiang, Failure mechanism of (La,Sr)MnO3 oxygen electrodes of solid oxide electrolysis cells, Int. J. Hydrog. Energy. 36 (2011) 10541–10549. https://doi.org/10.1016/j.ijhydene.2011.05.103.
[38] A.V. Virkar, Mechanism of oxygen electrode delamination in solid oxide electrolyzer cells, Int. J. Hydrog. Energy. 35 (2010) 9527–9543. https://doi.org/10.1016/j.ijhydene.2010.06.058.
[39] M.A. Laguna-Bercero, R. Campana, A. Larrea, J.A. Kilner, V.M. Orera, Electrolyte degradation in anode supported microtubular yttria stabilized zirconia-based solid oxide steam electrolysis cells at high voltages of operation, J. Power Sources. 196 (2011) 8942–8947. https://doi.org/10.1016/j.jpowsour.2011.01.015.
[40] M. Ettler, H. Timmermann, J. Malzbender, A. Weber, N.H. Menzler, Durability of Ni anodes during reoxidation cycles, J. Power Sources. 195 (2010) 5452–5467. https://doi.org/10.1016/j.jpowsour.2010.03.049.
[41] L. Hu, C.-A. Wang, Effect of sintering temperature on compressive strength of porous yttria-stabilized zirconia ceramics, Ceram. Int. 36 (2010) 1697–1701. https://doi.org/10.1016/j.ceramint.2010.03.009.
[42] A. Atkinson, B. Sun, Residual stress and thermal cycling of planar solid oxide fuel cells, Mater. Sci. Technol. 23 (2007) 1135–1143. https://doi.org/10.1179/026708307X232910.
[43] A. Selçuk, G. Merere, A. Atkinson, The influence of electrodes on the strength of planar zirconia solid oxide fuel cells, J. Mater. Sci. (2001) 1173–1182.
[44] L. Liu, G.-Y. Kim, A. Chandra, Modeling of thermal stresses and lifetime prediction of planar solid oxide fuel cell under thermal cycling conditions, J. Power Sources. (2010) 9.
[45] J.B. Robinson, L.D. Brown, R. Jervis, O.O. Taiwo, T.M.M. Heenan, J. Millichamp, T.J. Mason, T.P. Neville, R. Clague, D.S. Eastwood, C. Reinhard, P.D. Lee, D.J.L. Brett, P.R. Shearing, Investigating the effect of thermal gradients on stress in solid oxide fuel cell anodes using combined synchrotron radiation and thermal imaging, J. Power Sources. 288 (2015) 473–481. https://doi.org/10.1016/j.jpowsour.2015.04.104.
[46] F. Usseglio-Viretta, Optimisation des performances et de la robustesse d'un électrolyseur à hautes températures, phdthesis, Université Grenoble Alpes, 2015. https://tel.archives-ouvertes.fr/tel-01223428 (accessed November 9, 2021).
[47] F. Greco, Improved thermo-mechanical reliability of anode-supported solid oxide fuel cells, 2018.
[48] J. Laurencin, G. Delette, B. Morel, F. Lefebvre-Joud, M. Dupeux, Solid Oxide Fuel Cells damage mechanisms due to Ni-YSZ re-oxidation: Case of the Anode Supported Cell, J. Power Sources. 192 (2009) 344–352. https://doi.org/10.1016/j.jpowsour.2009.02.089.
[49] N.A. Knopper, Final Publishable Summary Report, (2017) 41.

[50] M. Mori, T. Yamamoto, H. Itoh, H. Inaba, H. Tagawa, Thermal Expansion of Nickel-Zirconia Anodes in Solid Oxide Fuel Cells during Fabrication and Operation, J. Electrochem. Soc. 145 (1998) 1374–1381. https://doi.org/10.1149/1.1838468.
[51] A. Nakajo, C. Stiller, G. Härkegård, O. Bolland, Modeling of thermal stresses and probability of survival of tubular SOFC, J. Power Sources. 158 (2006) 287–294. https://doi.org/10.1016/j.jpowsour.2005.09.004.
[52] J. Malzbender, E. Wessel, R. Steinbrech, Reduction and re-oxidation of anodes for solid oxide fuel cells, Solid State Ion. 176 (2005) 2201–2203. https://doi.org/10.1016/j.ssi.2005.06.014.
[53] A. Faes, A. Nakajo, A. Hessler-Wyser, D. Dubois, A. Brisse, S. Modena, J. Van herle, RedOx study of anode-supported solid oxide fuel cell, J. Power Sources. 193 (2009) 55–64. https://doi.org/10.1016/j.jpowsour.2008.12.118.
[54] A. Nakajo, A.M. Kiss, A.P. Cocco, W.M. Harris, M.B. DeGostin, F. Greco, G.J. Nelson, A.A. Peracchio, B.N. Cassenti, A. Deriy, S. Wang, Y. Chen-Wiegart, J. Wang, J. Van herle, W.K.S. Chiu, Characterization of Cracks and their Effects on the Effective Transport Pathways in Ni-YSZ Anodes after Reoxidation Using X-Ray Nanotomography, ECS Trans. 68 (2015) 1069–1081. https://doi.org/10.1149/06801.1069ecst.
[55] A. Faes, A. Hessler-Wyser, A. Zryd, J. Van herle, A Review of RedOx Cycling of Solid Oxide Fuel Cells Anode, Membranes. 2 (2012) 585–664. https://doi.org/10.3390/membranes2030585.
[56] D. Sarantaridis, R.A. Rudkin, A. Atkinson, Oxidation failure modes of anode-supported solid oxide fuel cells, J. Power Sources. (2008) 7.
[57] G. Robert, E. Batawi, A. Schuler, S. Riggenbach, B. Pietzak, M. Molinelli, J. Van Herle, R. Irhinger, O. Bucheli, Swiss SOFC Integration Activities: Stacks, Systems, and Applications, Chim. Int. J. Chem. 58 (2004) 879–886. https://doi.org/10.2533/000942904777677065.
[58] D. Fouquet, A.C. Müller, A. Weber, E. Ivers-Tiffée, Kinetics of oxidation and reduction of Ni/YSZ cermets, Ionics. 9 (2003) 103–108. https://doi.org/10.1007/BF02376545.
[59] J. Laurencin, R. Quey, G. Delette, H. Suhonen, P. Cloetens, P. Bleuet, Characterisation of Solid Oxide Fuel Cell Ni–8YSZ substrate by synchrotron X-ray nano-tomography: from 3D reconstruction to microstructure quantification, J. Power Sources. 198 (2012) 182–189. https://doi.org/10.1016/j.jpowsour.2011.09.105.
[60] J. Laurencin, V. Roche, C. Jaboutian, I. Kieffer, J. Mougin, M.C. Steil, Ni-8YSZ cermet re-oxidation of anode supported solid oxide fuel cell: From kinetics measurements to mechanical damage prediction, Int. J. Hydrog. Energy. 37 (2012) 12557–12573. https://doi.org/10.1016/j.ijhydene.2012.06.019.
[61] B. Eigenmann, B. Scholtes, E. Macherauch, Materialwiss. (1989) 314–325.
[62] V. Vedasri, J.L. Young, V.I. Birss, A possible solution to the mechanical degradation of Ni–yttria stabilized zirconia anode-supported solid oxide fuel cells due to redox cycling, J. Power Sources. 195 (2010) 5534–5542. https://doi.org/10.1016/j.jpowsour.2010.03.043.
[63] M.H. Pihlatie, H.L. Frandsen, A. Kaiser, M. Mogensen, Continuum mechanics simulations of NiO/Ni–YSZ composites during reduction and re-oxidation, J. Power Sources. 195 (2010) 2677–2690. https://doi.org/10.1016/j.jpowsour.2009.11.079.
[64] S. Toros, Microstructural finite element modeling of redox behavior of Ni–YSZ based ceramic SOFC anodes, Ceram. Int. 42 (2016) 8915–8924. https://doi.org/10.1016/j.ceramint.2016.02.148.

[65] Y. Xiang, Y. Da, Z. Zhong, N. Shikazono, Z. Jiao, Thermo-mechanical stress analyses of solid oxide fuel cell anode based on three-dimensional microstructure reconstruction, Int. J. Hydrog. Energy. 45 (2020) 19791–19800. https://doi.org/10.1016/j.ijhydene.2020.05.121.
[66] F. Abdeljawad, G.J. Nelson, W.K.S. Chiu, M. Haataja, Redox instability, mechanical deformation, and heterogeneous damage accumulation in solid oxide fuel cell anodes, J. Appl. Phys. 112 (2012) 036102. https://doi.org/10.1063/1.4745038.
[67] D. Leguillon, R. Piat, Fracture of porous materials – Influence of the pore size, Eng. Fract. Mech. 75 (2008) 1840–1853. https://doi.org/10.1016/j.engfracmech.2006.12.002.
[68] D.N. Boccaccini, H.L. Frandsen, S. Soprani, M. Cannio, T. Klemensø, V. Gil, P.V. Hendriksen, Influence of porosity on mechanical properties of tetragonal stabilized zirconia, J. Eur. Ceram. Soc. 38 (2018) 1720–1735. https://doi.org/10.1016/j.jeurceramsoc.2017.09.029.
[69] N. Miyazaki, T. Hoshide, Influence of Porosity and Pore Distributions on Strength Properties of Porous Alumina, J. Mater. Eng. Perform. 27 (2018) 4345–4354. https://doi.org/10.1007/s11665-018-3500-x.
[70] E. Ryshkewitch, Compression Strength of Porous Sintered Alumina and Zirconia.: 9th Communication to Ceramography, J. Am. Ceram. Soc. 36 (1953) 65–68. https://doi.org/10.1111/j.1151-2916.1953.tb12837.x.
[71] T. Ostrowski, J. Rödel, Evolution of Mechanical Properties of Porous Alumina during Free Sintering and Hot Pressing, J. Am. Ceram. Soc. 82 (2004) 3080–3086. https://doi.org/10.1111/j.1151-2916.1999.tb02206.x.
[72] S. Meille, M. Lombardi, J. Chevalier, L. Montanaro, Mechanical properties of porous ceramics in compression: On the transition between elastic, brittle, and cellular behavior, J. Eur. Ceram. Soc. 32 (2012) 3959–3967. https://doi.org/10.1016/j.jeurceramsoc.2012.05.006.
[73] A. Abaza, J. Laurencin, A. Nakajo, M. Hubert, T. David, F. Monaco, C. Lenser, S. Meille, Fracture properties of porous yttria-stabilized zirconia under micro-compression testing, Submiss. (2021).
[74] S. Samborski, T. Sadowski, Dynamic Fracture Toughness of Porous Ceramics: Rapid Communications of the American Ceramic Society, J. Am. Ceram. Soc. 93 (2010) 3607–3609. https://doi.org/10.1111/j.1551-2916.2010.04133.x.
[75] P. Khajavi, J. Chevalier, P. Vang Hendriksen, J.W. Tavacoli, L. Gremillard, H. Lund Frandsen, Double Torsion testing of thin porous zirconia supports for energy applications: Toughness and slow crack growth assessment, J. Eur. Ceram. Soc. 40 (2020) 3191–3199. https://doi.org/10.1016/j.jeurceramsoc.2020.02.019.
[76] Z.-Y. Deng, J. She, Y. Inagaki, J.-F. Yang, T. Ohji, Y. Tanaka, Reinforcement by crack-tip blunting in porous ceramics, J. Eur. Ceram. Soc. 24 (2004) 2055–2059. https://doi.org/10.1016/S0955-2219(03)00365-0.
[77] I. Doltsinis, R. Dattke, Modelling the damage of porous ceramics under internal pressure, Comput. Methods Appl. Mech. Eng. 191 (2001) 29–46. https://doi.org/10.1016/S0045-7825(01)00243-2.
[78] A. Doitrand, R. Henry, T. Lube, S. Meille, Size effect assessment by Weibull's approach and the coupled criterion, Eng. Fract. Mech. 256 (2021) 107979. https://doi.org/10.1016/j.engfracmech.2021.107979.
[79] F. Lipperman, M. Ryvkin, M.B. Fuchs, Fracture toughness of two-dimensional cellular material with periodic microstructure, Int. J. Fract. 146 (2007) 279–290. https://doi.org/10.1007/s10704-007-9171-5.

[80] V.A. Mikushina, I.Yu. Smolin, Simulation of mesoscopic fracture of ceramics with hierarchical porosity, in: Ekaterinburg, Russia, 2018: p. 030041. https://doi.org/10.1063/1.5084402.
[81] T. Sadowski, S. Samborski, Prediction of the mechanical behaviour of porous ceramics using mesomechanical modelling, Comput. Mater. Sci. 28 (2003) 512–517. https://doi.org/10.1016/j.commatsci.2003.08.008.
[82] R. Romani, M. Bornert, D. Leguillon, R. Le Roy, K. Sab, Detection of crack onset in double cleavage drilled specimens of plaster under compression by digital image correlation – Theoretical predictions based on a coupled criterion, Eur. J. Mech. - ASolids. 51 (2015) 172–182. https://doi.org/10.1016/j.euromechsol.2014.12.002.
[83] M.E. Gurtin, On the energy release rate in quasi-static elastic crack propagation, J. Elast. 9 (1979) 187–195. https://doi.org/10.1007/BF00041325.
[84] M.E. Gurtin, Thermodynamics and the griffith criterion for brittle fracture, Int. J. Solids Struct. 15 (1979) 553–560. https://doi.org/10.1016/0020-7683(79)90082-9.
[85] D. Leguillon, Strength or toughness? A criterion for crack onset at a notch, Eur. J. Mech. - ASolids. 21 (2002) 61–72. https://doi.org/10.1016/S0997-7538(01)01184-6.
[86] Z. Cui, Y. Huang, H. Liu, Predicting the mechanical properties of brittle porous materials with various porosity and pore sizes, J. Mech. Behav. Biomed. Mater. 71 (2017) 10–22. https://doi.org/10.1016/j.jmbbm.2017.02.014.
[87] B. Šavija, G.E. Smith, D. Liu, E. Schlangen, P.E.J. Flewitt, Modelling of deformation and fracture for a model quasi-brittle material with controlled porosity: Synthetic versus real microstructure, Eng. Fract. Mech. 205 (2019) 399–417. https://doi.org/10.1016/j.engfracmech.2018.11.008.
[88] D. Jauffrès, C.L. Martin, A. Lichtner, R.K. Bordia, Simulation of the toughness of partially sintered ceramics with realistic microstructures, Acta Mater. 60 (2012) 4685–4694. https://doi.org/10.1016/j.actamat.2012.05.024.
[89] D. Jauffrès, C.L. Martin, R.K. Bordia, Design of strain tolerant porous microstructures – A case for controlled imperfection, Acta Mater. 148 (2018) 193–201. https://doi.org/10.1016/j.actamat.2017.12.039.
[90] X. Liu, C.L. Martin, D. Bouvard, S. Di Iorio, J. Laurencin, G. Delette, Strength of Highly Porous Ceramic Electrodes, J. Am. Ceram. Soc. 94 (2011) 3500–3508. https://doi.org/10.1111/j.1551-2916.2011.04669.x.
[91] A.Yu. Smolin, N.V. Roman, I.S. Konovalenko, G.M. Eremina, S.P. Buyakova, S.G. Psakhie, 3D simulation of dependence of mechanical properties of porous ceramics on porosity, Eng. Fract. Mech. 130 (2014) 53–64. https://doi.org/10.1016/j.engfracmech.2014.04.001.
[92] I.Yu. Smolin, P.V. Makarov, M.O. Eremin, K.S. Matyko, Numerical simulation of mesomechanical behavior of porous brittle materials, Procedia Struct. Integr. 2 (2016) 3353–3360. https://doi.org/10.1016/j.prostr.2016.06.418.
[93] H. Xu, H. Du, L. Kang, Q. Cheng, D. Feng, S. Xia, Constructing Straight Pores and Improving Mechanical Properties of GangueBased Porous Ceramics, J. Renew. Mater. 9 (2021) 2129–2141. https://doi.org/10.32604/jrm.2021.016090.
[94] B. Abdallah, F. Willot, D. Jeulin, Morphological modelling of three-phase microstructures of anode layers using SEM images: MORPHOLOGICAL MODELING OF THREE PHASES, J. Microsc. 263 (2016) 51–63. https://doi.org/10.1111/jmi.12374.
[95] A. Lanzini, P. Leone, P. Asinari, Microstructural characterization of solid oxide fuel cell electrodes by image analysis technique, J. Power Sources. 194 (2009) 408–422. https://doi.org/10.1016/j.jpowsour.2009.04.062.

[96] B. Shri Prakash, S. Senthil Kumar, S.T. Aruna, Properties and development of Ni/YSZ as an anode material in solid oxide fuel cell: A review, Renew. Sustain. Energy Rev. 36 (2014) 149–179. https://doi.org/10.1016/j.rser.2014.04.043.
[97] D. Roussel, A. Lichtner, D. Jauffrès, J. Villanova, R.K. Bordia, C.L. Martin, Strength of hierarchically porous ceramics: Discrete simulations on X-ray nanotomography images, Scr. Mater. 113 (2016) 250–253. https://doi.org/10.1016/j.scriptamat.2015.11.015.
[98] D. Liu, B. Šavija, G.E. Smith, P.E.J. Flewitt, T. Lowe, E. Schlangen, Towards understanding the influence of porosity on mechanical and fracture behaviour of quasi-brittle materials: experiments and modelling, Int. J. Fract. 205 (2017) 57–72. https://doi.org/10.1007/s10704-017-0181-7.
[99] Y. Hsiao, The degradation of SOFC electrodes, Solid State Ion. 98 (1997) 33–38. https://doi.org/10.1016/S0167-2738(97)00106-9.
[100] S. Sukino, S. Watanabe, K. Sato, F. Iguchi, H. Yugami, T. Kawada, J. Mizusaki, T. Hashida, Effect of Redox Cycling on Mechanical Properties of Ni-YSZ Cermets for SOFC Anodes, ECS Trans. 35 (2019) 1473–1482. https://doi.org/10.1149/1.3570133.
[101] T. Klemensø, C. Chung, P.H. Larsen, M. Mogensen, The Mechanism Behind Redox Instability of Anodes in High-Temperature SOFCs, J. Electrochem. Soc. (2005) 8.
[102] A. Nakajo, J. Kuebler, A. Faes, U.F. Vogt, H.J. Schindler, L.-K. Chiang, S. Modena, J. Van herle, T. Hocker, Compilation of mechanical properties for the structural analysis of solid oxide fuel cell stacks. Constitutive materials of anode-supported cells, Ceram. Int. 38 (2012) 3907–3927. https://doi.org/10.1016/j.ceramint.2012.01.043.
[103] A. Selçuk, A. Atkinson, Strength and Toughness of Tape-Cast Yttria-Stabilized Zirconia, J. Am. Ceram. Soc. 83 (2004) 2029–2035. https://doi.org/10.1111/j.1151-2916.2000.tb01507.x.
[104] A. Atkinson, Mechanical behaviour of ceramic oxygen ion-conducting membranes, Solid State Ion. 134 (2000) 59–66. https://doi.org/10.1016/S0167-2738(00)00714-1.
[105] Y. Dong, C.-A. Wang, J. Zhou, Effect of YSZ fiber addition on microstructure and properties of porous YSZ ceramics, J. Mater. Sci. 47 (2012) 6326–6332. https://doi.org/10.1007/s10853-012-6555-3.
[106] E. Camposilvan, M. Anglada, Size and plasticity effects in zirconia micropillars compression, Acta Mater. 103 (2016) 882–892. https://doi.org/10.1016/j.actamat.2015.10.047.
[107] M. Mutoh, T. Nagoshi, T.-F. Mark Chang, T. Sato, M. Sone, Micro-compression test using non-tapered micro-pillar of electrodeposited Cu, Microelectron. Eng. 111 (2013) 118–121. https://doi.org/10.1016/j.mee.2013.02.040.
[108] H. Tang, K. Hashigata, T.-F.M. Chang, C.-Y. Chen, T. Nagoshi, D. Yamane, T. Konishi, K. Machida, K. Masu, M. Sone, Sample size effect on micro-mechanical properties of gold electroplated with dense carbon dioxide, Surf. Coat. Technol. 350 (2018) 1065–1070. https://doi.org/10.1016/j.surfcoat.2018.02.041.
[109] T. Nagoshi, T.-F.M. Chang, S. Tatsuo, M. Sone, Mechanical properties of nickel fabricated by electroplating with supercritical CO2 emulsion evaluated by micro-compression test using non-tapered micro-sized pillar, Microelectron. Eng. 110 (2013) 270–273. https://doi.org/10.1016/j.mee.2013.02.001.
[110] J.R. Greer, W.C. Oliver, W.D. Nix, Size dependence of mechanical properties of gold at the micron scale in the absence of strain gradients, Acta Mater. 53 (2005) 1821–1830. https://doi.org/10.1016/j.actamat.2004.12.031.
[111] Y. Yang, J.C. Ye, J. Lu, F.X. Liu, P.K. Liaw, Effects of specimen geometry and base material on the mechanical behavior of focused-ion-beam-fabricated metallic-glass

micropillars, Acta Mater. 57 (2009) 1613–1623. https://doi.org/10.1016/j.actamat.2008.11.043.
[112] Y. Xiao, V. Maier-Kiener, J. Michler, R. Spolenak, J.M. Wheeler, Deformation behavior of aluminum pillars produced by Xe and Ga focused ion beams: Insights from strain rate jump tests, Mater. Des. 181 (2019) 107914. https://doi.org/10.1016/j.matdes.2019.107914.
[113] R. Henry, T. Blay, T. Douillard, A. Descamps-Mandine, I. Zacharie-Aubrun, J.-M. Gatt, C. Langlois, S. Meille, Local fracture toughness measurements in polycrystalline cubic zirconia using micro-cantilever bending tests, Mech. Mater. 136 (2019) 103086. https://doi.org/10.1016/j.mechmat.2019.103086.
[114] W. Luo, C. Kirchlechner, X. Fang, S. Brinckmann, G. Dehm, F. Stein, Influence of composition and crystal structure on the fracture toughness of NbCo2 Laves phase studied by micro-cantilever bending tests, Mater. Des. 145 (2018) 116–121. https://doi.org/10.1016/j.matdes.2018.02.045.
[115] D. Gonzalez-Nino, S. Sonntag, M. Afshar-Mohajer, J. Goss, M. Zou, G.S. Prinz, Micromechanical Tension Testing of Additively Manufactured 17-4 PH Stainless Steel Specimens, JoVE J. Vis. Exp. (2021) e62433. https://doi.org/10.3791/62433.
[116] J.M. Tarragó, J.J. Roa, E. Jiménez-Piqué, E. Keown, J. Fair, L. Llanes, Mechanical deformation of WC–Co composite micropillars under uniaxial compression, Int. J. Refract. Met. Hard Mater. 54 (2016) 70–74. https://doi.org/10.1016/j.ijrmhm.2015.07.015.
[117] X. Zhang, Q. Zhao, S. Wang, R. Trejo, E. Lara-Curzio, G. Du, Characterizing strength and fracture of wood cell wall through uniaxial micro-compression test, Compos. Part Appl. Sci. Manuf. 41 (2010) 632–638. https://doi.org/10.1016/j.compositesa.2010.01.010.
[118] Z. Du, X.M. Zeng, Q. Liu, A. Lai, S. Amini, A. Miserez, C.A. Schuh, C.L. Gan, Size effects and shape memory properties in ZrO2 ceramic micro- and nano-pillars, Scr. Mater. 101 (2015) 40–43. https://doi.org/10.1016/j.scriptamat.2015.01.013.
[119] C. Chen, S. Nagao, T. Sugahara, H. Zhang, J. Jiu, K. Suganuma, T. Iwashige, K. Sugiura, K. Tsuruta, Effect of size and shape of Ag particles for mechanical properties of sintered Ag joints evaluated by micro-compression test, in: 2017 Int. Conf. Electron. Packag. ICEP, IEEE, Yamagata, Japan, 2017: pp. 130–134. https://doi.org/10.23919/ICEP.2017.7939340.
[120] J. Laurencin, G. Delette, F. Usseglio-Viretta, S. Di Iorio, Creep behaviour of porous SOFC electrodes: Measurement and application to Ni-8YSZ cermets, J. Eur. Ceram. Soc. 31 (2011) 1741–1752. https://doi.org/10.1016/j.jeurceramsoc.2011.02.036.
[121] A. Ernst, M. Wei, M. Aindow, A Comparison of Ga FIB and Xe-Plasma FIB of Complex Al Alloys, Microsc. Microanal. 23 (2017) 288–289. https://doi.org/10.1017/S1431927617002124.
[122] R. Mahbub, T. Hsu, W.K. Epting, N.T. Nuhfer, G.A. Hackett, H. Abernathy, A.D. Rollett, M. De Graef, S. Litster, P.A. Salvador, A Method for Quantitative 3D Mesoscale Analysis of Solid Oxide Fuel Cell Microstructures Using Xe-plasma Focused Ion Beam (PFIB) Coupled with SEM, ECS Trans. 78 (2017) 2159–2170. https://doi.org/10.1149/07801.2159ecst.
[123] P.R. Munroe, The application of focused ion beam microscopy in the material sciences, Mater. Charact. (2009) 12.
[124] C.A. Volkert, A.M. Minor, Focused Ion Beam Microscopy and Micromachining, MRS Bull. 32 (2007) 389–399. https://doi.org/10.1557/mrs2007.62.
[125] J. Laurencin, R. Quey, G. Delette, H. Suhonen, P. Cloetens, P. Bleuet, Characterisation of Solid Oxide Fuel Cell Ni–8YSZ substrate by synchrotron X-ray nano-tomography:

from 3D reconstruction to microstructure quantification, J. Power Sources. 198 (2012) 182–189. https://doi.org/10.1016/j.jpowsour.2011.09.105.
[126] A.W. Colldeweih, A. Baris, P. Spätig, S. Abolhassani, Evaluation of mechanical properties of irradiated zirconium alloys in the vicinity of the metal-oxide interface, Mater. Sci. Eng. A. 742 (2019) 842–850. https://doi.org/10.1016/j.msea.2018.09.107.
[127] H. Zhang, B.E. Schuster, Q. Wei, K.T. Ramesh, The design of accurate micro-compression experiments, Scr. Mater. 54 (2006) 181–186. https://doi.org/10.1016/j.scriptamat.2005.06.043.
[128] J.H. Fitschen, J. Ma, S. Schuff, Removal of curtaining effects by a variational model with directional forward differences, Comput. Vis. Image Underst. 155 (2017) 24–32. https://doi.org/10.1016/j.cviu.2016.12.008.
[129] J. Villanova, J. Laurencin, P. Cloetens, P. Bleuet, G. Delette, H. Suhonen, F. Usseglio-Viretta, 3D phase mapping of solid oxide fuel cell YSZ/Ni cermet at the nanoscale by holographic X-ray nanotomography, J. Power Sources. 243 (2013) 841–849. https://doi.org/10.1016/j.jpowsour.2013.06.069.
[130] M. Hubert, A. Pacureanu, C. Guilloud, Y. Yang, J.C. da Silva, J. Laurencin, F. Lefebvre-Joud, P. Cloetens, Efficient correction of wavefront inhomogeneities in X-ray holographic nanotomography by random sample displacement, Appl. Phys. Lett. 112 (2018) 203704. https://doi.org/10.1063/1.5026462.
[131] H. Moussaoui, Microstructural optimization of Solid Oxide Cells: a coupled stochastic geometrical and electrochemical modeling approach applied to LSCF-CGO electrode, (2019) 193.
[132] W. Pabst, E. Gregorová, G. Tichá, Elasticity of porous ceramics—A critical study of modulus−porosity relations, J. Eur. Ceram. Soc. 26 (2006) 1085–1097. https://doi.org/10.1016/j.jeurceramsoc.2005.01.041.
[133] X. Chen, S. Wu, J. Zhou, Influence of porosity on compressive and tensile strength of cement mortar, Constr. Build. Mater. 40 (2013) 869–874. https://doi.org/10.1016/j.conbuildmat.2012.11.072.
[134] A. Abaza, J. Laurencin, A. Nakajo, S. Meille, J. Debayle, D. Leguillon, Prediction of crack nucleation and propagation in porous ceramics using the phase-field approach, Theor. Appl. Fract. Mech. 119 (2022) 103349. https://doi.org/10.1016/j.tafmec.2022.103349.
[135] T.T. Nguyen, J. Yvonnet, M. Bornert, C. Chateau, F. Bilteryst, E. Steib, Large-scale simulations of quasi-brittle microcracking in realistic highly heterogeneous microstructures obtained from micro CT imaging, Extreme Mech. Lett. 17 (2017) 50–55. https://doi.org/10.1016/j.eml.2017.09.013.
[136] C. Miehe, M. Hofacker, F. Welschinger, A phase field model for rate-independent crack propagation: Robust algorithmic implementation based on operator splits, Comput. Methods Appl. Mech. Eng. 199 (2010) 2765–2778. https://doi.org/10.1016/j.cma.2010.04.011.
[137] N. Moes, J. Dolbow, T. Belytschko, A finite element method for crack growth without remeshing, (1999) 20.
[138] G. Molnár, A. Gravouil, 2D and 3D Abaqus implementation of a robust staggered phase-field solution for modeling brittle fracture, Finite Elem. Anal. Des. 130 (2017) 27–38. https://doi.org/10.1016/j.finel.2017.03.002.
[139] T.T. Nguyen, J. Yvonnet, M. Bornert, C. Chateau, K. Sab, R. Romani, R. Le Roy, On the choice of parameters in the phase field method for simulating crack initiation with experimental validation, Int. J. Fract. 197 (2016) 213–226. https://doi.org/10.1007/s10704-016-0082-1.

[140] T. Rabczuk, Computational Methods for Fracture in Brittle and Quasi-Brittle Solids: State-of-the-Art Review and Future Perspectives, ISRN Appl. Math. 2013 (2013) 1–38. https://doi.org/10.1155/2013/849231.
[141] K. Seleš, A. Jurčević, Z. Tonković, J. Sorić, Crack propagation prediction in heterogeneous microstructure using an efficient phase-field algorithm, Theor. Appl. Fract. Mech. 100 (2019) 289–297. https://doi.org/10.1016/j.tafmec.2019.01.022.
[142] B. Bourdin, G.A. Francfort, J.-J. Marigo, The Variational Approach to Fracture, Springer Netherlands, Dordrecht, 2008. https://doi.org/10.1007/978-1-4020-6395-4.
[143] G.A. Francfort, J.-J. Marigo, Revisiting brittle fracture as an energy minimization problem, J. Mech. Phys. Solids. 46 (1998) 1319–1342. https://doi.org/10.1016/S0022-5096(98)00034-9.
[144] K. Pham, J.-J. Marigo, Approche variationnelle de l'endommagement : II. Les modèles à gradient, Comptes Rendus Mécanique. 338 (2010) 199–206. https://doi.org/10.1016/j.crme.2010.03.012.
[145] K. Pham, J.-J. Marigo, Approche variationnelle de l'endommagement : I. Les concepts fondamentaux, Comptes Rendus Mécanique. 338 (2010) 191–198. https://doi.org/10.1016/j.crme.2010.03.009.
[146] C. Miehe, F. Welschinger, M. Hofacker, Thermodynamically consistent phase-field models of fracture: Variational principles and multi-field FE implementations, Int. J. Numer. Methods Eng. 83 (2010) 1273–1311. https://doi.org/10.1002/nme.2861.
[147] S. Zhou, X. Zhuang, H. Zhu, T. Rabczuk, Phase field modelling of crack propagation, branching and coalescence in rocks, Theor. Appl. Fract. Mech. 96 (2018) 174–192. https://doi.org/10.1016/j.tafmec.2018.04.011.
[148] S. Zhou, T. Rabczuk, X. Zhuang, Phase field modeling of quasi-static and dynamic crack propagation: COMSOL implementation and case studies, Adv. Eng. Softw. 122 (2018) 31–49. https://doi.org/10.1016/j.advengsoft.2018.03.012.
[149] H. Amor, J.-J. Marigo, C. Maurini, Regularized formulation of the variational brittle fracture with unilateral contact: Numerical experiments, J. Mech. Phys. Solids. 57 (2009) 1209–1229. https://doi.org/10.1016/j.jmps.2009.04.011.
[150] M.J. Borden, C.V. Verhoosel, M.A. Scott, T.J.R. Hughes, C.M. Landis, A phase-field description of dynamic brittle fracture, Comput. Methods Appl. Mech. Eng. 217–220 (2012) 77–95. https://doi.org/10.1016/j.cma.2012.01.008.
[151] E. Tanné, T. Li, B. Bourdin, J.-J. Marigo, C. Maurini, Crack nucleation in variational phase-field models of brittle fracture, J. Mech. Phys. Solids. 110 (2018) 80–99. https://doi.org/10.1016/j.jmps.2017.09.006.
[152] G. Molnár, A. Doitrand, R. Estevez, A. Gravouil, Toughness or strength? Regularization in phase-field fracture explained by the coupled criterion, Theor. Appl. Fract. Mech. 109 (2020) 102736. https://doi.org/10.1016/j.tafmec.2020.102736.
[153] A. Kumar, B. Bourdin, G.A. Francfort, O. Lopez-Pamies, Revisiting nucleation in the phase-field approach to brittle fracture, J. Mech. Phys. Solids. 142 (2020) 104027. https://doi.org/10.1016/j.jmps.2020.104027.
[154] C. Kuhn, A. Schlüter, R. Müller, On degradation functions in phase field fracture models, Comput. Mater. Sci. 108 (2015) 374–384. https://doi.org/10.1016/j.commatsci.2015.05.034.
[155] D. Leguillon, D. Quesada, C. Putot, E. Martin, Prediction of crack initiation at blunt notches and cavities – size effects, Eng. Fract. Mech. 74 (2007) 2420–2436. https://doi.org/10.1016/j.engfracmech.2006.11.008.
[156] M.L. Dunn, W. Suwito, S. Cunningham, Fracture initiation at sharp notches: Correlation using critical stress intensities, Int. J. Solids Struct. 34 (1997) 3873–3883. https://doi.org/10.1016/S0020-7683(96)00236-3.

[157] T.L. Anderson, Fracture Mechanics: Fundamentals and Applications, Taylor & Francis Group, 2005.
[158] A. Doitrand, D. Leguillon, Comparison between 2D and 3D applications of the coupled criterion to crack initiation prediction in scarf adhesive joints, Int. J. Adhes. Adhes. 85 (2018) 69–76. https://doi.org/10.1016/j.ijadhadh.2018.05.022.
[159] H. Moussaoui, J. Debayle, Y. Gavet, G. Delette, M. Hubert, P. Cloetens, J. Laurencin, 3D geometrical characterization and modelling of solid oxide cells electrodes microstructure by image analysis, in: H. Nagahara, K. Umeda, A. Yamashita (Eds.), Tokyo, Japan, 2017: p. 1033804. https://doi.org/10.1117/12.2264376.
[160] P. Abrahamsen, A review of Gaussian random fields and correlation functions, Research Council of Norway, 1997.
[161] A. Abaza, J. Laurencin, A. Nakajo, M. Hubert, T. David, F. Monaco, C. Lenser, S. Meille, Fracture properties of porous yttria-stabilized zirconia under micro-compression testing, J. Eur. Ceram. Soc. (2021). https://doi.org/10.1016/j.jeurceramsoc.2021.11.051.
[162] A. Doitrand, R. Henry, J. Chevalier, S. Meille, Revisiting the strength of micron-scale ceramic platelets, J. Am. Ceram. Soc. 103 (2020) 6991–7000. https://doi.org/10.1111/jace.17148.
[163] A. Faes, A. Hessler-Wyser, A. Zryd, J. Van herle, A Review of RedOx Cycling of Solid Oxide Fuel Cells Anode, Membranes. 2 (2012) 585–664. https://doi.org/10.3390/membranes2030585.
[164] J. Laurencin, V. Roche, C. Jaboutian, I. Kieffer, J. Mougin, M.C. Steil, Ni-8YSZ cermet re-oxidation of anode supported solid oxide fuel cell: From kinetics measurements to mechanical damage prediction, Int. J. Hydrog. Energy. 37 (2012) 12557–12573. https://doi.org/10.1016/j.ijhydene.2012.06.019.
[165] J. Laurencin, G. Delette, B. Morel, F. Lefebvre-Joud, M. Dupeux, Solid Oxide Fuel Cells damage mechanisms due to Ni-YSZ re-oxidation: Case of the Anode Supported Cell, J. Power Sources. 192 (2009) 344–352. https://doi.org/10.1016/j.jpowsour.2009.02.089.
[166] E.D.R. Silva, M. Hubert, B. Morel, H. Moussaoui, J. Debayle, J. Laurencin, A Dynamic Multi-Scale Model for Solid Oxide Cells Validated on Local Current Measurements: Impact of Global Cell Operation on the Electrodes Reaction Mechanisms, ECS Trans. 103 (2021) 893. https://doi.org/10.1149/10301.0893ecst.